

1                     **Simultaneous Measurement of**  
2                     **Oscillation Parameters in Beam and**  
3                     **Atmospheric Neutrino Data from**  
4                     **Tokai-to-Kamioka and**  
5                     **Super-Kamiokande Experiments**

6                     Daniel Robert Clement Barrow

7                     Magdalen College,  
8                     Oxford University

<sup>10</sup> A Dissertation Submitted to Oxford University

<sup>11</sup> for the Degree of Doctor of Philosophy

<sup>12</sup>

13                   **Simultaneous Measurement of**

14                   **Oscillation Parameters in Beam and**

15                   **Atmospheric Neutrino Data from**

16                   **Tokai-to-Kamioka and**

17                   **Super-Kamiokande Experiments**

18                   *Abstract*

19                   Lorem ipsum dolor sit amet, consectetur adipiscing elit, sed do eiusmod tempor incididunt ut labore et dolore magna aliqua. Nulla aliquet porttitor lacus luctus accumsan tortor posuere. Pulvinar neque laoreet suspendisse interdum. Sem viverra aliquet eget sit. Nunc sed velit dignissim sodales ut eu sem integer vitae. At erat pellentesque adipiscing commodo elit at imperdiet dui accumsan. Fames ac turpis egestas integer eget aliquet nibh. Scelerisque eu ultrices vitae auctor eu augue. Purus non enim praesent elementum facilisis leo vel. Sollicitudin nibh sit amet commodo. Vitae auctor eu augue ut. Vel quam elementum pulvinar etiam. A condimentum vitae sapien pellentesque habitant morbi tristique senectus. Viverra accumsan in nisl nisi scelerisque eu ultrices. Sed viverra ipsum nunc aliquet bibendum enim. Sit amet purus gravida quis. In vitae turpis massa

<sup>32</sup> sed elementum tempus egestas sed sed. Vivamus arcu felis bibendum  
<sup>33</sup> ut tristique et egestas. Senectus et netus et malesuada fames ac turpis.  
<sup>34</sup> Ac auctor augue mauris augue.

## 35 Declaration

36 This dissertation is the result of my own work, except where ex-  
37 plicit reference is made to the work of others, and has not been sub-  
38 mitted for another qualification to this or any other university. This  
39 dissertation does not exceed the word limit for the respective Degree  
40 Committee.

41 Daniel Robert Clement Barrow

42 ©The copyright of this thesis rests with the author and is made available under a Creative  
43 Commons Attribution Non-Commercial No Derivatives licence. Researchers are free to copy,  
44 distribute or transmit the thesis on the condition that they attribute it, that they do not use  
45 it for commercial purposes and that they do not alter, transform or build upon it. For any  
46 reuse or redistribution, researchers must make clear to others the licence terms of this work.

47

## Acknowledgements

48 at pretium nibh ipsum. Eget nunc scelerisque viverra mauris in aliquam. Arcu vitae  
49 elementum curabitur vitae nunc sed velit dignissim. Sed arcu non odio euismod lacinia  
50 at quis risus sed. Vitae tempus quam pellentesque nec nam aliquam sem et tortor.  
51 Viverra aliquet eget sit amet tellus cras adipiscing. Purus sit amet luctus venenatis  
52 lectus magna. In aliquam sem fringilla ut morbi tincidunt augue. Fermentum dui  
53 faucibus in ornare. Aliquam malesuada bibendum arcu vitae elementum curabitur  
54 vitae nunc sed.

55 Ultricies leo integer malesuada nunc vel risus commodo. Tellus cras adipiscing  
56 enim eu turpis egestas pretium. Dictumst quisque sagittis purus sit amet volutpat  
57 consequat mauris nunc. Vitae congue mauris rhoncus aenean vel elit scelerisque  
58 mauris pellentesque. Vel facilisis volutpat est velit egestas dui id ornare. Suscipit  
59 adipiscing bibendum est ultricies. At in tellus integer feugiat scelerisque varius  
60 morbi enim. Cras semper auctor neque vitae tempus. Commodo sed egestas egestas  
61 fringilla phasellus faucibus. Cras pulvinar mattis nunc sed blandit. Pretium viverra  
62 suspendisse potenti nullam ac tortor vitae. Purus sit amet volutpat consequat. Orci  
63 sagittis eu volutpat odio facilisis mauris. Sit amet massa vitae tortor condimentum  
64 lacinia quis. Commodo sed egestas egestas fringilla phasellus. Sed libero enim sed  
65 faucibus turpis. Vitae tempus quam pellentesque nec.

66 Blandit massa enim nec dui. Viverra tellus in hac habitasse platea dictumst vestibulu-  
67 lum. Bibendum enim facilisis gravida neque convallis. Sagittis nisl rhoncus mattis  
68 rhoncus urna neque. Nisl rhoncus mattis rhoncus urna neque. Ac tortor vitae purus  
69 faucibus ornare. Aenean sed adipiscing diam donec adipiscing tristique risus. Sapien  
70 nec sagittis aliquam malesuada bibendum. Et leo duis ut diam quam nulla. Tellus  
71 rutrum tellus pellentesque eu tincidunt tortor aliquam nulla facilisi. Fermentum leo

<sup>72</sup> vel orci porta non pulvinar neque. Eget sit amet tellus cras adipiscing enim eu. Sed  
<sup>73</sup> viverra tellus in hac habitasse platea dictumst vestibulum.

<sup>74</sup> Sit amet consectetur adipiscing elit. At varius vel pharetra vel turpis nunc eget  
<sup>75</sup> lorem. Elit scelerisque mauris pellentesque pulvinar pellentesque habitant morbi  
<sup>76</sup> tristique senectus. Odio euismod lacinia at quis risus sed vulputate odio. Vitae suscipit  
<sup>77</sup> tellus mauris a diam maecenas sed enim ut. Dignissim convallis aenean et tortor at  
<sup>78</sup> risus viverra. Diam sollicitudin tempor id eu. Erat velit scelerisque in dictum. Blandit  
<sup>79</sup> cursus risus at ultrices. Ac tortor vitae purus faucibus ornare suspendisse sed.

# **Contents**

<b>81</b>	<b>1</b>	<b>Neutrino Oscillation Physics</b>	<b>1</b>
82	1.1	Discovery of Neutrinos . . . . .	1
83	1.2	Theory of Neutrino Oscillation . . . . .	3
84	1.2.1	Three Flavour Oscillations . . . . .	3
85	1.2.2	The MSW Effect . . . . .	7
86	1.3	Neutrino Oscillation Measurements . . . . .	8
87	1.3.1	Solar Neutrinos . . . . .	9
88	1.3.2	Atmospheric Neutrinos . . . . .	11
89	1.3.3	Accelerator Neutrinos . . . . .	14
90	1.3.4	Reactor Neutrinos . . . . .	17
<b>91</b>	<b>2</b>	<b>T2K and SK Experiment Overview</b>	<b>20</b>
92	2.1	The Super-Kamiokande Experiment . . . . .	20
93	2.1.1	The SK Detector . . . . .	21
94	2.1.2	Calibration . . . . .	25
95	2.1.3	Data Acquisition and Triggering . . . . .	28
96	2.1.4	Cherenkov Radiation . . . . .	30
97	2.2	The Tokai to Kamioka Experiment . . . . .	32
98	2.2.1	The Neutrino Beam . . . . .	34
99	2.2.2	The Near Detector at 280m . . . . .	37
100	2.2.2.1	Fine Grained Detectors . . . . .	40
101	2.2.2.2	Time Projection Chambers . . . . .	41
102	2.2.2.3	$\pi^0$ Detector . . . . .	43
103	2.2.2.4	Electromagnetic Calorimeter . . . . .	43
104	2.2.2.5	Side Muon Range Detector . . . . .	45

105	2.2.3 The Interactive Neutrino GRID . . . . .	45
106	<b>3 Bayesian Statistics and Markov Chain Monte Carlo Techniques</b>	47
107	3.1 Bayesian Statistics . . . . .	48
108	3.2 Monte Carlo Simulation . . . . .	49
109	3.2.1 Markov Chain Monte Carlo . . . . .	51
110	3.2.2 Metropolis-Hastings Algorithm . . . . .	54
111	3.2.3 MCMC Optimisation . . . . .	55
112	3.3 Understanding the MCMC Results . . . . .	59
113	3.3.1 Marginalisation . . . . .	59
114	3.3.2 Parameter Estimation and Credible Intervals . . . . .	60
115	3.3.3 Application of Bayes' Theorem . . . . .	62
116	3.3.4 Comparison of MCMC Output to Expectation . . . . .	63
117	<b>4 Oscillation Probability Calculation</b>	65
118	4.1 Overview . . . . .	66
119	4.2 Treatment of Fast Oscillations . . . . .	72
120	4.3 Calculation Engine . . . . .	82
121	4.4 Matter Density Profile . . . . .	83
122	4.5 Production Height Averaging . . . . .	89
123	<b>Bibliography</b>	93
124	<b>List of Figures</b>	101
125	<b>List of Tables</b>	108



<sup>127</sup> **Chapter 1**

<sup>128</sup> **Neutrino Oscillation Physics**

<sup>129</sup> When first proposed, neutrinos were expected to be massless fermions that only in-  
<sup>130</sup> teract through weak and gravitational forces. This meant they were very difficult to  
<sup>131</sup> detect as they can pass through significant amounts of matter without interacting. De-  
<sup>132</sup> spite this, experimental neutrino physics has developed with many different detection  
<sup>133</sup> techniques and neutrino sources being used today. In direct tension with the standard  
<sup>134</sup> model physics, neutrinos have been determined to oscillate between different lepton  
<sup>135</sup> flavours requiring them to have mass.

<sup>136</sup> section 1.1 describes the observation techniques and discovery of neutrinos. The  
<sup>137</sup> theory underpinning neutrino oscillation is described in section 1.2. This section  
<sup>138</sup> includes the approximations which can be made to simplify the understanding of  
<sup>139</sup> neutrino oscillation in a two-flavour approximation as well as how the medium  
<sup>140</sup> in which neutrinos propagate can manipulate the oscillation probability. The past,  
<sup>141</sup> current, and future neutrino experiments are detailed in section 1.3 including the  
<sup>142</sup> reactor, atmospheric, and long-baseline accelerator neutrino sources that have been  
<sup>143</sup> used to successfully constrain oscillation parameter determination.

<sup>144</sup> **1.1 Discovery of Neutrinos**

<sup>145</sup> At the start of the 20<sup>th</sup> century, the electrons emitted from the  $\beta$ -decay of the nucleus  
<sup>146</sup> were found to have a continuous energy spectrum [1,2]. This observation seemingly  
<sup>147</sup> broke the energy conservation invoked within that period's nuclear models. Postulated

in 1930 by Pauli as the solution to this problem, the neutrino (originally termed “neutron”) was theorized to be an electrically neutral spin-1/2 fermion with a mass of the same order of magnitude as the electron [3]. This neutrino was to be emitted with the electron in  $\beta$ -decay to alleviate the apparent breaking of energy conservation. As a predecessor of the weak interaction model, Fermi’s theory of  $\beta$ -decay developed the understanding by coupling the four constituent particles; electron, proton, neutron, and neutrino, into a consistent model [4].

Whilst Pauli was not convinced of the ability to detect neutrinos. The first observations of the particle were made in the mid-1950s when neutrinos from a reactor were observed via the inverse  $\beta$ -decay (IBD) process,  $\bar{\nu}_e + p \rightarrow n + e^+$  [5, 6]. The detector consisted of two parts; a neutrino interaction medium and a liquid scintillator. The interaction medium was built from two water tanks. These were loaded with cadmium chloride to allow increased efficiency of neutron capture. The positron emitted from IBD annihilates,  $e^+ + e^- \rightarrow 2\gamma$ , generating a prompt signal and the neutron is captured on the cadmium via  $n + ^{108}Cd \rightarrow ^{109}Cd \rightarrow ^{109}Cd + \gamma$ , producing a delayed signal. The experiment observed an increase in the neutrino event rate when the reactor was operating compared to when it was switched off, in much the same way as modern reactor neutrino experiments operate.

After the discovery of the  $\nu_e$ , the natural question of how many flavours of neutrino exist was asked. In 1962, a measurement of the  $\nu_\mu$  was conducted at the Brookhaven National Laboratory [7]. A proton beam was directed at a beryllium target, generating a  $\pi$ -dominated beam which then decayed via  $\pi^\pm \rightarrow \mu^\pm + (\nu_\mu, \bar{\nu}_\mu)$ , and the subsequent interactions of the  $\nu_\mu$  were observed. The final observation to be made was that of the  $\nu_\tau$  from the DONUT experiment [8]. Three neutrinos seem the obvious solution as it mirrors the known number of charged lepton (as they form weak isospin doublets) but there could be evidence of more. Several neutrino experiments have found anomalous

<sub>174</sub> results [9, 10] which could be attributed to sterile neutrinos however cosmological  
<sub>175</sub> observations indicate the number of neutrino species  $N_{eff} = 3.15 \pm 0.23$  [11].

## <sub>176</sub> 1.2 Theory of Neutrino Oscillation

<sub>177</sub> As direct evidence of beyond Standard Model physics, a neutrino generated with  
<sub>178</sub> lepton flavour  $\alpha$  can change into a different lepton flavour  $\beta$  after propagating some  
<sub>179</sub> distance. This phenomenon is called neutrino oscillation and requires that neutrinos  
<sub>180</sub> must have a non-zero mass (as seen in subsection 1.2.1). This is direct evidence  
<sub>181</sub> of beyond standard model physics. This behaviour has been characterised by the  
<sub>182</sub> Pontecorvo-Maki-Nakagawa-Sakata (PMNS) [12–14] mixing matrix which describes  
<sub>183</sub> how the flavour and mass of neutrinos are associated. This is analogous to the Cabibbo-  
<sub>184</sub> Kobayashi-Maskawa (CKM) [15] matrix measured in quark physics.

### <sub>185</sub> 1.2.1 Three Flavour Oscillations

<sub>186</sub> The PMNS parameterisation defines three flavour eigenstates,  $\nu_e$ ,  $\nu_\mu$  and  $\nu_\tau$  (indexed  
<sub>187</sub>  $\nu_\alpha$ ), which are assigned based upon the weak interaction flavour states and three mass  
<sub>188</sub> eigenstates,  $\nu_1$ ,  $\nu_2$  and  $\nu_3$  (indexed  $\nu_i$ ). Each mass eigenstate is the superposition of all  
<sub>189</sub> three flavour states,

$$|\nu_i\rangle = \sum_\alpha U_{\alpha i} |\nu_\alpha\rangle. \quad (1.1)$$

<sub>190</sub>  $U$  is the PMNS matrix which correlates the mass and flavour eigenstates. Neutrinos  
<sub>191</sub> interact with leptons of the same weak flavour eigenstate rather than mass eigenstate.

<sup>192</sup> The propagation of a neutrino flavour eigenstate, in a vacuum, can be re-written as a  
<sup>193</sup> plane-wave solution to the time-dependent Schrödinger equation,

$$|\nu_\alpha(t)\rangle = \sum_i U_{\alpha i}^* |\nu_i\rangle e^{-i\phi_i}. \quad (1.2)$$

<sup>194</sup> The probability of observing a neutrino of flavour eigenstate  $\beta$  from one which  
<sup>195</sup> originated as flavour  $\alpha$  can be calculated as,

$$P(\nu_\alpha \rightarrow \nu_\beta) = |\langle \nu_\beta | \nu_\alpha(t) \rangle|^2 = \sum_{i,j} U_{\alpha i}^* U_{\beta i} U_{\alpha j} U_{\beta j}^* e^{-i(\phi_j - \phi_i)} \quad (1.3)$$

<sup>196</sup> The  $\phi_i$  term can be expressed in terms of the energy,  $E_i$ , and magnitude of the  
<sup>197</sup> three momenta,  $p_i$ , of the neutrino,  $\phi_i = E_i t - p_i x$  (t and x being time and position  
<sup>198</sup> coordinates). Therefore,

$$\phi_j - \phi_i = E_j t - E_i t - p_j x + p_i x. \quad (1.4)$$

<sup>199</sup> For a relativistic particle,  $E_i \gg m_i$ ,

$$p_i = \sqrt{E_i^2 - m_i^2} \approx E_i - \frac{m_i^2}{2E_i}. \quad (1.5)$$

200 Making the approximations that neutrinos are relativistic, the mass eigenstates  
201 were created with the same energy and that  $x = L$ , where  $L$  is the distance traveled by  
202 the neutrino, Equation 1.4 then becomes

$$\phi_j - \phi_i = \frac{\Delta m_{ij}^2 L}{2E}, \quad (1.6)$$

203 where  $\Delta m_{ij}^2 = m_i^2 - m_j^2$ . This, teamed with further use of unitarity relations results  
204 in Equation 1.3 becoming

$$P(\nu_\alpha \rightarrow \nu_\beta) = \delta_{\alpha\beta} - 4 \sum_{i>j} \Re \left( U_{\alpha i}^* U_{\beta i} U_{\alpha j} U_{\beta j}^* \right) \sin^2 \left( \frac{\Delta m_{ij}^2 L}{4E} \right) + (-) 2 \sum_{i>j} \Im \left( U_{\alpha i}^* U_{\beta i} U_{\alpha j} U_{\beta j}^* \right) \sin \left( \frac{\Delta m_{ij}^2 L}{2E} \right). \quad (1.7)$$

205 Where  $\delta_{\alpha\beta}$  is the Kronecker delta function and the negative sign is included for the  
206 oscillation probability of antineutrinos.

207 Typically, the PMNS matrix is parameterised into three mixing angles, a charge  
208 parity (CP) violating phase  $\delta_{CP}$ , and two Majorana phases  $\alpha_{1,2}$ ,

$$U = \underbrace{\begin{pmatrix} 1 & 0 & 0 \\ 0 & c_{23} & s_{23} \\ 0 & -s_{23} & c_{23} \end{pmatrix}}_{\text{Atmospheric, Accelerator}} \underbrace{\begin{pmatrix} c_{13} & 0 & s_{13}e^{-i\delta_{CP}} \\ 0 & 1 & 0 \\ -s_{13}e^{-i\delta_{CP}} & 0 & c_{13} \end{pmatrix}}_{\text{Reactor, Accelerator}} \underbrace{\begin{pmatrix} c_{12} & s_{12} & 0 \\ -s_{12} & c_{12} & 0 \\ 0 & 0 & 1 \end{pmatrix}}_{\text{Reactor, Solar}} \underbrace{\begin{pmatrix} e^{i\alpha_1/2} & 0 & 0 \\ 0 & e^{i\alpha_2/2} & 0 \\ 0 & 0 & 1 \end{pmatrix}}_{\text{Majorana}}. \quad (1.8)$$

209 Where  $s_{ij} = \sin(\theta_{ij})$  and  $c_{ij} = \cos(\theta_{ij})$ . The oscillation parameters are often  
210 grouped; (1, 2) as “solar”, (2, 3) as “atmospheric” and (1, 3) as “reactor”. Many  
211 neutrino experiments aim to measure the PMNS parameters from a wide array of  
212 origins, as is the purpose of this thesis.

213 The Majorana phase,  $\alpha_{1,2}$ , containing matrix included within Equation 1.8 is only  
214 included for completeness. For an oscillation analysis experiment, any term in this  
215 oscillation probability calculation containing this phase disappears due to taking the  
216 expectation value of the PMNS matrix.

217 A two flavour approximation can be attained when one assumes the third mass  
218 eigenstate is degenerate with another. As discussed in section 1.3, it is found that  
219  $\Delta m_{21}^2 \ll |\Delta m_{31}^2|$ . This results in the two flavour approximation being reasonable for  
220 understanding the features of the oscillation. In this two flavour case, the mixing  
221 matrix becomes,

$$U_{2\text{ Flav.}} = \begin{pmatrix} \cos(\theta) & \sin(\theta) \\ -\sin(\theta) & \cos(\theta) \end{pmatrix}. \quad (1.9)$$

222 This culminates in the oscillation probability,

$$\begin{aligned} P(\nu_\alpha \rightarrow \nu_\alpha) &= 1 - \sin^2(2\theta) \sin^2\left(\frac{\Delta m^2 L}{4E}\right), \\ P(\nu_\alpha \rightarrow \nu_\beta) &= \sin^2(2\theta) \sin^2\left(\frac{\Delta m^2 L}{4E}\right). \end{aligned} \quad (1.10)$$

223 For  $\alpha \neq \beta$ . For a fixed neutrino energy, the oscillation probability is a sinusoidal  
224 function depending upon the distance over which the neutrino propagates. The

225 frequency and amplitude of oscillation are dependent upon the ratio of the  $\Delta m^2 / 4E$   
226 and  $\sin^2 2\theta$ , respectively. For more human-readable units, the maximum oscillation  
227 probability for a fixed value of  $\theta$  is given at  $L[km] / E[GeV] \sim 1.27 / \Delta m^2$ . It is this  
228 calculation that determines the best  $L/E$  value for a given experiment to be designed  
229 around for measurements of a specific value of  $\Delta m^2$ .

### 230 1.2.2 The MSW Effect

231 The theory of neutrino oscillation in a vacuum is described in subsection 1.2.1. How-  
232 ever, the beam neutrinos and atmospheric neutrinos originating from below the  
233 horizon propagate through matter in the Earth. The coherent scattering of neutrinos  
234 from a material target modifies the hamiltonian of the system. This results in a change  
235 in the oscillation probability. Notably, charged current scattering ( $\nu_e + e^- \rightarrow \nu_e + e^-$ ,  
236 propagated by a  $W$  boson) only affects electron neutrinos compared to the neutral  
237 current scattering ( $\nu_l + l^- \rightarrow \nu_l + l^-$ , propagated by a  $Z^0$  boson), interacts through  
238 all neutrino flavours equally. In the two-flavour limit, the effective mixing parameter  
239 becomes

$$\sin^2(2\theta) \rightarrow \sin^2(2\theta_m) = \frac{\sin^2(2\theta)}{(A/\Delta m^2 - \cos(2\theta))^2 + \sin^2(2\theta)}, \quad (1.11)$$

240 where  $A = 2\sqrt{2}G_F N_e E$  with  $N_e$  is the electron density of the medium and  $G_F$  is  
241 Fermi's constant. It is clear to see that there exists a value of  $A = \Delta m^2 \cos(2\theta)$  for  
242  $\Delta m^2 > 0$  which results in a divergent mixing parameter. This resonance is due to  
243 the Mikheyev-Smirnov-Wolfenstein (MSW) effect (or more colloquially, the matter  
244 resonance) which regenerates the electron neutrino component of the neutrino flux  
245 [16–18]. The density at which the resonance occurs is given by

$$N_e = \frac{\Delta m^2 \cos(2\theta)}{2\sqrt{2}G_F E}. \quad (1.12)$$

246 At densities lower than this critical value, the oscillation probability will be much  
247 closer to that of vacuum oscillation. The resonance occurring from the MSW effect  
248 depends on the sign of  $\Delta m^2$ . Therefore, any neutrino oscillation experiment which  
249 observes neutrinos and antineutrinos which have propagated through matter can have  
250 some sensitivity to the ordering of the neutrino mass eigenstates.

### 251 1.3 Neutrino Oscillation Measurements

252 As evidence of beyond standard model physics, the 2015 Nobel Prize in Physics was  
253 awarded to the Super-Kamiokande (SK) [19] and Sudbury Neutrino Observatory  
254 (SNO) [20] collaborations for the first definitive observation of solar and atmospheric  
255 neutrino oscillation [21]. Since then, the field has seen a wide array of oscillation  
256 measurements from a variety of neutrino sources. As seen in subsection 1.2.1, the  
257 neutrino oscillation probability is dependent on the ratio of the propagation baseline,  $L$ ,  
258 to the neutrino energy,  $E$ . It is this ratio that determines the type of neutrino oscillation  
259 a particular experiment is sensitive to.

260 As illustrated in Figure 1.1, there are many neutrino sources that span a wide  
261 range of energies. The least energetic neutrinos are from diffuse supernovae and  
262 terrestrial neutrinos at  $O(1)\text{MeV}$  whereas the most energetic neutrinos originate from  
263 atmospheric and galactic neutrinos of  $> O(1)\text{TeV}$ .

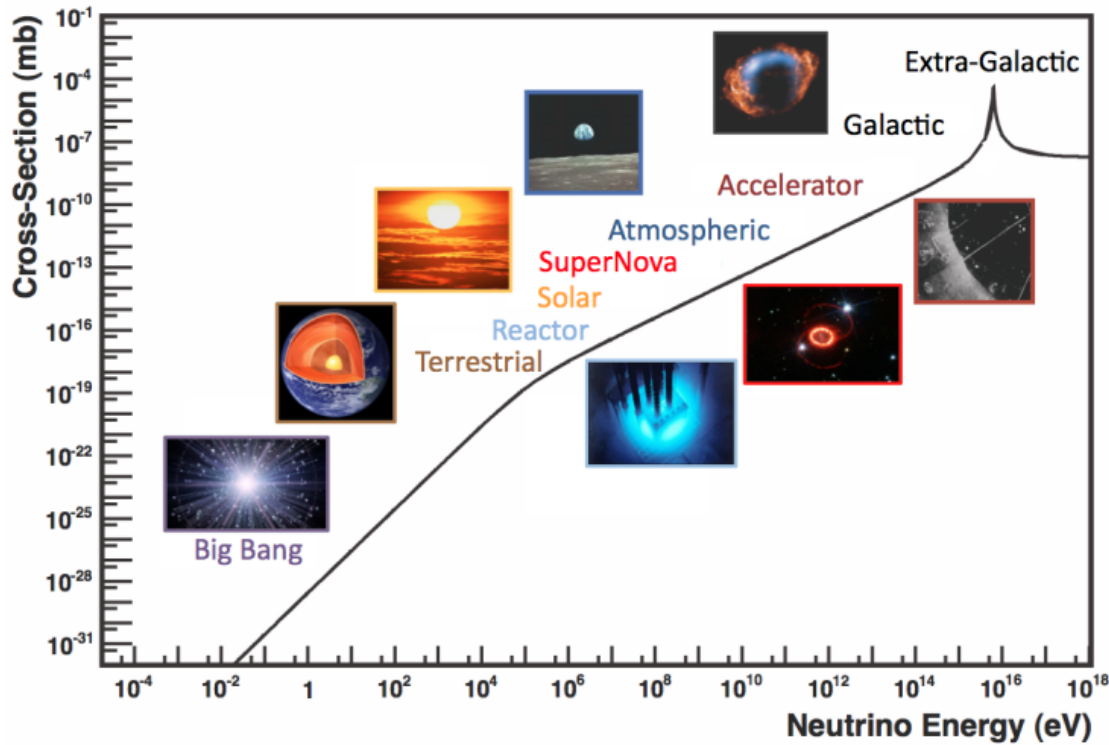


**Figure 1.1:** The cross-section of neutrinos from various natural and man-made sources as a function of neutrino energy. Taken from [22]

### 264 1.3.1 Solar Neutrinos

265 Solar neutrinos are emitted from fusion reaction chains at the center of the Sun. The  
 266 solar neutrino flux, given as a function of neutrino energy for different fusion and  
 267 decay chains is illustrated in Figure 1.2. Whilst proton-proton fusion generates the  
 268 largest flux of neutrinos, the neutrinos are of low energy and are difficult to reconstruct  
 269 due to the IBD interaction threshold of 1.8MeV. Consequently, most experiments focus  
 270 on the neutrinos from the decay of  ${}^8B$  (via  ${}^8B \rightarrow {}^8Be^* + e^+ + \nu_e$ ), which are higher  
 271 energy.

272 The first measurements of solar neutrinos observed a significant reduction in the  
 273 event rate compared to predictions from the Standard Solar Model [24, 25]. The  
 274 proposed solution to this “solar neutrino problem” was  $\nu_e \leftrightarrow \nu_\mu$  oscillations in a

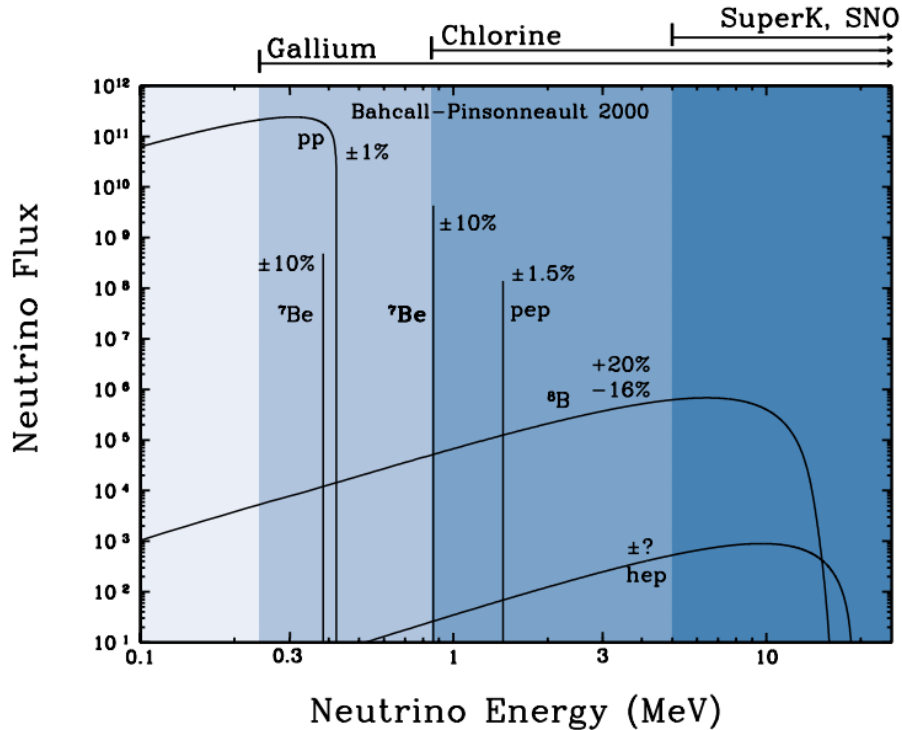


**Figure 1.2:** The solar neutrino flux as a function of neutrino energy for various fusion reactions and decay chains as predicted by the Standard Solar Model. Taken from [23].

275 precursory version of the PMNS model [26]. The Kamiokande [27], Gallex [28] and  
 276 Sage [29] experiments confirmed the  $\sim 0.5$  factor deficit of solar neutrinos.

277 The conclusive solution to this problem was determined by the SNO collabora-  
 278 tion [30]. Using a deuterium water target to observe  ${}^8B$  neutrinos, the event rate of  
 279 charged current (CC), neutral current (NC), and elastic scattering (ES) interactions  
 280 (Given in Equation 1.13) was simultaneously measured. CC events can only occur for  
 281 electron neutrinos, whereas the other interaction channels are agnostic to neutrino  
 282 flavour (Although the ES reaction is more sensitive to electron neutrino interactions).  
 283 This meant that there were direct measurements of the  $\nu_e$  and  $\nu_x$  neutrino flux. It  
 284 was concluded that the CC and ES interaction rates were consistent with the deficit  
 285 previously observed. Most importantly, the NC reaction rate was only consistent with  
 286 the others under the hypothesis of flavour transformation.

$$\begin{aligned}
 \nu_e + d &\rightarrow p + p + e^- & (CC) \\
 \nu_x + d &\rightarrow p + n + \nu_x & (NC) \\
 \nu_x + e^- &\rightarrow \nu_x + e^- & (ES)
 \end{aligned} \tag{1.13}$$

287 Many experiments have since measured the neutrino flux of different interaction  
 288 chains within the sun [31–33]. The most recent measurement was that of CNO neutrinos  
 289 which were recently observed with  $5\sigma$  significance by the Borexino collaboration.  
 290 Future neutrino experiments aim to further these spectroscopic measurements of  
 291 different fusion chains within the Sun [34–36]. Solar neutrinos act as an irreducible  
 292 background for dark matter experiments like DARWIN but oscillation parameter  
 293 measurements can be made [37].

### 294 1.3.2 Atmospheric Neutrinos

295 The interactions of primary cosmic ray protons in Earth’s upper atmosphere generate  
 296 showers of energetic hadrons. These are mostly pions and kaons which when they  
 297 decay produce a natural source of neutrinos spanning energies of MeV to TeV [38].  
 298 This decay is via

$$\begin{aligned}
 \pi^\pm &\rightarrow \mu^\pm + (\nu_\mu, \bar{\nu}_\mu) \\
 \mu^\pm &\rightarrow e^\pm + (\nu_\mu, \bar{\nu}_\mu) + (\nu_e, \bar{\nu}_e)
 \end{aligned} \tag{1.14}$$

299 such that for a single pion decay, three neutrinos are produced. The atmospheric  
 300 neutrino flux energy spectra as predicted by the Bartol [39], Honda [40, 41], and  
 301 FLUKA [42] models are illustrated in Figure 1.3. The flux distribution peaks at an

<sup>302</sup> energy of  $O(10)$ GeV. The uncertainties associated with these models are dominated  
<sup>303</sup> by the hadronic production of kaon and pions as well as the primary cosmic flux.

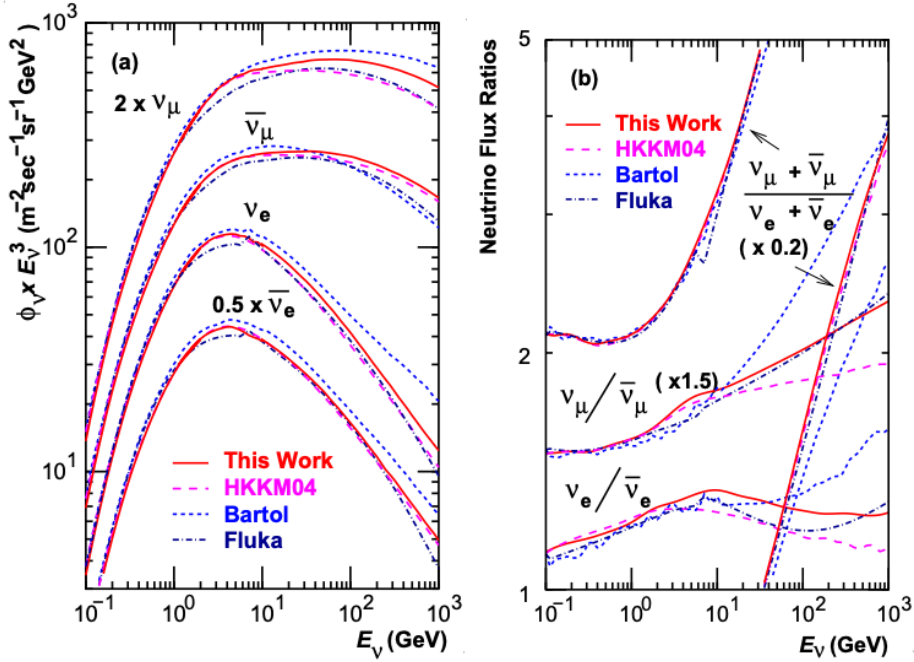


**Figure 1.3:** Left panel: The atmospheric neutrino flux for different neutrino flavours as a function of neutrino energy as predicted by the 2007 Honda model (“This work”) [40], the 2004 Honda model (“HKKM04”) [41], the Bartol model [39] and the FLUKA model [42]. Right panel: The ratio of the muon to electron neutrino flux as predicted by all the quoted models. Both figures taken from [40].

<sup>304</sup> Unlike long-baseline experiments which have a fixed baseline, the distance at-  
<sup>305</sup> mospheric neutrinos propagate is dependent upon the zenith angle at which they  
<sup>306</sup> interact. This is illustrated in Figure 1.4. Neutrinos that are generated directly above  
<sup>307</sup> the detector ( $\cos(\theta) = 1.0$ ) have a baseline equivalent to the height of the atmosphere  
<sup>308</sup> whereas neutrinos that interact directly below the detector ( $\cos(\theta) = -1.0$ ) have to  
<sup>309</sup> travel a length equal to the diameter of the Earth. This means atmospheric neutrinos  
<sup>310</sup> have a baseline that varies from  $O(20)$ km to  $O(6 \times 10^3)$ km. Any neutrino generated  
<sup>311</sup> at or below the horizon will be subject to matter effects as they propagate through the  
<sup>312</sup> Earth.

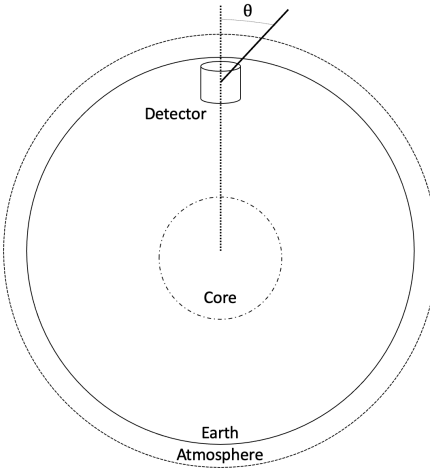


**Figure 1.4:** A diagram illustrating the definition of zenith angle as used in the Super Kamiokande experiment [43].

313      Figure 1.5 highlights the neutrino flux as a function of the zenith angle for different

314      slices of neutrino energy. For medium to high-energy neutrinos (and to a lesser degree

315      for low-energy neutrinos), the flux is approximately symmetric around  $\cos(\theta) = 0$ .

316      To the accuracy of this approximation, the systematic uncertainties associated with

317      atmospheric flux for comparing upward-going and down-going neutrino cancels. This

318      allows the down-going events, which are mostly insensitive to oscillation probabilities,

319      to act as an unoscillated prediction (similar to a near detector in an accelerator neutrino

320      experiment).

321      Precursory hints of atmospheric neutrinos were observed in the mid-1960s search-

322      ing for  $\nu_\mu^{(-)} + X \rightarrow X^* + \mu^\pm$  [44]. This was succeeded with the IMB-3 [45] and

323      Kamiokande [46] experiments which measured the ratio of muon neutrinos com-

324      pared to electron neutrinos  $R(\nu_\mu/\nu_e)$ . Both experiments were found to have a con-

325      sistent deficit of muon neutrinos, with  $R(\nu_\mu/\nu_e) = 0.67 \pm 0.17$  and  $R(\nu_\mu/\nu_e) =$

326       $0.60^{+0.07}_{-0.06} \pm 0.05$ . Super-Kamiokande (SK) [43] extended this analysis by fitting os-

327      cillation parameters in  $P(\nu_\mu \rightarrow \nu_\tau)$  which found best fit parameters  $\sin^2(2\theta) > 0.92$

328      and  $1.5 \times 10^{-3} < \Delta m^2 < 3.4 \times 10^{-3} \text{ eV}^2$ .

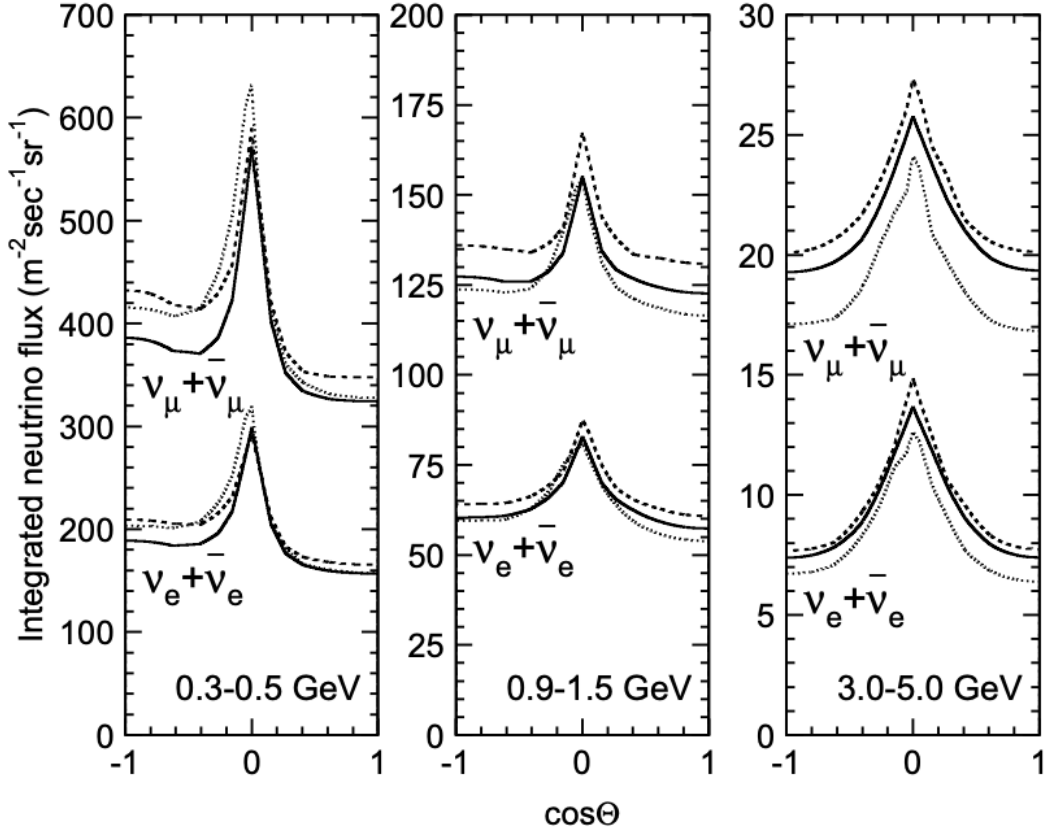


**Figure 1.5:** Predictions of the summed neutrino and antineutrino flux for electron and muon neutrinos from the Bartol [39], Honda [40] and FLUKA [42] models as a function of zenith angle with respect to the detector. Left panel:  $0.3 < E_\nu < 0.5$ . Middle panel:  $0.9 < E_\nu < 1.5$ . Right panel:  $3.0 < E_\nu < 5.0$ . Figures taken from [43].

Since then, atmospheric neutrino experiments have been making precision measurements of the  $\sin^2(\theta_{23})$  and  $\Delta m_{32}^2$  oscillation parameters. Atmospheric neutrino oscillation is dominated by  $P(\nu_\mu \rightarrow \nu_\tau)$ , where SK observed a  $4.6\sigma$  discovery of  $\nu_\tau$  appearance [47]. Figure 1.6 illustrates the current estimates on the atmospheric mixing parameters from a wide range of atmospheric and accelerator neutrino observatories.

### 1.3.3 Accelerator Neutrinos

The concept of using a man-made “neutrino beam” was first realised in 1962 [54]. Since then, many experiments have followed which all use the same fundamental concepts. Typically, a proton beam is aimed at a target producing charged mesons that

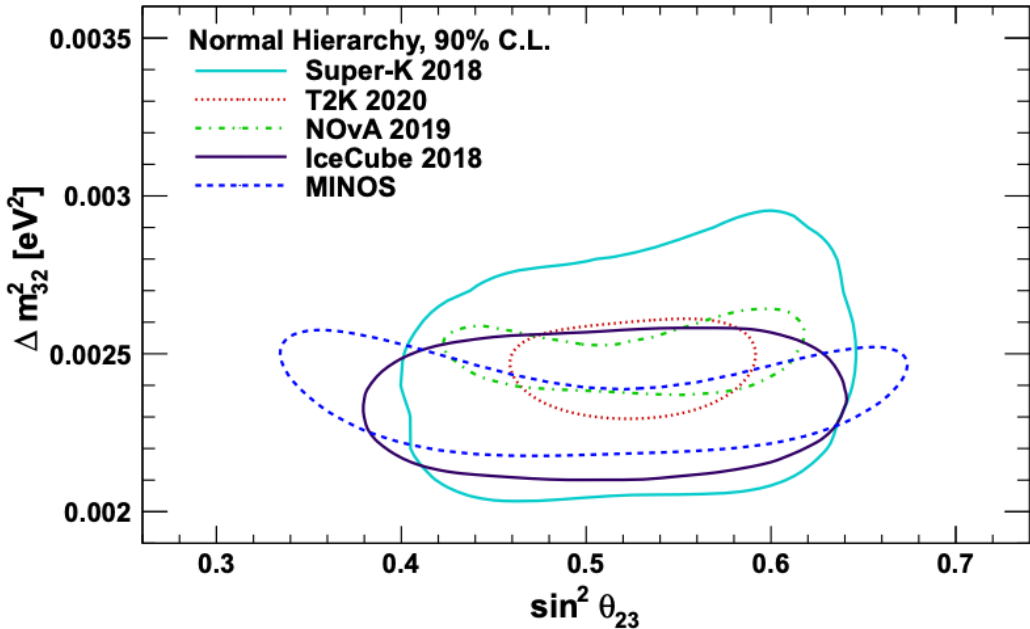


**Figure 1.6:** Constraints on the atmospheric oscillation parameters,  $\sin^2(\theta_{23})$  and  $\Delta m_{23}^2$ , from atmospheric and long baseline experiments: SK [48], T2K [49], NO $\nu$ A [50], IceCube [51] and MINOS [52]. Figure taken from [53].

decay to neutrinos. The mesons can be sign-selected by the use of magnetic focusing horns to generate a neutrino or antineutrino beam. Pions are the primary meson that decay and depending on the orientation of the magnetic field, a muon (anti-)neutrino beam is generated via  $\pi^+ \rightarrow \mu^+ + \nu_\mu$  or  $\pi^- \rightarrow \mu^- + \bar{\nu}_\mu$ . The decay of muons and kaons does result in an irreducible intrinsic electron neutrino background. In T2K, this background contamination is  $O(< 1\%)$  [55]. There is also an approximately  $\sim 5\%$  “wrong-sign” neutrino background of  $\bar{\nu}_\mu$  generated via the same decays.

The energy of each neutrino in the beam is dependent on the energy of the initial proton beam. Therefore, tuning the proton energy allows the neutrino energy to be set to a value that maximises the disappearance oscillation probability in the  $L/E$  term in Equation 1.10. This means that accelerator experiments are typically more sensitive to the mixing parameters as compared to a natural neutrino source. However, the disadvantage compared to atmospheric neutrino experiments is that the baseline has

351 to be shorter due to the lower flux. Consequently, there is typically less sensitivity to  
352 matter effects and the ordering of the neutrino mass eigenstates.

353 A neutrino experiment measures

$$R(\vec{x}) = \Phi(E_\nu) \times \sigma(E_\nu) \times \epsilon(\vec{x}) \times P(\nu_\alpha \rightarrow \nu_\beta), \quad (1.15)$$

354 where  $R(\vec{x})$  is the event rate of neutrinos at position  $\vec{x}$ ,  $\Phi(E_\nu)$  is the flux of neutrinos  
355 with energy  $E_\nu$ ,  $\sigma(E_\nu)$  is the cross-section of the neutrino interaction and  $\epsilon(\vec{x})$  is the  
356 efficiency of the detector. In order to leverage the most out of an accelerator neutrino  
357 experiment, the flux and cross-section systematics need to be constrained. This is  
358 typically done via the use of a “near detector”, situated at a baseline of  $O(1)$ km. This  
359 detector observes the unoscillated neutrino flux and constrains the parameters used  
360 within the flux and cross-section model.

361 The first accelerator experiments to precisely measure oscillation parameters were  
362 MINOS [56] and K2K [57]. These experiments confirmed the  $\nu_\mu \rightarrow \nu_\mu$  oscillations seen  
363 in atmospheric neutrino experiments by finding consistent mixing parameter values  
364 for  $\sin^2(\theta_{23})$  and  $\Delta m_{23}^2$ . The current generation of accelerator neutrino experiments,  
365 T2K and NOvA extended this field by observing  $\bar{\nu}_\mu \rightarrow \bar{\nu}_e$  and lead the sensitivity to at-  
366 mospheric mixing parameters as seen in Figure 1.6 [58]. The two experiments differ in  
367 their peak neutrino energy, baseline, and detection technique. The NOvA experiment  
368 is situated at a baseline of 810km from the NuMI beamline which delivers 2GeV neu-  
369 trinos. The T2K neutrino beam is peaked around 0.6GeV and propagates 295km. The  
370 NOvA experiment also uses functionally identical detectors (near and far) which allow  
371 the approximate cancellation of detector systematics whereas T2K uses a plastic scin-  
372 tillator technique at the near detector and a water Cherenkov far detector. The future

<sup>373</sup> generation experiments DUNE [59] and Hyper-Kamiokande [60] will succeed these  
<sup>374</sup> experiments as the high-precision era of neutrino oscillation parameter measurements  
<sup>375</sup> develops.

<sup>376</sup> Several anomalous results have been observed in the LSND [9] and MiniBooNE [10]  
<sup>377</sup> detectors which were designed with purposefully short baselines. Parts of the neu-  
<sup>378</sup> trino community attributed these results to oscillations induced by a fourth “sterile”  
<sup>379</sup> neutrino [61] but several searches in other experiments, MicroBooNE [62] and KAR-  
<sup>380</sup> MEN [63], found no hints of additional neutrino species. The solution to the anomalous  
<sup>381</sup> results are still being determined.

### <sup>382</sup> 1.3.4 Reactor Neutrinos

<sup>383</sup> As illustrated in the first discovery of neutrinos (section 1.1), nuclear reactors are a very  
<sup>384</sup> useful man-made source of electron antineutrinos. For reactors that use low-enriched  
<sup>385</sup> uranium  $^{235}\text{U}$  as fuel, the antineutrino flux is dominated by the  $\beta$ -decay fission of  $^{235}\text{U}$ ,  
<sup>386</sup>  $^{238}\text{U}$ ,  $^{239}\text{Pu}$  and  $^{241}\text{Pu}$  [64] as illustrated in Figure 1.7.

<sup>387</sup> Due to their low energy, reactor electron antineutrinos predominantly interact  
<sup>388</sup> via the inverse  $\beta$ -decay (IBD) interaction. The typical signature contains two signals  
<sup>389</sup> delayed by  $O(200)\mu\text{s}$ ; firstly the prompt photons from positron annihilation, and  
<sup>390</sup> secondly the photons emitted ( $E_{tot}^\gamma = 2.2\text{MeV}$ ) from de-excitation after neutron capture  
<sup>391</sup> on hydrogen. Searching for both signals improves the detector’s ability to distinguish  
<sup>392</sup> between background and signal events [66]. Recently, SK included gadolinium dopants  
<sup>393</sup> into the ultra-pure water to increase the energy released from the photon cascade to  
<sup>394</sup>  $\sim 8\text{MeV}$  and reduce the time of the delayed signal to  $\sim 28\mu\text{s}$ .

<sup>395</sup> There are many short baseline experiments ( $L \sim O(1)\text{km}$ ) that have measured the  
<sup>396</sup>  $\sin^2(\theta_{13})$  and  $\Delta m_{23}^2$  oscillation parameters. Daya Bay [67], RENO [68] and Double

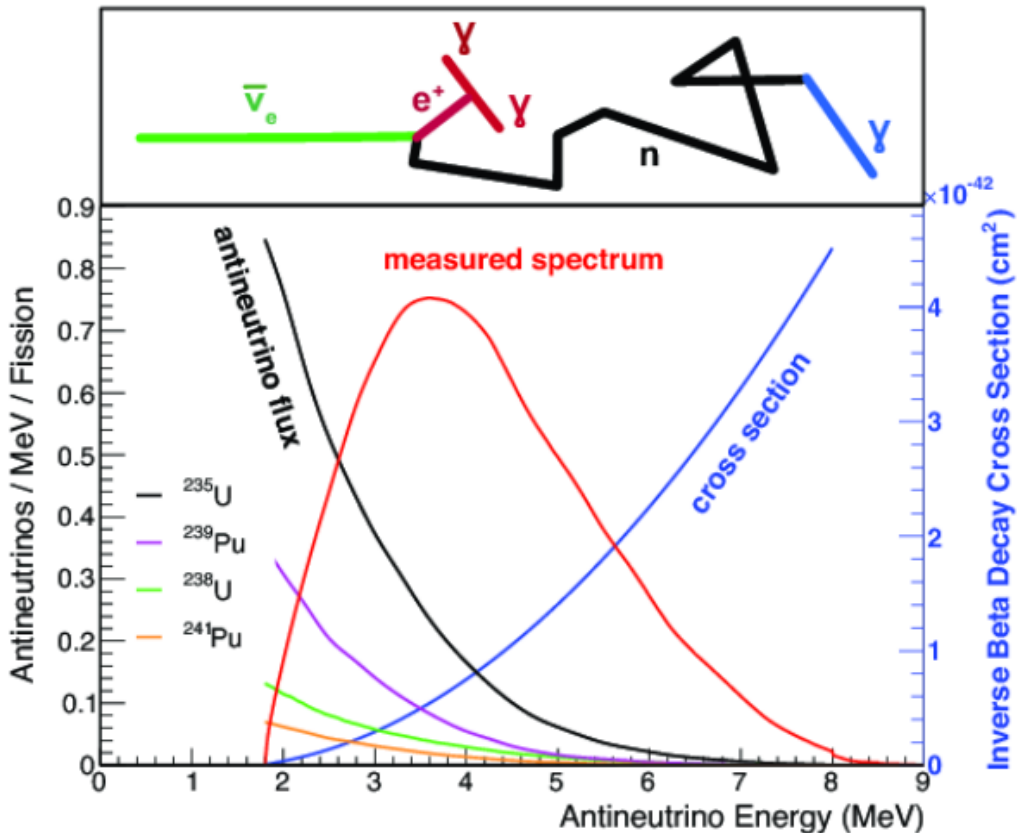


**Figure 1.7:** Reactor electron antineutrino fluxes for  $^{235}\text{U}$  (Black),  $^{238}\text{U}$  (Green),  $^{239}\text{Pu}$  (Purple), and  $^{241}\text{Pu}$  (Orange) isotopes. The inverse  $\beta$ -decay cross-section (Blue) and corresponding measurable neutrino spectrum (Red) are also given. Top panel: Schematic of Inverse  $\beta$ -decay interaction including the eventual capture of the emitted neutron. This capture emits a  $\gamma$ -ray which provides a second signal of the event. Taken from [65].

Chooz [69] have all provided precise measurements, with the first discovery of a non-zero  $\theta_{13}$  made by Daya Bay and RENO (and complimented by T2K [69]). The constraints on  $\sin^2(\theta_{13})$  by the reactor experiments lead the field and are often used as external inputs to accelerator neutrino experiments to improve their sensitivity to  $\delta_{CP}$  and mass hierarchy determination. JUNO-TAO [70], a small collaboration within the larger JUNO experiment, is a next-generation reactor experiment that aims to precisely measure the isotopic antineutrino yields from the different fission chains. Alongside this, it aims to explain the ‘5MeV excess’ [71–73] by conducting a search for sterile neutrinos with a mass scale of around 1eV.

406        Kamland [74] is the only experiment to have observed reactor neutrinos using a  
407        long baseline (flux weighted averaged baseline of  $L \sim 180\text{km}$ ) which allows it to have  
408        sensitivity to  $\Delta m_{12}^2$ . Combined with the SK solar neutrino experiment, the combined  
409        analysis puts the most stringent constraint on  $\Delta m_{12}^2$  [75] which is used as a prior  
410        uncertainty within accelerator neutrino experiments.

<sup>411</sup> **Chapter 2**

<sup>412</sup> **T2K and SK Experiment Overview**

<sup>413</sup> As the successor of the Kamiokande experiment, the Super-Kamiokande (SK) collaboration has been leading atmospheric neutrino oscillation analyses for over two decades.  
<sup>414</sup> The detector has provided some of the strongest constraints on proton decay limits  
<sup>415</sup> and as well as the first precise measurements of the  $\Delta m_{23}^2$  and  $\sin^2(\theta_{23})$  neutrino  
<sup>416</sup> oscillation parameters. Despite this, the ability of the detector to low-energy neutrino  
<sup>417</sup> events has been significantly improved with the recent gadolinium doping of the  
<sup>418</sup> ultra-pure water target. section 2.1 describes the history, detection technique, and  
<sup>419</sup> operation of the SK detector.

<sup>421</sup> The Tokai-to-Kamioka (T2K) experiment was one of the first long-baseline experiments to use both neutrino and antineutrino beams to precisely measure the  
<sup>422</sup> charge parity violation within the neutrino sector. With the SK detector observing  
<sup>423</sup> the oscillated neutrino flux, the T2K experiment observed the first hints of a non-zero  
<sup>424</sup>  $\sin^2(\theta_{13})$  measurement and continues to lead the field with the constraints it provides  
<sup>425</sup> on  $\sin^2(\theta_{13})$ ,  $\sin^2(\theta_{23})$ ,  $\Delta m_{23}^2$  and  $\delta_{CP}$ . section 2.2 documents the techniques  
<sup>426</sup> which T2K uses in generating its neutrino beam as well as the ‘near-detector’ used to  
<sup>427</sup> constrain the flux and cross-section parameters invoked within the systematic models.

<sup>429</sup> **2.1 The Super-Kamiokande Experiment**

<sup>430</sup> The SK experiment began taking data in 1996 [76] and has had many modifications  
<sup>431</sup> throughout its lifespan. There have been seven defined periods of data taking as

noted in Table 2.1. Data taking began in SK-I which ran for five years. Between the SK-I and SK-II periods, a significant proportion of the PMTs were damaged during maintenance. Those that survived were equally distributed throughout the detector in the SK-II era, which resulted in a reduced photo-coverage. From SK-III onwards, repairs to the detector meant the full suite of PMTs was operational. Before the start of SK-IV, the data acquisition and electronic systems were upgraded. Between SK-IV and SK-V, a significant effort was placed into tank open maintenance and repair/replacement of defective PMTs, a task for which the author of this thesis was required. Consequently, the detector conditions were significantly different between the two operational periods. SK-VI saw the start of the 0.01% gadolinium doped water. SK-VII, which started during the writing of this thesis, has increased the gadolinium concentration to 0.03% for continued operation. [DB: Link to Linyan's talk from Nu2022.](#)

Period	Start Date	End Date	Live-time (days)
I	April 1996	July 2001	1489.19
II	October 2002	October 2005	798.59
III	July 2006	September 2008	518.08
IV	September 2008	May 2018	3244.4
V	January 2019	July 2020	461.02
VI	July 2020	May 2022	583.3
VII	May 2022	Ongoing	N/A

**Table 2.1:** The various SK periods and respective live-time. The SK-VI live-time is calculated until 1<sup>st</sup> April 2022. SK-VII started during the writing of this thesis.

### 2.1.1 The SK Detector

The basic structure of the Super-Kamiokande (SK) detector is a cylindrical tank with a diameter 39.3m and height 41.1m filled with ultrapure water [77]. A diagram of the significant components of the SK detector is illustrated in Figure 2.1. The SK detector

is situated in the Kamioka mine in Gifu, Japan. The mine is underground with roughly 1km rock overburden (2.7km water equivalent overburden) [78]. At this depth, the rate of cosmic ray muons is significantly decreased to a value of  $\sim 2\text{Hz}$ . The top of the tank is covered with stainless steel which is designed as a working platform for maintenance, calibration, and location for high voltage and data acquisition electronics.

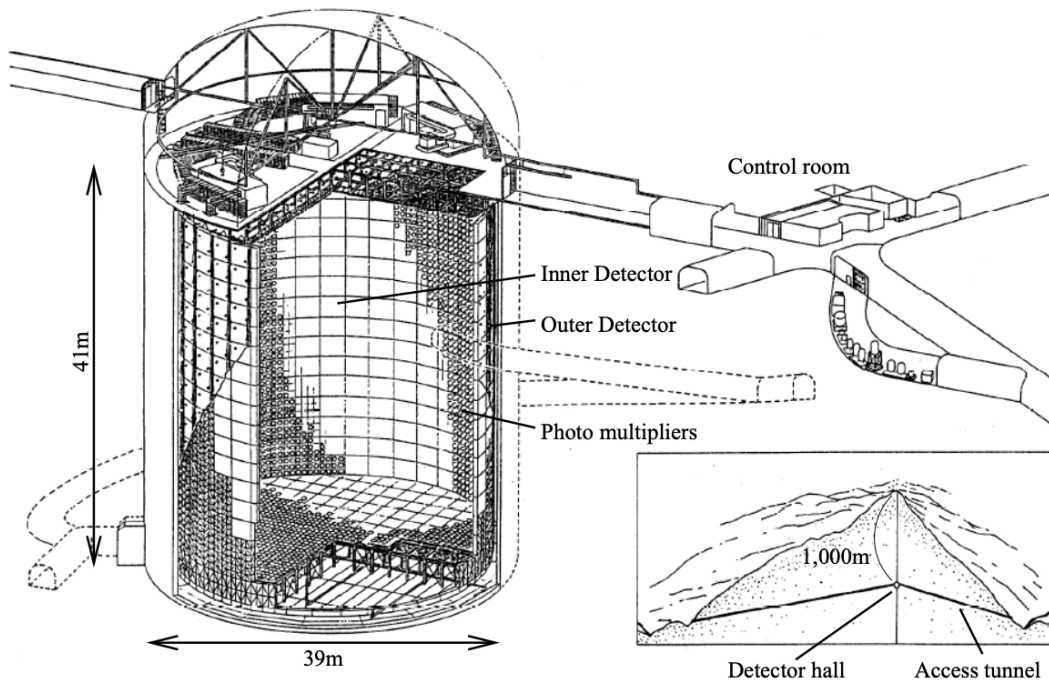


**Figure 2.1:** A schematic diagram of the Super-Kamiokande Detector. Taken from [79].

A smaller cylindrical structure (36.2m diameter, 33.8m height) is situated inside the tank, with an approximate 2m gap between this structure and the outer tank wall. The purpose of this structure is to support the photomultiplier tubes (PMTs). The volume inside and outside the support structure is referred to as the inner detector (ID) and outer detector (OD), respectively. In the SK-IV era, the ID and OD are instrumented by 11,129 50cm and 1,885 20cm PMTs respectively [77]. The ID contains a 32kton mass of water. Many analyses performed at SK use a “fiducial volume” defined by the volume of water inside the ID excluding some distance to the ID wall. This reduces the volume of the detector which is sensitive to neutrino events but reduces radioactive

463 backgrounds and allows for better reconstruction performance. The nominal fiducial  
464 volume is defined as the area contained inside 2m from the ID wall for a total of  
465 22.5kton water [80].

466 The two regions of the detector (ID and OD) are optically separated with opaque  
467 black plastic. The purpose of this is to determine whether a track entered or exited  
468 the ID. This allows cosmic ray muons and partially contained events to be tagged and  
469 separated from neutrino events entirely contained within the ID. This black plastic is  
470 also used to cover the area between the ID PMTs to reduce photon reflection from the  
471 ID walls. Opposite to this, the OD is lined with a reflective material to allow photons to  
472 reflect around inside the OD until collected by one of the PMTs. Furthermore, each OD  
473 PMT is backed with  $50 \times 50\text{cm}$  plates of wavelength shifting acrylic which increases  
474 the efficiency of light collection [78].

475 In the SK-IV data-taking period, the photocathode coverage of the detector, or the  
476 fraction of the ID wall instrumented with PMTs, is  $\sim 40\%$  [78]. The PMTs have a  
477 quantum efficiency (the ratio of detected electrons to incident photons) of  $\sim 21\%$  for  
478 photons with wavelengths of  $360\text{nm} < \lambda < 390\text{nm}$ . The proportion of photoelectrons  
479 that produce a signal in the dynode of a PMT, termed the collection efficiency, is  
480  $> 70\%$  [78]. The PMTs used within SK are most sensitive to photons with wavelength  
481  $300\text{nm} \leq \lambda \leq 600\text{nm}$  [78]. One disadvantage of using PMTs as the detection media  
482 is that the Earth's geomagnetic field can modify its response. Therefore, a set of  
483 compensation coils is built around the inner surface of the detector to mitigate this  
484 effect [81].

485 As mentioned, the SK detector is filled with ultrapure water, which in a perfect  
486 world would contain no impurities. However, bacteria and organic compounds can  
487 significantly degrade the water quality. This decreases the attenuation length which  
488 reduces the total number of photons that hit a PMT. To combat this, a sophisticated

489 water treatment system has been developed [78, 82]. UV lights, mechanical filters, and  
490 membrane degasifiers are used to reduce the bacteria, suspended particulates, and  
491 radioactive materials from the water. The flow of water within the tank is also critical  
492 as it can remove stagnant bacterial growth or build-up of dust on the surfaces within  
493 the tank. Gravity drifts impurities in the water towards the bottom of the tank which,  
494 if left uncontrolled, can create asymmetric water conditions between the top and  
495 bottom of the tank. Typically, the water entering the tank is cooled below the ambient  
496 temperature of the tank to control convection and inhibit bacteria growth. Furthermore,  
497 the dark noise hits within PMTs is sensitive to the PMT temperature [83] so controlling  
498 the temperature gradients within the tank is beneficial for stable measurements.

499 SK-VI is the first phase of the SK experiment to use gadolinium dopants within  
500 the ultrapure water [DB: Link to Linyan's talk at Nu2022](#). As such, the SK water  
501 system had to be replaced to avoid removing the gadolinium concentrate from the  
502 ultrapure water [84]. For an inverse  $\beta$ -decay (IBD) interaction in a water target, the  
503 emitted neutron is thermally captured on hydrogen. This process releases 2.2MeV  $\gamma$   
504 rays which are difficult to detect due to Compton scattered electrons from a  $\gamma$  ray of  
505 this energy is very close to the Cherenkov threshold, limiting the number of photons  
506 produced. Thermal capture of neutrons on gadolinium generates  $\gamma$  rays with higher  
507 energy meaning they are more easily detected. SK-VI has 0.01% Gd loading (0.02%  
508 gadolinium sulphate by mass) which causes  $\approx$  50% of neutrons emitted by IBD to  
509 be captured on gadolinium [85, 86]. Whilst predominantly useful for low energy  
510 analyses, Gd loading allows better  $\nu/\bar{\nu}$  separation for atmospheric neutrino event  
511 selections [87]. Efforts are currently in place to increase the gadolinium concentrate to  
512 0.03% for  $\approx$  75% neutron capture efficiency on gadolinium [DB: Link to Mark's talk at](#)  
513 [Nu2022](#). The final stage of loading targets 0.1% concentrate.

## 514 2.1.2 Calibration

515 The calibration of the SK detector is documented in [77] and summarised below. The  
516 analysis presented within this thesis is dependent upon ‘high energy events’ (Charged  
517 particles with  $O(> 100)\text{MeV}$  momenta). These are events that are expected to generate  
518 a larger number of photons such that each PMT will be hit with multiple photons.  
519 The reconstruction of these events depends upon the charge deposited within each  
520 PMT and the timing response of each individual PMT. Therefore, the most relevant  
521 calibration techniques to this thesis are outlined.

522 Before installation, 420 PMTs were calibrated to have identical charge responses  
523 and then distributed throughout the tank in a cross-shape pattern (As illustrated by  
524 Figure 2.2). These are used as a standardised measure for the rest of the PMTs installed  
525 at similar geometric positions within SK to be calibrated against. To perform this  
526 calibration, a xenon lamp is located at the center of the SK tank which flashes uniform  
527 light at 1Hz. This allows for geometrical effects, water quality variation, and timing  
528 effects to be measured in-situ throughout normal data-taking periods.

529 When specifically performing calibration of the detector (in out-of-data taking  
530 mode), the water in the tank was circulated to avoid top/bottom asymmetric water  
531 quality. Any non-uniformity within the tank significantly affects the PMT hit proba-  
532 bility through scattering or absorption. This becomes a dominant effect for the very  
533 low-intensity light sources discussed later which are designed such that only one  
534 photon is incident upon a given PMT.

535 The “gain” of a PMT is defined as the ratio of the total charge of the signal produced  
536 compared to the charge of photoelectrons emitted by the photocathodes within the  
537 PMT. To calibrate the signal of each PMT, the “relative” and “absolute” gain values are

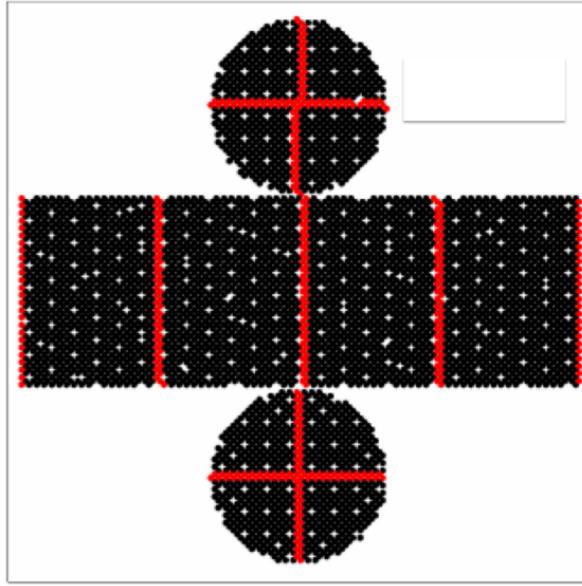


**Figure 2.2:** The location of “standard PMTs” (red) inside the SK detector. Taken from [77].

538 measured. The relative gain is the variation of gain among each of the PMTs whereas  
 539 the absolute gain is the average gain of all PMTs.

540 The relative gain is calibrated as follows. A laser is used to generate two measure-  
 541 ments; a high-intensity flash that illuminates every PMT with a sufficient number of  
 542 photons, and a low-intensity flash in which only a small number of PMTs collect light.  
 543 The first measurement creates an average charge,  $Q_{obs}(i)$  on PMT  $i$ , whereas the second  
 544 measurement ensures that each hit PMT only generates a single photoelectron. For the  
 545 low-intensity measurement, the number of times each PMT records a charge larger  
 546 than 1/4 photoelectrons,  $N_{obs}(i)$ , is counted. The values measured can be expressed as

$$\begin{aligned} Q_{obs}(i) &\propto I_H \times f(i) \times \epsilon(i) \times G(i), \\ N_{obs}(i) &\propto I_L \times f(i) \times \epsilon(i), \end{aligned} \tag{2.1}$$

547 Where  $I_H$  and  $I_L$  is the intensity of the high and low flashes,  $f(i)$  is the acceptance  
 548 efficiency of the  $i^{\text{th}}$  PMT,  $\epsilon(i)$  is the product of the quantum and collection efficiency

549 of the  $i^{\text{th}}$  PMT and  $G(i)$  is the gain of the  $i^{\text{th}}$  PMT. The relative gain for each PMT can  
550 determined by taking the ratio of these quantities.

551 The absolute gain calibration is performed by observing fixed energy  $\gamma$ -rays of  
552  $E_{\gamma} \sim 9\text{MeV}$  emitted isotropically from neutron capture on a NiCf source situated at  
553 the center of the detector. This generates a photon yield of about 0.004 photoelec-  
554 trons/PMT/event, meaning that  $> 99\%$  of PMT signals are generated from single  
555 photoelectrons. A charge distribution is generated by performing this calibration over  
556 all PMTs, and the average value of this distribution is taken to be the absolute gain  
557 value.

558 As mentioned in subsection 2.1.1, the average quantum and collection efficiency  
559 for the SK detector is  $\sim 21\%$  and  $> 70\%$  respectively. However, these values do differ  
560 between each PMT and need to be calibrated accordingly. Consequently, the NiCf  
561 source is also used to calibrate the “quantum  $\times$  collection” efficiency (denoted “QE”)  
562 value of each PMT. The NiCf low-intensity source is used as the PMT hit probability  
563 is proportional to the QE ( $N_{\text{obs}}(i) \propto \epsilon(i)$  in Equation 2.1). A Monte Carlo prediction  
564 which includes photon absorption, scattering, and reflection is made to estimate the  
565 number of photons incident on each PMT and the ratio of the number of predicted  
566 to observed hits is calculated. The difference is attributed to the QE efficiency of that  
567 PMT. This technique is extended to calculate the relative QE efficiency by normalizing  
568 the average of all PMTs which removes the dependence on the light intensity.

569 Due to differing cable lengths and readout electronics, the timing response between  
570 a photon hitting the PMT and the signal being captured by the data acquisition can be  
571 different between each PMT. Due to threshold triggers (Described in subsection 2.1.3),  
572 the time at which a pulse reaches a threshold is dependent upon the size of the pulse.  
573 This is known as the ‘time-walk’ effect and also needs to be accounted for in each PMT.  
574 To calibrate the timing response, a pulse of light with width 0.2ns is emitted into the

575 detector through a diffuser Two-dimensional distributions of time and pulse height  
576 (or charge) are made for each PMT and are used to calibrate the timing response. This  
577 is performed in-situ whilst data taking with the light source pulsing at 0.03Hz.

578 The top/bottom water quality asymmetry is measured using the NiCf calibration  
579 data and cross-referencing these results to the “standard PMTs”. The water attenuation  
580 length is continuously measured by the rate of vertically-downgoing cosmic-ray  
581 muons which enter via the top of the tank.

### 582 2.1.3 Data Acquisition and Triggering

583 Dark noise is the phenomenon where a PMT registers a pulse that is consistent with a  
584 single photoelectron emitted from photon detection despite the PMT being in complete  
585 darkness. This is predominately caused by two processes. Firstly there is intrinsic  
586 dark noise which is where photoelectrons gain enough thermal energy to be emitted  
587 from the photocathode, and secondly, the radioactive decay of contaminants inside the  
588 structure of the PMT. Typical dark noise rate for PMTs used within SK are  $O(3)$ kHz [78]  
589 which equates to about 12 dark noise hits per 220ns [88]. This is lower than the  
590 expected number of photons generated for a ‘high energy event’ (As described in  
591 subsection 2.1.4) but instability in this value can cause biases in reconstruction.

592 The analysis presented in this thesis only uses the SK-IV period of the SK exper-  
593 iment so this subsection focuses on the relevant points of the data acquisition and  
594 triggering systems to that SK period. The earlier data acquisition and triggering  
595 systems are documented in [89, 90].

596 Before the SK-IV period started, the existing front-end electronics were replaced  
597 with “QTC-Based Electrons with Ethernet, QBEE” systems [91]. When the QBEE  
598 observes a signal above a 1/4 photoelectron threshold, the charge-to-time (QTC)

599 converter generates a rectangular pulse. The start of the rectangular pulse indicates  
 600 the time at which the analog photoelectron signal was received and the width of the  
 601 pulse indicates the total charge integrated throughout the signal. This is then digitized  
 602 by time-to-digital converters and sent to the “front-end” PCs. The digitized signal  
 603 from every QBEE is then chronologically ordered and sent to the “merger” PCs. It is  
 604 the merger PCs that apply the software trigger. Any triggered events are passed to the  
 605 “organizer” PC. This sorts the data stream of multiple merger PCs into chronologically  
 606 ordered events which are then saved to disk. The schematic of data flow from PMTs to  
 607 disk is illustrated in Figure 2.3.

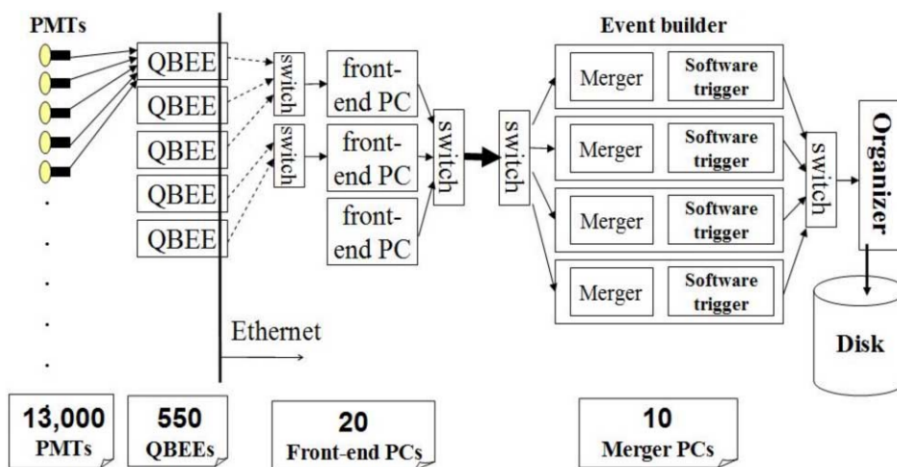


**Figure 2.3:** Schematic view of the data flow through the data acquisition and online system.  
 Taken from [92].

608 The software trigger (described in [93]) operates by determining the number of  
 609 PMT hits within a 200ns sliding window,  $N_{200}$ , coincides with the maximum time that  
 610 a Cherenkov photon would take to traverse the length of the SK tank [90]. For lower  
 611 energy events that generate fewer photons, this technique is useful for eliminating  
 612 background processes like dark noise and radioactive decay which would be expected  
 613 to separate in time. When the value of  $N_{200}$  exceeds some threshold, a software trigger  
 614 is issued. There are several trigger thresholds used within the SK-IV period which are  
 615 detailed in Table 2.2. If one of these thresholds is met, the PMT hits within an extended

time window are also read out and saved to disk. In the special case of an event that exceeds the SHE trigger but does not exceed the OD trigger, the AFT trigger looks for delayed coincidences of 2.2MeV gamma rays emitted from neutron capture in a  $535\mu\text{s}$  window after the SHE trigger. A similar but more complex “Wideband Intelligent Trigger (WIT)” has been deployed and is described in [88].

Trigger	Acronym	Condition	Extended time window ( $\mu\text{s}$ )
Super Low Energy	SLE	>34/31 hits	1.3
Low Energy	LE	>47 hits	40
High Energy	HE	>50 hits	40
Super High Energy	SHE	>70/58 hits	40
Outer Detector	OD	>22 hits in OD	N/A

**Table 2.2:** The trigger thresholds and extended time windows saved around an event which were utilised throughout the SK-IV period. The exact thresholds can change and the values listed here represent the thresholds at the start and end of the SK-IV period.

### 2.1.4 Cherenkov Radiation

Cherenkov light is emitted from any highly energetic charged particle traveling with relativistic velocity,  $\beta$ , greater than the local speed of light in a medium [94]. Cherenkov light is formed at the surface of a cone with characteristic pitch angle,

$$\cos(\theta) = \frac{1}{\beta n}. \quad (2.2)$$

where  $n$  is the refractive index of the medium. Consequently, the Cherenkov momentum threshold,  $P_{thres}$ , is dependent upon the mass,  $m$ , of the charged particle moving through the media,

$$P_{thres} = \frac{m}{\sqrt{n^2 - 1}} \quad (2.3)$$

628 For water, where  $n = 1.33$ , the Cherenkov threshold momentum and energy for  
 629 various particles are given in Table 2.3. In contrast,  $\gamma$ -rays are detected indirectly via  
 630 the combination of photons generated by Compton scattering and pair production.  
 631 The threshold for detection in the SK detector is typically higher than the threshold  
 632 for photon production. This is due to the fact that the attenuation of photons in the  
 633 water means that typically  $\sim 75\%$  of Cherenkov photons reach the ID PMTs. Then the  
 634 collection and quantum efficiencies described in subsection 2.1.1 result in the number  
 635 of detected photons being lower than the number of photons which reach the PMTs.

Particle	Threshold Momentum (MeV)	Threshold Energy (MeV)
Electron	0.5828	0.7751
Muon	120.5	160.3
Pion	159.2	211.7
Proton	1070.0	1423.1

**Table 2.3:** The threshold momentum and energy for a particle to generate Cherenkov light in ultrapure water, as calculated in Equation 2.2 in ultrapure water which has refractive index  $n = 1.33$ .

636 The Frank-Tamm equation [95] describes the relationship between the number of  
 637 Cherenkov photons generated per unit length,  $dN/dx$ , the wavelength of the photons  
 638 generated,  $\lambda$ , and the relativistic velocity of the charged particle,

$$\frac{d^2N}{dxd\lambda} = 2\pi\alpha \left(1 - \frac{1}{n^2\beta^2}\right) \frac{1}{\lambda^2}. \quad (2.4)$$

639 where  $\alpha$  is the fine structure constant. For a 100MeV momentum electron, approx-  
 640 imately 330 photons will be produced per centimeter in the  $300\text{nm} \leq \lambda \leq 700\text{nm}$   
 641 region which the ID PMTs are most sensitive to [78].

## 642 2.2 The Tokai to Kamioka Experiment

643 The Tokai to Kamioka (T2K) experiment is a long-baseline neutrino oscillation experi-  
 644 ment located in Japan. Proposed in the early 2000s [96, 97] to replace K2K [98], T2K  
 645 was designed to observe electron neutrino appearance whilst precisely measuring  
 646 the oscillation parameters associated with muon neutrino disappearance [99]. The  
 647 experiment consists of a neutrino beam generated at the Japan Proton Accelerator  
 648 Research Complex (J-PARC), a suite of near detectors situated 280m from the beam  
 649 target, and the Super Kamiokande far detector positioned at a 295km baseline. The  
 650 cross-section view of the T2K experiment is drawn in Figure 2.4.

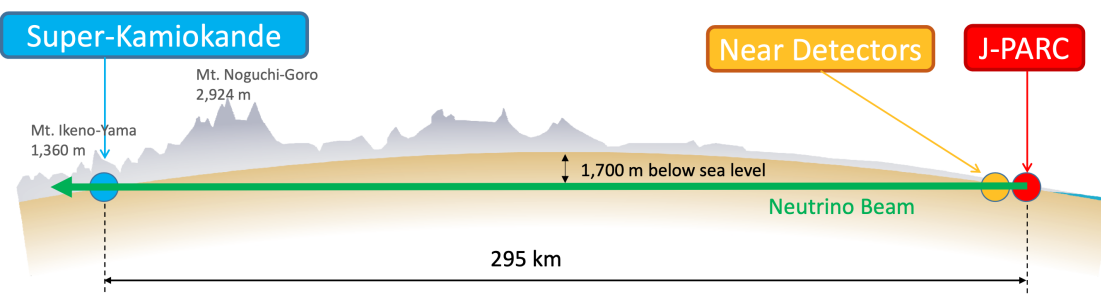
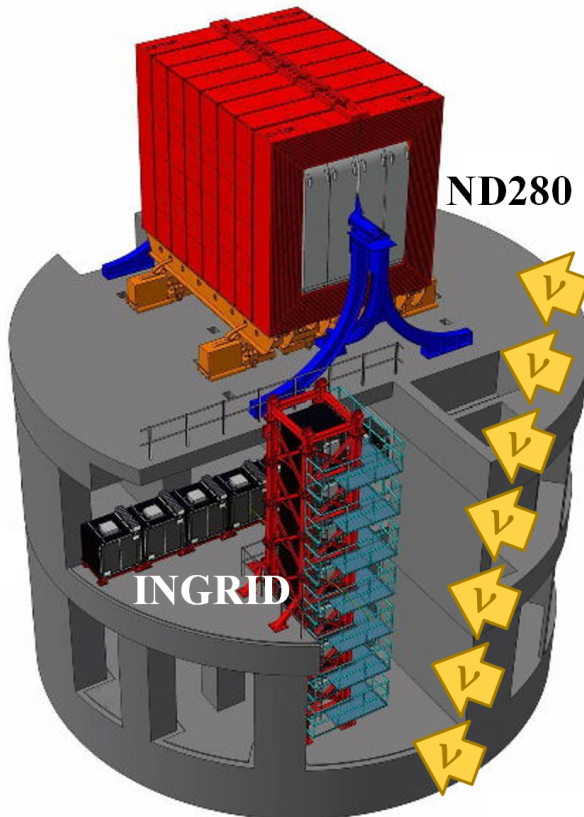


Figure 2.4: The cross-section view of the Tokai to Kamioka experiment illustrating the beam generation facility at J-PARC, the near detector situated at a baseline of 280m and the Super Kamiokande far detector situated 295km from the beam target.

651 The T2K collaboration makes world-leading measurements of the  $\sin^2(\theta_{23})$ ,  $\Delta m_{23}^2$   
 652 , and  $\delta_{CP}$  oscillation parameters. Improvements in the precision and accuracy of pa-  
 653 rameter estimates are still being made by including new data samples and developing  
 654 the models which describe the neutrino interactions and detector responses DB: [Link](#)  
 655 to Christophe's slides from Nu2022. Electron neutrino appearance was first observed

656 at T2K in 2014 [100] which accompanied a  $7.3\sigma$  significance of a non-zero  $\sin^2(\theta_{13})$   
 657 measurement.

658 The near detectors provide constraints on the beam flux and cross-section model  
 659 parameters used within the fit by observing the unoscillated neutrino beam. There  
 660 are a host of detectors situated in the near detector hall (As illustrated in Figure 2.5);  
 661 ND280 (subsection 2.2.2), INGRID (subsection 2.2.3), NINJA [101], WAGASCI [102],  
 662 and Baby-MIND [103]. The latter three are not currently used within the oscillation  
 663 analysis presented within this thesis.



**Figure 2.5:** The near detector suite for the T2K experiment showing the ND280 and INGRID detectors. The distance between the detectors and the beam target is 280m.

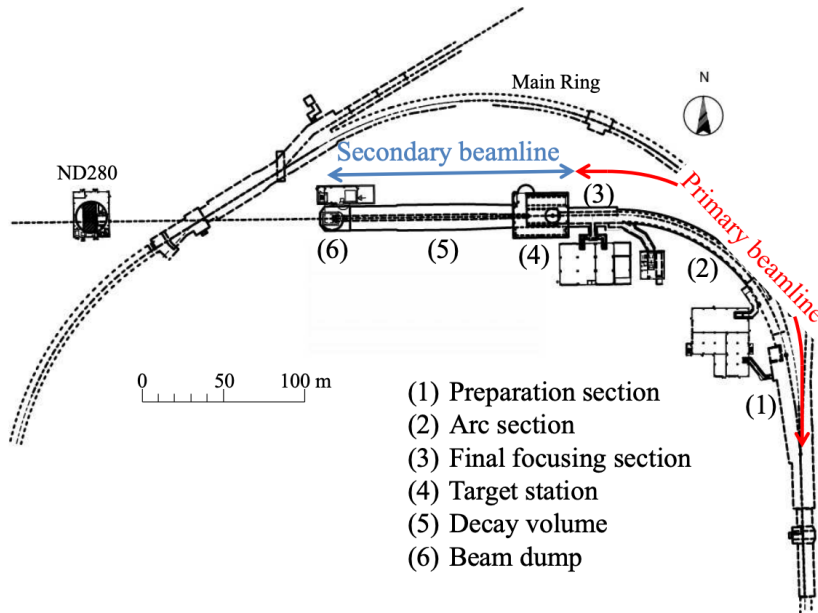
664 Whilst this thesis presents the ND280 in terms of its purpose for the oscillation  
 665 analysis, the detector can also make many cross-section measurements at neutrino  
 666 energies of  $O(1)\text{GeV}$  for the different targets within the detector [104, 105]. These

667 measurements are of equal importance as they can lead the way in determining the  
668 model parameters used in the interaction models for the future high-precision era of  
669 neutrino physics.

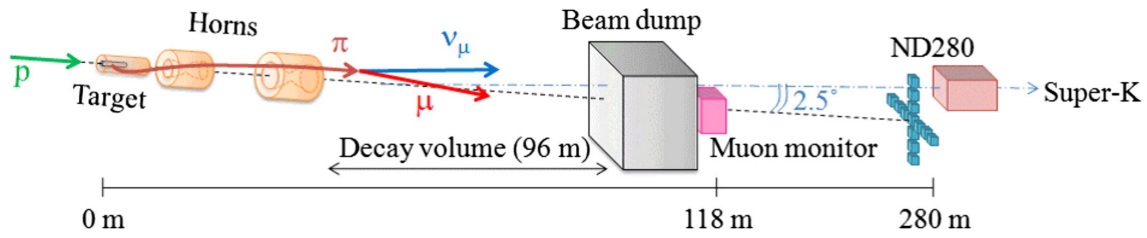
### 670 2.2.1 The Neutrino Beam

671 The neutrino beam used within the T2K experiment is described in [55, 106] and  
672 summarised below. The accelerating facility at J-PARC is composed of two sections; the  
673 primary and secondary beamlines. Figure 2.6 illustrates a schematic of the beamline,  
674 focusing mostly on the components of the secondary beamline. The primary beamline  
675 has three accelerators that progressively accelerate protons; a linear accelerator, a rapid-  
676 cycling synchrotron, and the main-ring (MR) synchrotron. Once fully accelerated by  
677 the MR, the protons have a kinetic energy of 30GeV. Eight bunches of these protons,  
678 separated by 500ns, are extracted per “spill” from the MR and directed towards a  
679 graphite target (A rod of length 91.4cm and diameter 2.6cm). Spills are extracted at  
680 0.5Hz with  $\sim 3 \times 10^{14}$  protons contained per spill.

681 The secondary beamline consists of three main components; the target station, the  
682 decay volume, and the beam dump. The target station is comprised of the target, beam  
683 monitors, and three magnetic focusing horns. The proton beam interacts with the  
684 graphite target to form a secondary beam of mostly pions and kaons. The secondary  
685 beam travels through a 96m long decay volume, generating neutrinos through the  
686 following decays [55],



(a) Primary and secondary beamline



(b) Secondary beamline

**Figure 2.6:** Top panel: Bird's eye view of the most relevant part of primary and secondary beamline used within the T2K experiment. The primary beamline is the main-ring proton synchrotron, kicker magnet, and graphite target. The secondary beamline consists of the three focusing horns, decay volume, and beam dump. Figure taken from [106]. Bottom panel: The side-view of the secondary beamline including the focusing horns, beam dump and neutrino detectors. Figure taken from [107].

$$\begin{array}{ll}
 \pi^+ \rightarrow \mu^+ + \nu_\mu & \pi^- \rightarrow \mu^- + \bar{\nu}_\mu \\
 K^+ \rightarrow \mu^+ + \nu_\mu & K^- \rightarrow \mu^- + \bar{\nu}_\mu \\
 \rightarrow \pi^0 + e^+ + \nu_e & \rightarrow \pi^0 + e^- + \bar{\nu}_e \\
 \rightarrow \pi^0 + \mu^+ + \nu_\mu & \rightarrow \pi^0 + \mu^- + \bar{\nu}_\mu \\
 K_L^0 \rightarrow \pi^- + e^+ + \nu_e & K_L^0 \rightarrow \pi^+ + e^- + \bar{\nu}_e \\
 \rightarrow \pi^- + \mu^+ + \nu_\mu & \rightarrow \pi^+ + \mu^- + \bar{\nu}_\mu \\
 \mu^+ \rightarrow e^+ + \bar{\nu}_\mu + \nu_e & \mu^- \rightarrow e^- + \nu_\mu + \bar{\nu}_e
 \end{array}$$

The electrically charged component of the secondary beam is focused towards the far detector by the three magnetic horns. These horns direct charged particles of a particular polarity towards SK whilst defocusing the oppositely charged particles. This allows a mostly neutrino or mostly antineutrino beam to be used within the experiment, denoted as “forward horn current (FHC)” or “reverse horn current (RHC)” respectively.

Figure 2.7 illustrates the different contributions to the FHC and RHC neutrino flux.

The low energy flux is dominated by the decay of pions whereas kaon decay becomes the dominant source of neutrinos for  $E_\nu > 3\text{GeV}$ . The “wrong-sign” component, which is the  $\bar{\nu}_\mu$  background in a  $\nu_\mu$  beam, and the intrinsic irreducible  $\nu_e$  background are predominantly due to muon decay for  $E_\nu < 2\text{GeV}$ . As the antineutrino cross-section is smaller than the neutrino cross-section, the wrong-sign component is more dominant in the RHC beam as compared to that in the FHC beam.

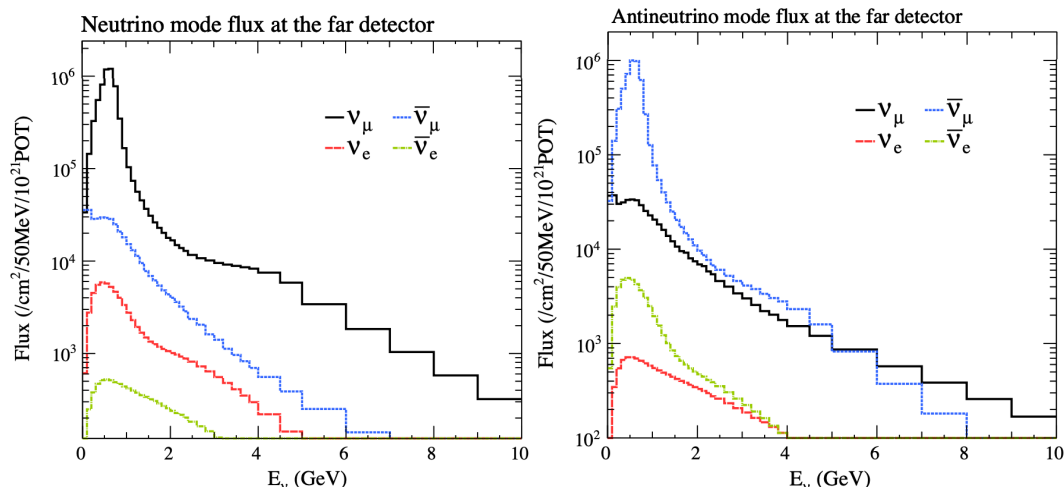


**Figure 2.7:** The Monte Carlo prediction of the energy spectrum for each flavour of neutrino ( $\nu_e$ ,  $\bar{\nu}_e$ ,  $\nu_\mu$  and  $\bar{\nu}_\mu$ ) in the neutrino dominated beam FHC mode (Left) and antineutrino dominated beam RHC mode (Right) expected at SK. Taken from [108].

The beam dump, situated at the end of the decay volume, stops all charged particles other than highly energetic muons ( $p_\mu > 5\text{GeV}$ ). The MuMon detector monitors the

<sup>703</sup> penetrating muons to determine the beam direction and intensity which is used to  
<sup>704</sup> constrain some of the beam flux systematics within the analysis [107, 109].

<sup>705</sup> The T2K experiment uses an off-axis beam to narrow the neutrino energy distribu-  
<sup>706</sup> tion. This was the first implementation of this technique in a long-baseline neutrino  
<sup>707</sup> oscillation experiment after its original proposal [110]. Pion decay,  $\pi \rightarrow \mu + \nu_\mu$ , is a  
<sup>708</sup> two-body decay. Consequently, the neutrino energy,  $E_\nu$ , can be determined based on  
<sup>709</sup> the pion energy,  $E_\pi$ , and the angle at which the neutrino is emitted,  $\theta$ ,

$$E_\nu = \frac{m_\pi^2 - m_\mu^2}{2(E_\pi - p_\pi \cos(\theta))}, \quad (2.5)$$

<sup>710</sup> where  $m_\pi$  and  $m_\mu$  are the mass of the pion and muon respectively. For a fixed  
<sup>711</sup> energy pion, the neutrino energy distribution is dependent upon the angle at which  
<sup>712</sup> the neutrinos are observed from the initial pion beam direction. For the 295km  
<sup>713</sup> baseline at T2K,  $E_\nu = 0.6\text{GeV}$  maximises the electron neutrino appearance probability,  
<sup>714</sup>  $P(\nu_\mu \rightarrow \nu_e)$ , whilst minimising the muon disappearance probability,  $P(\nu_\mu \rightarrow \nu_\mu)$ .  
<sup>715</sup> Figure 2.8 illustrates the neutrino energy distribution for a range of off-axis angles, as  
<sup>716</sup> well as the oscillation probabilities most relevant to T2K.

### <sup>717</sup> 2.2.2 The Near Detector at 280m

<sup>718</sup> Whilst all the near detectors are situated in the same “pit” located at 280m from the  
<sup>719</sup> beamline, the “ND280” detector is the off-axis detector which is situated at the same  
<sup>720</sup> off-axis angle as the Super-Kamiokande far detector. It has two primary functions;  
<sup>721</sup> firstly it measures the neutrino flux and secondly it counts the event rates of different  
<sup>722</sup> types of neutrino interactions. Both of these constrain the flux and cross-section

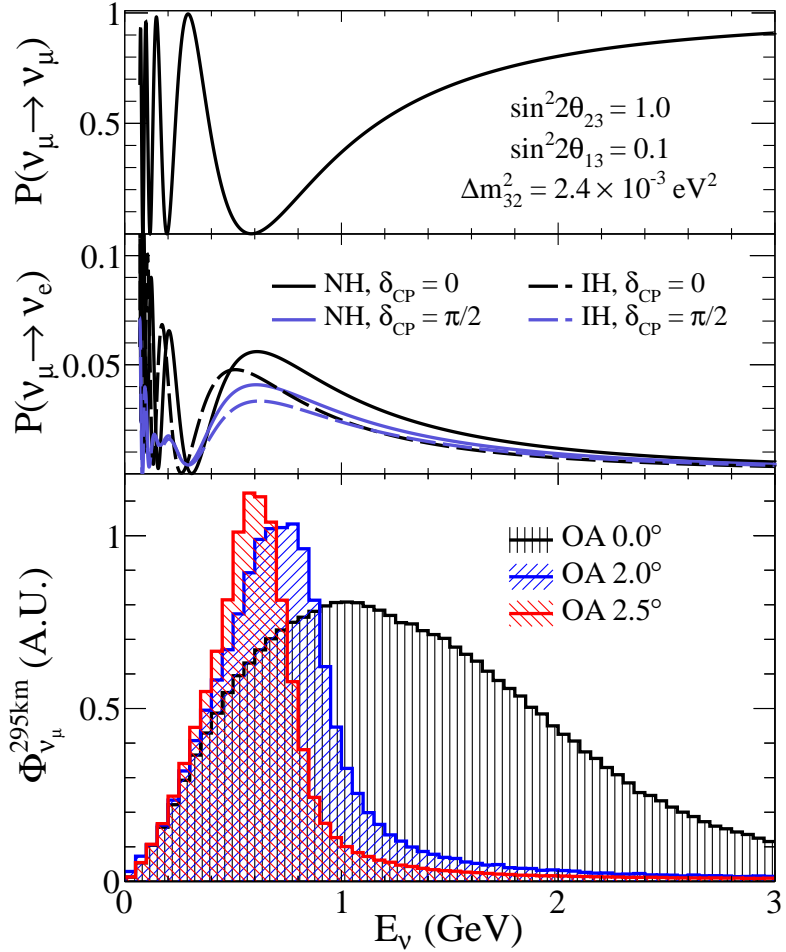


**Figure 2.8:** Top panel: T2K muon neutrino disappearance probability as a function of neutrino energy. Middle panel: T2K electron neutrino appearance probability as a function of neutrino energy. Bottom panel: The neutrino flux distribution for three different off-axis angles (Arbitrary units) as a function of neutrino energy.

systematics invoked within the model for a more accurate prediction of the expected event rate at the far detector.

As illustrated in Figure 2.9, the ND280 detector consists of several sub-detectors. The most important part of the detector for this analysis is the tracker region. This is comprised of two time projection chambers (TPCs) sandwiched between three fine grain detectors (FGDs). The FGDs contain both hydrocarbon plastics and water targets for neutrino interactions and provide track reconstruction near the interaction vertex. The emitted charged particles can then propagate into the TPCs which provide particle identification and momentum reconstruction. The FGDs and TPCs are

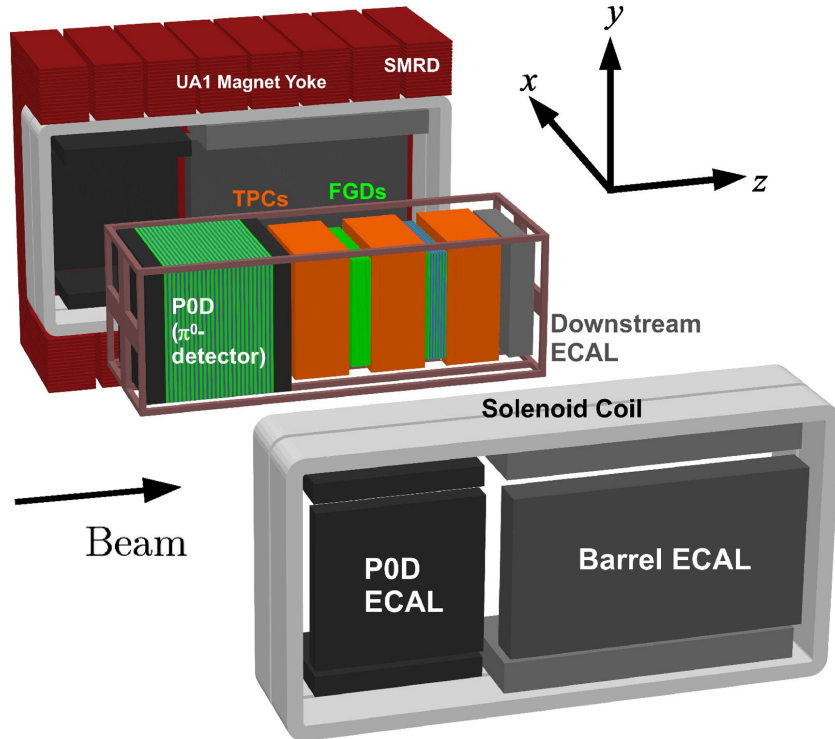


**Figure 2.9:** The components of the ND280 detector. The neutrino beam travels from left to right. Taken from [106].

732 further described in subsubsection 2.2.2.1 and subsubsection 2.2.2.2 respectively. The  
 733 electromagnetic calorimeter (ECAL) encapsulates the tracker region alongside the  $\pi^0$   
 734 detector (P0D). The ECAL measures the deposited energy from photons emitted from  
 735 interactions within the FGD. The P0D constrains the cross-section of neutral current  
 736 interactions which generate neutral pions, which is one of the largest backgrounds in  
 737 the electron neutrino appearance oscillation channel. The P0D and ECAL detectors  
 738 are detailed in subsubsection 2.2.2.3 and subsubsection 2.2.2.4 respectively. The entire  
 739 detector is located within a large yolk magnet which produces a 0.2T magnetic field.  
 740 This design of the magnet also includes a scintillating detector called the side muon  
 741 range detector (SMRD) which is used to track high-angle muons as well as acting as a  
 742 cosmic veto. The SMRD is described in subsubsection 2.2.2.5.

<sup>743</sup> **2.2.2.1 Fine Grained Detectors**

<sup>744</sup> The T2K tracker region is comprised of two fine grained detectors (FGD) and three  
<sup>745</sup> Time Projection Chambers (TPC). A detailed description of the FGD design, construc-  
<sup>746</sup> tion, and assembly is found in [111] and summarised below. The FGDs are the primary  
<sup>747</sup> target for neutrino interactions with a mass of 1.1 tonnes per FGD. Alongside this,  
<sup>748</sup> the FGDs are designed to be able to track short-range particles which do not exit the  
<sup>749</sup> FGD. Typically, short-range particles are low momentum and are observed as tracks  
<sup>750</sup> that deposit a large amount of energy per unit length. This means the FGD needs  
<sup>751</sup> good granularity to resolve these particles. The FGDs have the best timing resolution  
<sup>752</sup> ( $\sim 3\text{ns}$ ) of any of the sub-detectors of the ND280 detector. As such, the FGDs are  
<sup>753</sup> used for time of flight measurements to determine forward going positively charged  
<sup>754</sup> particles from backward going negatively charged particles. Finally, any tracks which  
<sup>755</sup> pass through multiple sub-detectors are required to be track matched to the FGD.

<sup>756</sup> Both FDGs are made from square scintillator planes of side length 186cm and width  
<sup>757</sup> 2.02cm. Each plane consists of two layers of 192 scintillator bars in an XY orientation.  
<sup>758</sup> A wave-length shift fiber is threaded through the center of each bar and is read out by  
<sup>759</sup> a multi-photon pixel counter (MPPC). FGD1 is the most upstream of the two FGDs  
<sup>760</sup> and contains 15 planes of carbon plastic scintillator which is a common target in  
<sup>761</sup> external neutrino scattering data. As the far detector is a pure water target, 7 of the 15  
<sup>762</sup> scintillator planes in FGD2 have been replaced with a hybrid water-scintillator target.  
<sup>763</sup> Due to the complexity of the nucleus, nuclear effects can not be extrapolated between  
<sup>764</sup> different nuclei. Therefore having the ability to take data on one target which is the  
<sup>765</sup> same as external data and another target which is the same as the far detector target is  
<sup>766</sup> beneficial for reliable model parameter estimates.

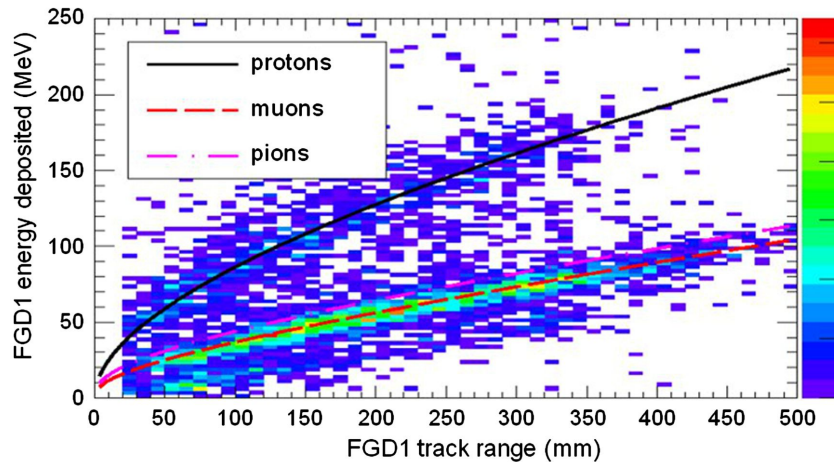


**Figure 2.10:** Comparison of data to Monte Carlo prediction of integrated deposited energy as a function of track length for particles that stopped in FGD1. Taken from [111].

767     The integrated deposited energy is used for particle identification. The FGD  
 768     can distinguish protons from other charged particles by comparing the integrated  
 769     deposited energy from data to Monte Carlo prediction as seen in Figure 2.10.

#### 770     2.2.2.2 Time Projection Chambers

771     The majority of particle identification and momentum measurements within ND280  
 772     are provided by three Time Projection Chambers (TPCs) [112]. The TPCs are located  
 773     on either side of the FGDs. They are located inside of the magnetic field meaning the  
 774     momentum of a charged particle can be determined from the bending of the track.

775     Each TPC module consists of two gas-tight boxes, as shown in Figure 2.11, which  
 776     are made of non-magnetic material. The outer box is filled with CO<sub>2</sub> which acts as  
 777     an electrical insulator between the inner box and the ground. The inner box forms  
 778     the field cage which produces a uniform electric drift field of  $\sim 275\text{V/cm}$  and an  
 779     argon gas mixture. Charged particles moving through this gas mixture ionize the gas  
 780     mixture. The ionised charge is drifted towards micromega detectors which measure  
 781     the ionization charge. The time and position information in the readout allows a  
 782     three-dimensional image of the neutrino interaction.

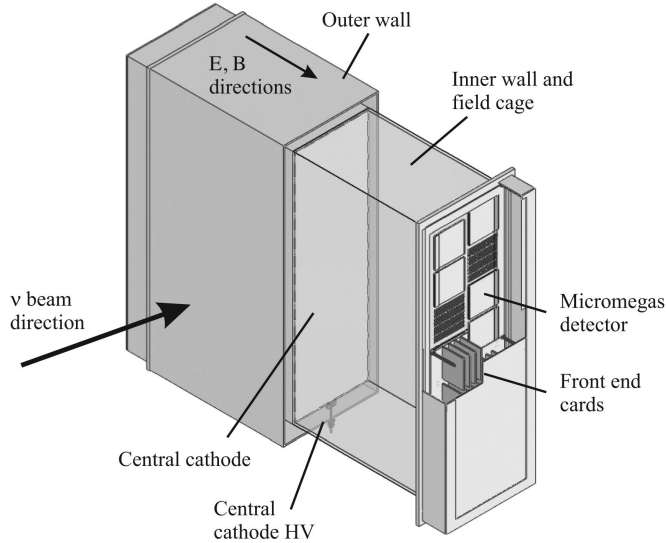


**Figure 2.11:** Schematic design of a Time Projection Chamber detector. Taken from [112].

The particle identification of tracks that pass through the TPCs is performed using

dE/dx measurements. Figure 2.12 illustrates the data to Monte Carlo distributions of the energy lost by a charged particle passing through the TPC as a function of the reconstructed particle momentum. The resolution is  $7.8 \pm 0.2\%$  meaning that electrons and muons can be distinguished. This allows reliable measurements of the intrinsic  $\nu_e$  component of the beam.

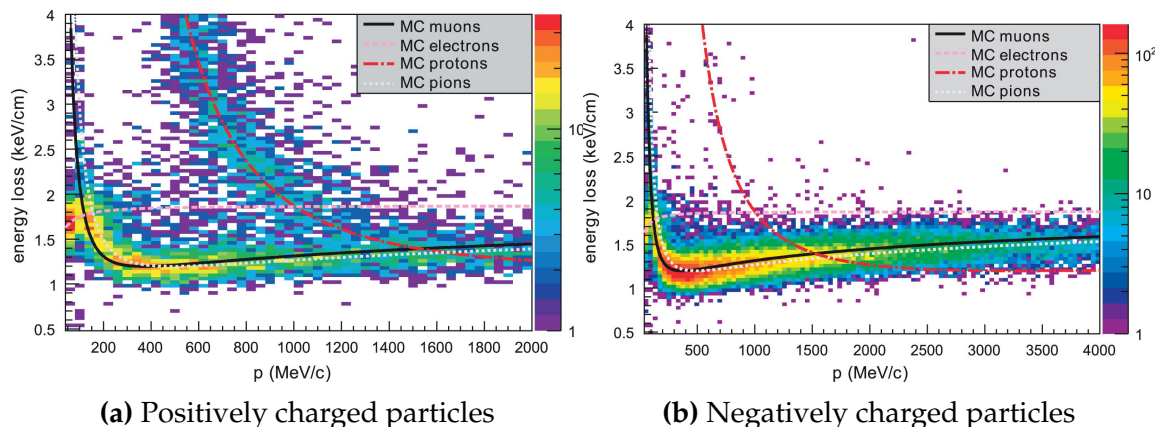


**Figure 2.12:** The distribution of energy loss as a function of reconstructed momentum for charged particles passing through the TPC, comparing data to Monte Carlo prediction. Taken from [112].

<sup>789</sup> **2.2.2.3  $\pi^0$  Detector**

<sup>790</sup> If one of the  $\gamma$ -rays from a  $\pi^0 \rightarrow 2\gamma$  decay is missed at the far detector, the reconstruc-  
<sup>791</sup> tion will determine that event to be electron-like. This is one of the main backgrounds  
<sup>792</sup> hindering the electron neutrino appearance searches. Therefore, the  $\pi^0$  detector (P0D)  
<sup>793</sup> measures the cross-section of the neutral current induced neutral pion production on  
<sup>794</sup> a water target.

<sup>795</sup> The P0D is a cube of approximately 2.5m length. The P0D consists of layers of  
<sup>796</sup> scintillating bars, brass and lead sheets, and water bags as illustrated in Figure 2.13.  
<sup>797</sup> Two electromagnetic calorimeters are positioned at the most upstream and most  
<sup>798</sup> downstream position in the sub-detector and the water target is situated in between  
<sup>799</sup> them. The scintillator layers are built from two triangular bars orientated in opposite  
<sup>800</sup> directions to form a rectangular layer. Each triangular scintillator bar is threaded with  
<sup>801</sup> optical fiber which is read out by MPPCs. The high-Z brass and lead regions produce  
<sup>802</sup> electron showers from the photons emitted in  $\pi^0$  decay.

<sup>803</sup> The sub-detector can generate measurements of NC1 $\pi^0$  cross-sections on a water  
<sup>804</sup> target by measuring the event rate both with and without the water target, with the  
<sup>805</sup> cross-section on a water target being determined as the difference. The total active  
<sup>806</sup> mass is 16.1 tonnes when filled with water and 13.3 tonnes when empty.

<sup>807</sup> **2.2.2.4 Electromagnetic Calorimeter**

<sup>808</sup> The electromagnetic calorimeter [114] (ECal) encapsulates the P0D and tracking sub-  
<sup>809</sup> detectors. Its primary purpose is to aid  $\pi^0$  reconstruction from any interaction in  
<sup>810</sup> the tracker. To do this, it measures the energy and direction of photon showers from  
<sup>811</sup>  $\pi^0 \rightarrow 2\gamma$  decay. It can also distinguish pion and muon tracks depending on the shape  
<sup>812</sup> of the photon shower deposited.

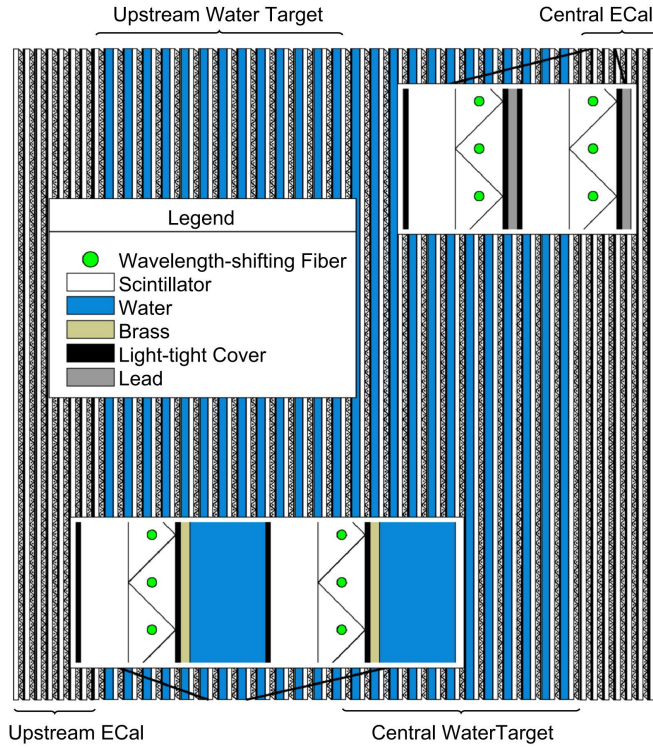


**Figure 2.13:** A schematic of the P0D side-view. Taken from [113].

The ECal is comprised of three sections; the P0D ECal which surrounds the P0D, the barrel ECal which encompasses the tracking region, and the downstream ECal which is situated downstream of the tracker region. The barrel and downstream ECals are tracking calorimeters that focus on electromagnetic showers from high-angle particles emitted from the tracking sub-detectors. Particularly in the TPC, high-angle tracks (those which travel perpendicularly to the beam-axis) can travel along a single scintillator bar resulting in very few hits. The width of the barrel and downstream ECal corresponds to  $\sim 11$  electron radiation lengths to ensure  $\sim 50\%$  of the energy of the  $\pi^0$  is contained. As the P0D has its own calorimetry which reconstructs showers, the P0D ECal determines the energy which escapes the P0D.

Each ECal is constructed of multiple layers of scintillating bars sandwiched between lead sheets. The scintillating bars are threaded with optical fiber and read out by MPPCs. Each sequential layer of the scintillator is orientated perpendicular to the previous which allows a two-dimensional readout, which when temporal information

<sup>827</sup> is included results in three-dimension event displays. The target mass of the P0D ECal,  
<sup>828</sup> barrel ECal, and downstream ECal are 1.50, 4.80 and 6.62 tonnes respectively.

<sup>829</sup> **2.2.2.5 Side Muon Range Detector**

<sup>830</sup> As illustrated in Figure 2.9, the ECal, FGDs, P0D, and TPCs are enclosed within the  
<sup>831</sup> UA1 magnet. Originally designed for the NOMAD [115] experiment and reconditioned  
<sup>832</sup> for use in the T2K experiment [116], the UA1 magnet provides a uniform horizontal  
<sup>833</sup> magnetic field of  $0.2 \pm 2 \times 10^{-4}$ T.

<sup>834</sup> Built into the UA1 magnet, the side muon range detector (SMRD) [117] monitors  
<sup>835</sup> high-energy muons which leave the tracking region and permeate through the ECal.  
<sup>836</sup> It additionally acts as a cosmic muon veto and trigger.

<sup>837</sup> **2.2.3 The Interactive Neutrino GRID**

<sup>838</sup> The Interactive Neutrino GRID (INGRID) detector is situated within the same “pit” as  
<sup>839</sup> the other near detectors. It is aligned with the beam in the “on-axis” position and mea-  
<sup>840</sup> sures the beam direction, spread, and intensity. The detector was originally designed  
<sup>841</sup> with 16 identical modules [106] (two modules have since been decommissioned) and a  
<sup>842</sup> “proton” module. The design of the detector is cross-shaped with length and height  
<sup>843</sup> 10m × 10m as illustrated in Figure 2.14.

<sup>844</sup> Each module is composed of iron sheets interlaced with eleven tracking scintillator  
<sup>845</sup> planes for a total target mass of 7.1 tonnes per module. The scintillator design is an X-Y  
<sup>846</sup> pattern of 24 bars in both orientations, where each bar contains wave-length shifting  
<sup>847</sup> fibers which are connected to multi-pixel photon counters (MPPCs). The MPPCs  
<sup>848</sup> convert detected photons into electrical signals via photodiodes. This is then read  
<sup>849</sup> out by Trip-T front-end electronics [118] and passed to the readout merging modules

850 along with timing information from the clock module. Each module is encapsulated  
 851 inside veto planes to aid the rejection of charged particles entering the module.

852 The proton module is different from the other modules in that it consists of entirely  
 853 scintillator planes with no iron target. The scintillator bars are also smaller than those  
 854 used in the other modules to increase the granularity of the detector and improve  
 855 tracking capabilities. The module sits in the center of the beamline and is designed to  
 856 give precise measurements of quasi-elastic charged current interactions to evaluate  
 857 the performance of the Monte Carlo simulation of the beamline.

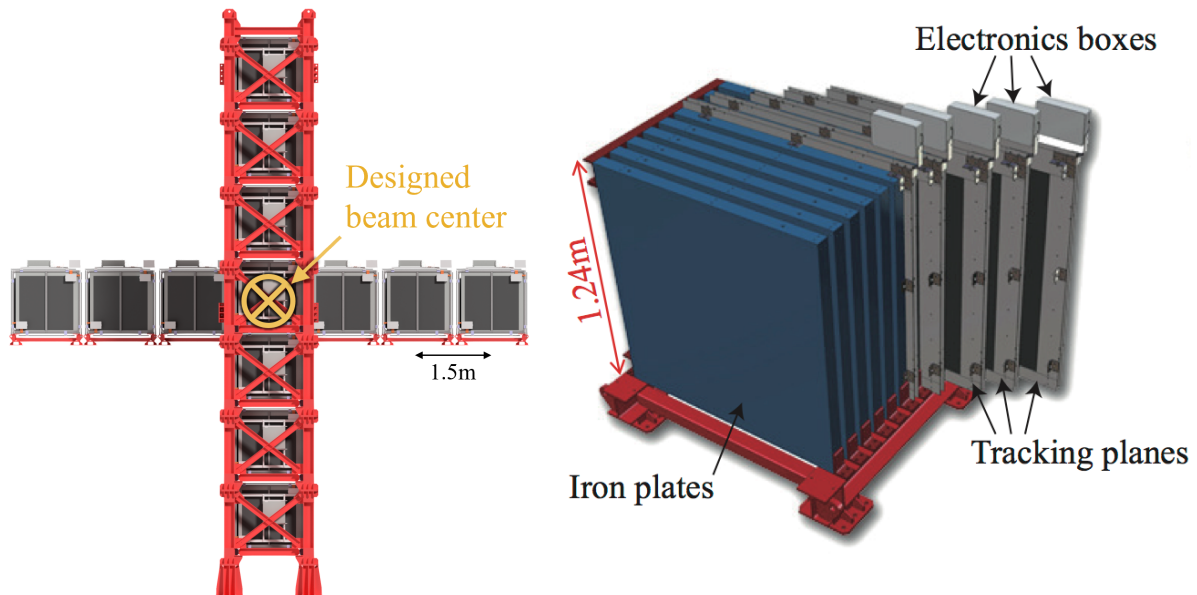


**Figure 2.14:** Left panel: The Interactive Neutrino GRID on-axis Detector. 14 modules are arranged in a cross-shape configuration, with the center modules being directly aligned with the on-axis beam. Right panel: The layout of a single module of the INGRID detector. Both figures are recreated from [106].

858 The INGRID detector can measure the beam direction to an uncertainty of 0.4mrad  
 859 and the beam center within a resolution of 10cm [106]. The beam direction in both the  
 860 vertical and horizontal directions is discussed in [119] and it is found to be in good  
 861 agreement with the MUMON monitor described in subsection 2.2.1.

862 **Chapter 3**

863 **Bayesian Statistics and Markov Chain  
Monte Carlo Techniques**

865 The analysis throughout this thesis is based upon a Bayesian oscillation analysis. To  
866 extract the oscillation parameters, a Markov Chain Monte Carlo (MCMC) method is  
867 used. This chapter explains the theory of how parameter estimates can be determined  
868 using this technique and condenses the material found in the literature [120–123].

869 The oscillation parameter determination presented within this thesis is built upon a  
870 simultaneous fit to the near detector, far detector beam, and atmospheric neutrino data.  
871 In total, there are four oscillation parameters of interest ( $\sin^2(\theta_{23})$  ,  $\sin^2(\theta_{13})$  ,  $\Delta m_{23}^2$  ,  
872 and  $\delta_{CP}$  ), two oscillation parameters to which this study will not be sensitive ( $\sin^2(\theta_{12})$   
873 ,  $\Delta m_{12}^2$  ) and many nuisance parameters that control the systematic uncertainty models  
874 invoked within this study. The systematic uncertainties can be grouped into categories  
875 depending on how they are defined; 574 bin-normalisations due to the near detector  
876 response, 45 bin-normalisations to describe the far detector response to neutrino beam  
877 events, 27 parameters to describe the detector response to atmospheric neutrino events,  
878 100 to model the bin-normalisation due to beam flux uncertainties, 18 which model the  
879 atmospheric flux uncertainties, and 87 to describe the correlated cross-section model.  
880 An alternative parameterisation, where the far detector response is correlated between  
881 the beam and atmospheric samples, replaces the bin-normalisation parameters with  
882 224 shift and smear systematics. Section [DB: Link to Systematics Chapter](#) describes  
883 the systematic model in more depth.

884 The MCMC technique generates a multi-dimensional probability distribution across  
 885 all of the model parameters used in the fit. To determine the parameter estimate of a  
 886 single parameter, this multi-dimensional object is integrated over all other parameters.  
 887 This process is called Marginalisation and is further described in subsection 3.3.1.  
 888 Monte Carlo techniques approximate the probability distribution of each parameter  
 889 within the limit of generating infinite samples. As ever, generating a large number of  
 890 samples is time and resource-dependent. Therefore, an MCMC technique is utilised  
 891 within this analysis to reduce the required number of steps to sufficiently sample the  
 892 parameter space. This technique is described in further detail in subsection 3.2.1.

893 **3.1 Bayesian Statistics**

894 According to Bayesian Inference, observables and parameters of a statistical model are  
 895 treated on an equal footing. To estimate model parameters  $\vec{\theta}$  from some data  $D$ , one  
 896 needs to define the joint probability distribution  $P(D|\vec{\theta})$  which can be described as the  
 897 prior distribution for model parameters  $P(\vec{\theta})$  and the likelihood of the data given the  
 898 model parameters  $P(D|\vec{\theta})$ ,

$$P(D, \vec{\theta}) = P(D|\vec{\theta})P(\vec{\theta}). \quad (3.1)$$

899 The prior distribution,  $P(\vec{\theta})$ , describes all previous knowledge about the parameters  
 900 within the model. For example, if the risk of developing health problems is known  
 901 to increase with age, the prior distribution would describe the increase. For the  
 902 purpose of this analysis, the prior distribution is typically the best-fit values taken  
 903 from external data measurements with a Gaussian uncertainty. The prior distribution

904 can also contain correlations between model parameters. In an analysis using Monte  
 905 Carlo techniques, the likelihood of measuring some data assuming some set of model  
 906 parameters is calculated by comparing the Monte Carlo prediction generated at that  
 907 particular set of model parameters to the data.

908 It is parameter estimation that is important for this analysis and as such, we apply  
 909 Bayes' theorem [124]. To calculate the probability for each parameter to have a certain  
 910 value given the observed data  $P(\vec{\theta}|D)$ , known as the posterior distribution (often  
 911 termed the posterior). This can be expressed as

$$P(\vec{\theta}|D) = \frac{P(D|\vec{\theta})P(\vec{\theta})}{\int P(D|\vec{\theta})P(\vec{\theta})d\vec{\theta}}. \quad (3.2)$$

912 The denominator in Equation 3.2 is the integral of the joint probability distribution  
 913 over all values of all parameters used within the fit. For brevity, we say that the  
 914 posterior distribution is

$$P(\vec{\theta}|D)\alpha P(D|\vec{\theta})P(\vec{\theta}). \quad (3.3)$$

915 In subsection 3.3.1, we see that for the cases used within this analysis, it is reason-  
 916 able to know the posterior to some normalisation constant.

## 917 3.2 Monte Carlo Simulation

918 Monte Carlo techniques are used to numerically solve a complex problem that does  
 919 not necessarily have an analytical solution. These techniques rely on building a large

ensemble of samples from an unknown distribution and then using the ensemble to approximate the properties of the distribution.

An example that uses Monte Carlo techniques is to calculate the area underneath a curve. For example, take the problem of calculating the area under a straight line with gradient  $M = 0.4$  and intercept  $C = 1.0$ . Analytically, one can calculate the area under the line is equal to 30 units for  $0 \leq x \leq 10$ . Using Monte Carlo techniques, one can calculate the area under this line by throwing many random values for the  $x$  and  $y$  components of each sample and then calculating whether that point falls below the line. The area can then be calculated by the ratio of points below the line to the total number of samples thrown multiplied by the total area in which samples were scattered. The study is shown in Figure 3.1 highlights this technique and finds the area under the curve to be 29.9 compared to an analytical solution of 30.0. The deviation of the numerical to analytical solution can be attributed to the number of samples used in the study. The accuracy of the approximation in which the properties of the Monte Carlo samples replicate those of the desired distribution is dependent on the number of samples used. Replicating this study with a differing number of Monte Carlo samples used in each study (As shown in Figure 3.2) highlights how the Monte Carlo techniques are only accurate within the limit of a high number of samples.

Whilst the above example has an analytical solution, these techniques are just as applicable to complex solutions. Clearly, any numerical solution is only as useful as its efficiency. As discussed, the accuracy of the Monte Carlo technique is dependent upon the number of samples generated to approximate the properties of the distribution. Furthermore, if the positions at which the samples are evaluated are not 'cleverly' picked, the efficiency of the Monte Carlo technique significantly drops. Given the example in Figure 3.1, if the region in which the samples are scattered significantly extends passed the region of interest, many calculations will be calculated but do

not add to the ability of the Monte Carlo technique to achieve the correct result. For instance, any sample evaluated at a  $y \geq 5$  could be removed without affecting the final result. This does bring in an aspect of the ‘chicken and egg’ problem in that to achieve efficient sampling, one needs to know the distribution beforehand.

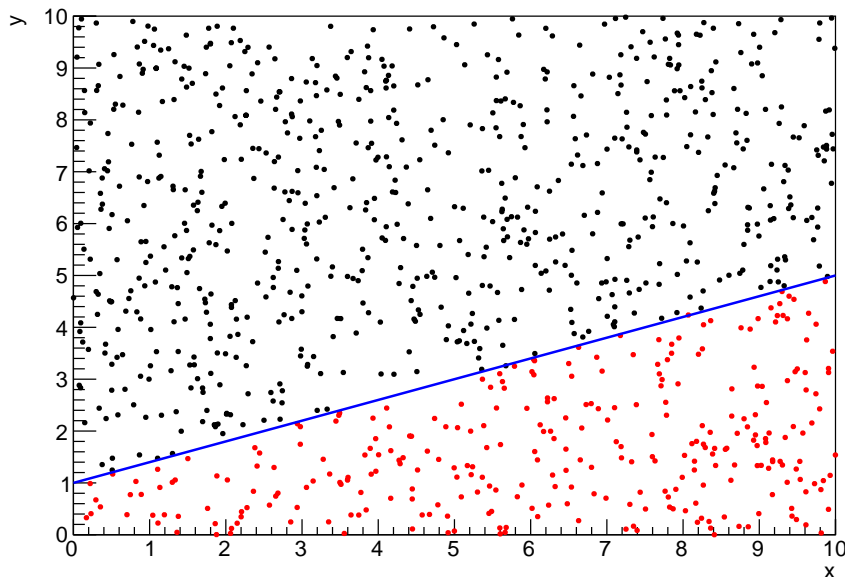


**Figure 3.1:** Example of using Monte Carlo techniques to find the area under the blue line. The gradient and intercept of the line are 0.4 and 1.0 respectively. The area found to be under the curve using one thousand samples is 29.9 units.

### 3.2.1 Markov Chain Monte Carlo

This analysis utilises a multi-dimensional probability distribution, with some dimensions being significantly more constrained than others. This could be from prior knowledge of parameter distributions from external data or un-physical regions in which parameters can not exist. Consequently, the Monte Carlo techniques used need to be as efficient as possible. For this analysis, the Markov Chain Monte Carlo (MCMC) technique is chosen. An MCMC technique is a Monte Carlo technique that uses a Markov chain to select which points at which to sample the parameter distribution.

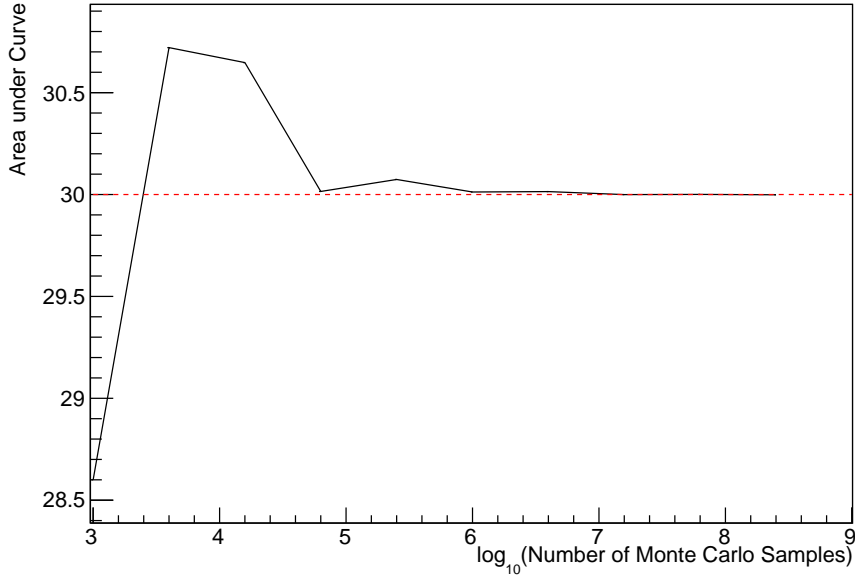


**Figure 3.2:** The area under a line of gradient 0.4 and intercept 1.0 for the range  $0 \leq x \leq 10$  as calculated using Monte Carlo techniques as a function of the number of samples used in each repetition. The analytical solution to the area is 30 units as given by the red line.

958 This technique performs a semi-random stochastic walk through the allowable pa-  
 959 rameter space. This builds a posterior distribution which has the property that the  
 960 density of sampled points is proportional to the probability density of that parame-  
 961 ter. This does mean that the samples produced by this technique are not statistically  
 962 independent but they will cover the space of the distribution.

963 A Markov chain functions by selecting the position of step  $\vec{x}_{i+1}$  based on the  
 964 position of  $\vec{x}_i$ . The space in which the Markov chain selects samples is dependent  
 965 upon the total number of parameters utilised within the fit, where a discrete point in  
 966 this space is described by the N-dimensional space  $\vec{x}$ . In a perfectly operating Markov  
 967 chain, the position of the next step depends solely on the previous step and not on the  
 968 further history of the chain ( $\vec{x}_0, \vec{x}_1$ , etc.). However, in solving the multi-dimensionality  
 969 of the fit used within this analysis, each step becomes correlated with several of  
 970 the steps preceding itself. This behaviour is further explained in subsection 3.2.3.  
 971 Providing the MCMC chain is well optimised, it will begin to converge towards a

unique stationary distribution. The period between the chain's initial starting point and the convergence to the unique stationary distribution is colloquially known as the burn-in period. This is discussed further in subsection 3.2.3. Once the chain reaches the stationary distribution, all points sampled after that point will look like samples from that distribution.

Further details of the theories underpinning MCMC techniques are discussed in [121] but can be summarised by the requirement that the chain satisfies the three 'regularity conditions':

- Irreducibility: From every position in the parameter space  $\vec{x}$ , there must exist a non-zero probability for every other position in the parameter space to be reached.
- Recurrence: Once the chain arrives at the stationary distribution, every step following from that position must be samples from the same stationary distribution.
- Aperiodicity: The chain must not repeat the same sequence of steps at any point throughout the sampling period.

The output of the chain after burn-in (ie. the sampled points after the chain has reached the stationary distribution) can be used to approximate the posterior distribution and model parameters  $\vec{\theta}$ . To achieve the requirement that the unique stationary distribution found by the chain be the posterior distribution, one can use the Metropolis-Hastings algorithm. This guides the stochastic process depending on the likelihood of the current proposed step compared to that of the previous step. Implementation and other details of this technique are discussed in subsection 3.2.2.

### <sup>993</sup> 3.2.2 Metropolis-Hastings Algorithm

<sup>994</sup> As a requirement for MCMCs, the Markov chain implemented in this technique must  
<sup>995</sup> have a unique stationary distribution that is equivalent to the posterior distribution.  
<sup>996</sup> To ensure this requirement and that the regularity conditions are met, this analysis  
<sup>997</sup> utilises the Metropolis-Hastings (MH) algorithm [125,126]. For the  $i^{th}$  step in the chain,  
<sup>998</sup> the MH algorithm determines the position in the parameter space to which the chain  
<sup>999</sup> moves to based on the current step,  $\vec{x}_i$ , and the proposed step,  $\vec{y}_{i+1}$ . The proposed step  
<sup>1000</sup> is randomly selected from some proposal function  $f(\vec{x}_{i+1}|\vec{x}_i)$ , which depends solely  
<sup>1001</sup> on the current step (ie. not the further history of the chain). The next step in the chain  
<sup>1002</sup>  $\vec{x}_{i+1}$  can be either the current step or the proposed step determined by whether the  
<sup>1003</sup> proposed step is accepted or rejected. To decide if the proposed step is selected, the  
<sup>1004</sup> acceptance probability,  $\alpha(\vec{x}_i, \vec{y}_i)$ , is calculated as

$$\alpha(\vec{x}_i, \vec{y}_{i+1}) = \min\left(1, \frac{P(\vec{y}_{i+1}|D)f(\vec{x}_i|\vec{y}_{i+1})}{P(\vec{x}_i|D)f(\vec{y}_{i+1}|\vec{x}_i)}\right). \quad (3.4)$$

<sup>1005</sup> Where  $P(\vec{y}_{i+1}|D)$  is the posterior distribution as introduced in section 3.1. To  
<sup>1006</sup> simplify this calculation, the proposal function is required to be symmetric such that  
<sup>1007</sup>  $f(\vec{x}_i|\vec{y}_{i+1}) = f(\vec{y}_{i+1}|\vec{x}_i)$ . In practice, a multi-variate Gaussian distribution is used to  
<sup>1008</sup> throw parameter proposals from. This reduces Equation 3.4 to

$$\alpha(\vec{x}_i, \vec{y}_{i+1}) = \min\left(1, \frac{P(\vec{y}_{i+1}|D)}{P(\vec{x}_i|D)}\right). \quad (3.5)$$

1009 After calculating this quantity, a random number,  $\beta$ , is generated uniformly be-  
1010 tween 0 and 1. If  $\beta \leq \alpha(\vec{x}_i, \vec{y}_{i+1})$ , the proposed step is accepted. Otherwise, the chain  
1011 sets the next step equal to the current step and this procedure is repeated. This can be  
1012 interpreted as if the posterior probability of the proposed step is greater than that of  
1013 the current step, ( $P(\vec{y}_{i+1}|D) \geq P(\vec{x}_i|D)$ ), the proposed step will always be accepted.  
1014 If the opposite is true, ( $P(\vec{y}_{i+1}|D) \leq P(\vec{x}_i|D)$ ), the proposed step will be accepted  
1015 with probability  $P(\vec{x}_i|D)/P(\vec{y}_{i+1}|D)$ . This ensures that the Markov chain does not get  
1016 trapped in any local minima in the potentially non-Gaussian posterior distribution.  
1017 The outcome of this technique is that the density of steps taken in a discrete region is  
1018 directly proportional to the probability density in that region.

### 1019 3.2.3 MCMC Optimisation

1020 As discussed in subsection 3.2.2, the proposal function invoked within the MH algo-  
1021 rithm can take any form and the chain will still converge to the stationary distribution.  
1022 As discussed in [DB: Link to Analysis Strategy Section](#), this analysis performs the  
1023 Monte Carlo reweighting on an event-by-event basis. This requires significant com-  
1024 putational resources to perform a parameter fit. Therefore, the number of steps taken  
1025 before the unique stationary distribution is found should be minimised as only steps  
1026 after convergence add information to the fit. Furthermore, the chain should entirely  
1027 cover the allowable parameter space to ensure that all values have been considered.  
1028 Tuning the distance that the proposal function jumps between steps on a parameter-  
1029 by-parameter basis can both minimise the length of the burn-in period and ensure that  
1030 the correlation between step  $\vec{x}_i$  and  $\vec{x}_j$  is sufficiently small.

1031 The effect of changing the width of the proposal function is highlighted in Figure 3.3.  
1032 Three scenarios, each with the same underlying stationary distribution (A Gaussian of  
1033 width 1.0 and mean 0.), are presented. The only difference between the three scenarios

is the width of the proposal function, colloquially known as the ‘step size  $\sigma$ ’. Each scenario starts at an initial parameter value of 10.0 which would be considered an extreme variation. For the case where  $\sigma = 0.1$ , it is clear to see that the chain takes a long time to reach the expected region of the parameter. This indicates that this chain would have a large burn-in period and does not converge to the stationary distribution until step  $\sim 500$ . Furthermore, whilst the chain does move towards the expected region, each step is significantly correlated with the previous. Considering the case where  $\sigma = 5.0$ , the chain approaches the expected parameter region almost instantly meaning that the burn-in period is not significant. However, there are clearly large regions of steps where the chain does not move. This is likely due to the chain proposing steps in the tails of the distribution which have a low probability of being accepted. Consequently, this chain would take a significant number of steps to fully span the allowable parameter region. For the final scenario, where  $\sigma = 0.5$ , you can see a relatively small burn-in period of approximately 100 steps. Once the chain reaches the stationary distribution, it moves throughout the expected region of parameter values many times, sufficiently sampling the full parameter region. This example is a single parameter varying across a continuous distribution and does not fully reflect the difficulties in the many-hundred multi-variate parameter distribution used within this analysis. However, it does give a conceptual idea of the importance of selecting the proposal function and associated step size.

As discussed, step size tuning directly correlates to the average step acceptance rate. If the step size is too small, many steps will be accepted but the chain moves slowly. If the opposite is true, many steps will be rejected as the chain proposes steps in the tails of the distribution. Discussion in [127] suggests that the ‘ideal’ acceptance rate of a high dimension MCMC chain should be approximately  $\sim 25\%$ . An “ideal” step size [127] of

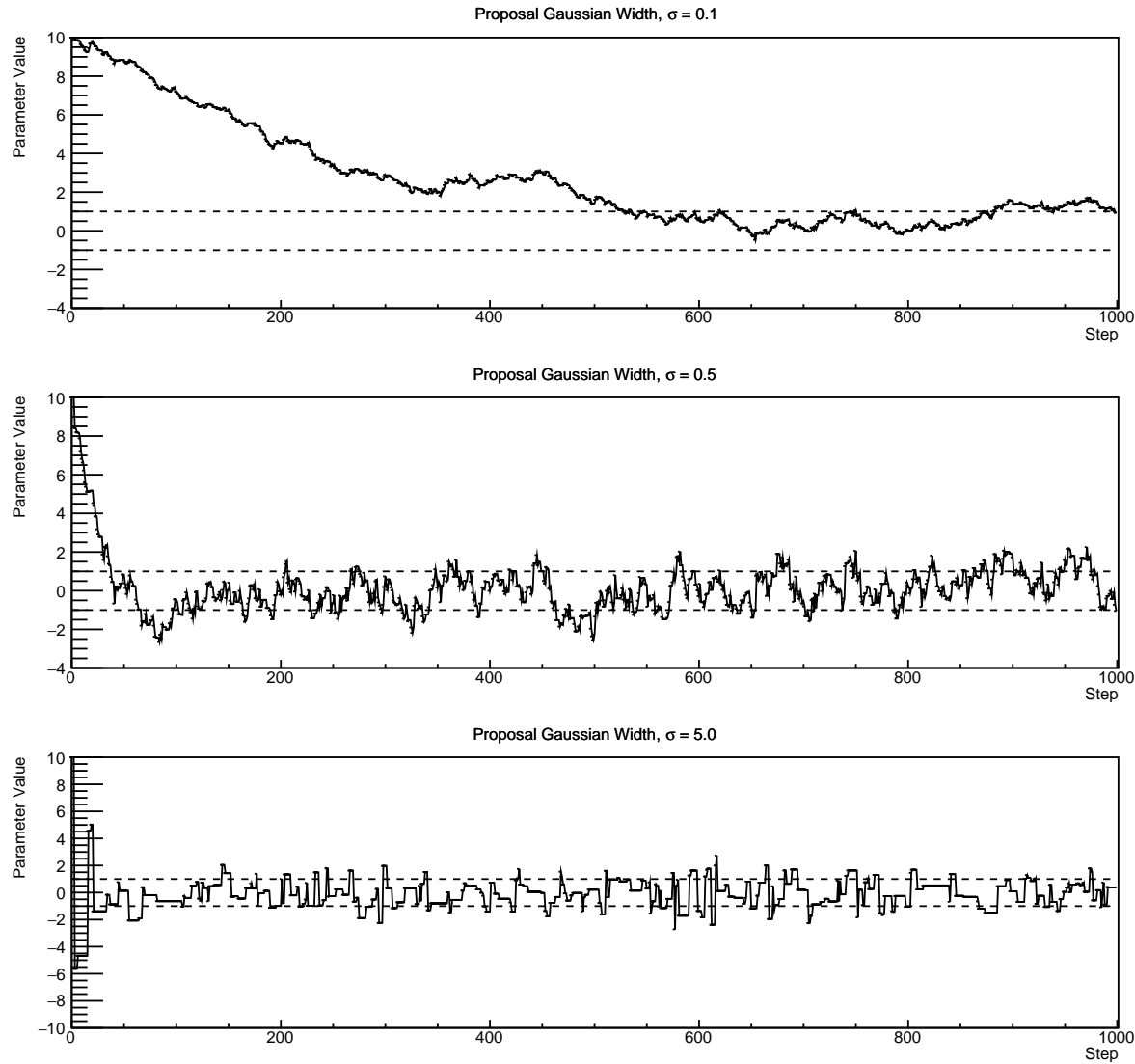


**Figure 3.3:** Three MCMC chains, each with a stationary distribution equal to a Gaussian centered at 0 and width 1 (As indicated by the black dotted lines). All of the chains use a Gaussian proposal function but have different widths (or ‘step size  $\sigma$ ’). The top panel has  $\sigma = 0.1$ , middle panel has  $\sigma = 0.5$  and the bottom panel has  $\sigma = 5.0$ .

$$\sigma = \frac{2.4}{N_p}, \quad (3.6)$$

where  $N_p$  is the number of parameters included in the MCMC fit. However, the complex correlations between systematics mean that some parameters have to be hand

1062 tuned and many efforts have been taken to select a set of parameter-by-parameter step  
1063 sizes to approximately reach the ideal acceptance rate.

1064 Figure 3.3 highlights the likelihood as calculated by the fit in [DB: Link to AsimovA](#)  
1065 [Sensitivity Section](#) as a function of the number of steps in each chain. In practice,  
1066 many independent MCMC chains are run simultaneously to parallelise the task of  
1067 performing the fit. This figure overlays the distribution found in each chain. As seen,  
1068 the likelihood decreases from its initial value and converges towards a stationary  
1069 distribution after  $\sim 1 \times 10^5$  steps. Each fit (whether it be different asimov fits or data  
1070 fit) will have a different set of preferred parameter values which results in a different  
1071 stationary distribution. For each fit presented in this thesis, a burn-in period of  $1 \times 10^5$   
1072 steps was found to be sufficient.

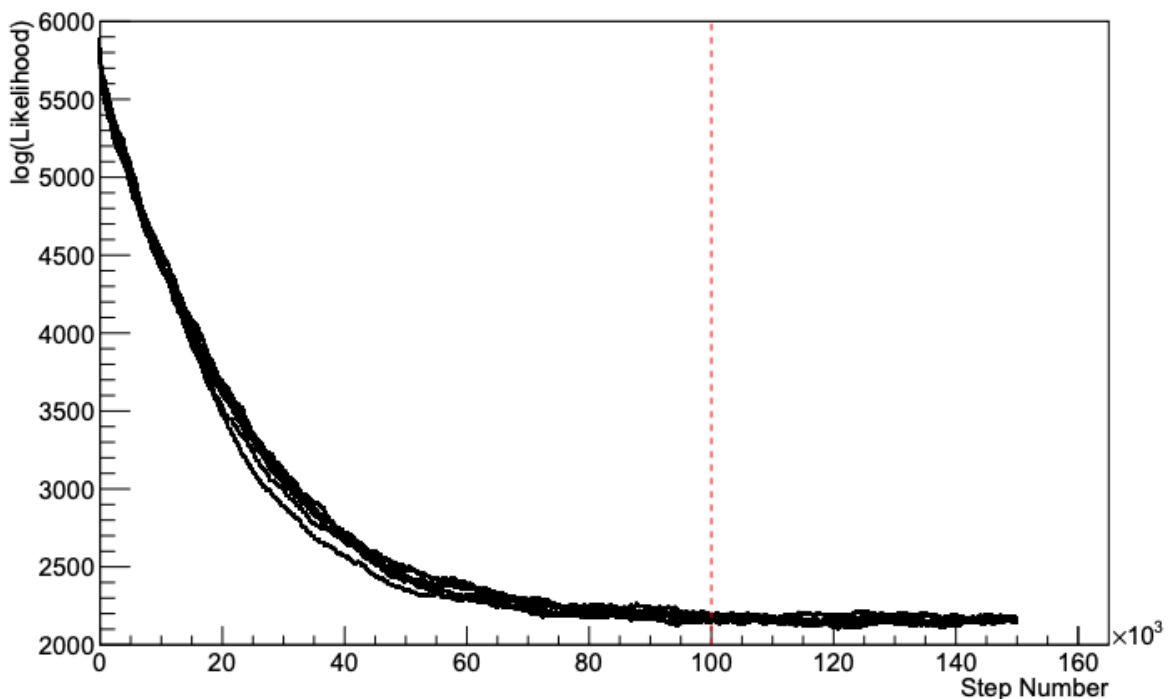


**Figure 3.4:** The log-likelihood from the fit detailed in [DB: Link to AsimovA](#) [Sensitivity Section](#) as a function of the number of steps accumulated in each fit. Many independent MCMC chains were run in parallel and overlaid on this plot. The red line indicates the  $1 \times 10^5$  step burn-in period after which the log-likelihood becomes stable.

### <sup>1073</sup> 3.3 Understanding the MCMC Results

<sup>1074</sup> Whilst section 3.1 and section 3.2 describe how to interpret Bayesian statistics and  
<sup>1075</sup> explains the MCMC techniques used within this analysis, there is no mention of  
<sup>1076</sup> how to interpret the output of the chain. The posterior distribution output from the  
<sup>1077</sup> chain is a high dimension object, with as many dimensions as there are parameters  
<sup>1078</sup> included in the fit. However, this multi-dimensional object is difficult to conceptualize  
<sup>1079</sup> so parameter estimations are often presented in one or two-dimensional projections  
<sup>1080</sup> of this probability distribution. To do this, we invoke the marginalisation technique  
<sup>1081</sup> highlighted in subsection 3.3.1.

#### <sup>1082</sup> 3.3.1 Marginalisation

<sup>1083</sup> The output of the MCMC chain is a highly dimensional probability distribution  
<sup>1084</sup> which is very difficult to interpret. From the standpoint of an oscillation analysis  
<sup>1085</sup> experiment, the one or two-dimensional ‘projections’ of the oscillation parameters of  
<sup>1086</sup> interest are most relevant. Despite this, the best fit values and uncertainties on the  
<sup>1087</sup> oscillation parameters of interest should correctly encapsulate the correlations to the  
<sup>1088</sup> other systematic uncertainties (colloquially called ‘nuisance’ parameters). For this joint  
<sup>1089</sup> beam and atmospheric analysis, the oscillation parameters of interest are  $\sin^2(\theta_{23})$  ,  
<sup>1090</sup>  $\sin^2(\theta_{13})$  ,  $\Delta m_{23}^2$  , and  $\delta_{CP}$  . All other parameters (Including the oscillation parameter  
<sup>1091</sup> this fit is insensitive to) are deemed nuisance parameters. To generate these projections,  
<sup>1092</sup> we rely upon integrating the posterior distribution over all nuisance parameters. This  
<sup>1093</sup> is called marginalisation. A simple example of this technique is to imagine the scenario  
<sup>1094</sup> where two coins are flipped. To determine the probability that the first coin returned  
<sup>1095</sup> a ‘head’, the exact result of the second coin flip is disregarded and simply integrated

over. For the parameters of interest,  $\vec{\theta}_i$ , we can calculate the marginalised posterior by integrating over the nuisance parameters,  $\vec{\theta}_n$ . In this case, Equation 3.2 becomes

$$P(\vec{\theta}_i|D) = \frac{\int P(D|\vec{\theta}_i, \vec{\theta}_n)P(\vec{\theta}_i, \vec{\theta}_n)d\vec{\theta}_n}{\int P(D|\vec{\theta})P(\vec{\theta})d\vec{\theta}} \quad (3.7)$$

Where  $P(\vec{\theta}_i, \vec{\theta}_n)$  encodes the prior knowledge about the uncertainty and correlations between the parameters of interest and the nuisance parameters. In practice, this is simply taking the one or two-dimensional projection of the multi-dimensional probability distribution.

Whilst in principle an easy solution to a complex problem, correlations between the interesting and nuisance parameters can bias the marginalised results. A similar effect is found when the parameters being marginalised over have non-Gaussian probability distributions. For example, Figure 3.5 highlights the marginalisation bias in the probability distribution found for a parameter when requiring a correlated parameter to have a positive parameter value. Due to the complex nature of this oscillation parameter fit presented in this thesis, there are certainly correlations occurring between the oscillation parameters of interest and the other nuisance parameters included in the fit.

### 3.3.2 Parameter Estimation and Credible Intervals

The purpose of this analysis is to determine the best fit values for the oscillation parameters that the beam and atmospheric samples are sensitive to;  $\sin^2(\theta_{23})$  ,  $\sin^2(\theta_{13})$  ,  $\Delta m_{23}^2$  , and  $\delta_{CP}$  . Typically, the results presented take the form of one or two-dimension marginalised probability distributions for the appearance ( $\sin^2(\theta_{13})$  and  $\delta_{CP}$  ) and

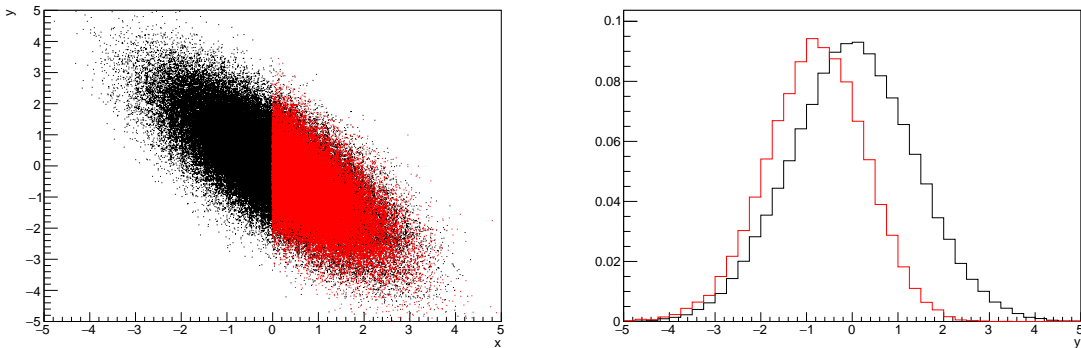


**Figure 3.5:** Left: The two dimensional probability distribution for two correlated parameters  $x$  and  $y$ . The red distribution shows the two dimensional probability distribution when  $0 \leq x \leq 5$ . Right: The marginalised probability distribution for the  $y$  parameter found when requiring the  $x$  to be bound between  $-5 \leq x \leq 5$  and  $0 \leq x \leq 5$  for the black and red distribution, respectively.

1116 disappearance ( $\sin^2(\theta_{23})$  and  $\Delta m_{23}^2$ ) parameters. The posterior probability density  
 1117 taken from the output MCMC chain is binned in these parameters. The parameter  
 1118 best-fit point is then taken to be the value that has the highest posterior probability.  
 1119 This is performed in both one and two-dimensional projections.

1120 However, the single best-fit point in a given parameter is not of much use on its  
 1121 own. We would also like to determine the uncertainty, or credible interval, on that  
 1122 best-fit point. The definition of the  $1\sigma$  credible interval is that we have 68% belief that  
 1123 the parameter is within those bounds. For a more generalised definition, the credible  
 1124 interval is the region of the posterior distribution that contains a specific fraction of  
 1125 the total probability, such that

$$\int P(\theta|D)d\theta = \alpha \quad (3.8)$$

1126 Where  $\theta$  is the parameter on which we calculate the credible interval. This technique  
 1127 then calculates the  $\alpha \times 100\%$  credible interval.

In practice, this analysis uses the highest posterior density (HPD) credible intervals which are calculated through the following method. First, the probability distribution is area-normalised such that it has an integrated area equal to 1.0. The bins of probability are then summed from the highest to lowest until the sum exceeds the  $1\sigma$  level (0.68 in this example). This process is repeated for a range of credible intervals, notably the  $1\sigma$ ,  $2\sigma$  and  $3\sigma$  along with other levels where the critical values for each level can be found in [128]. This process can be repeated for the two-dimensional probability distributions by creating two-dimensional contours of credible intervals rather than a one-dimensional result.

### 3.3.3 Application of Bayes' Theorem

Due to the matter resonance, this analysis has some sensitivity to the mass hierarchy of neutrino states (whether  $\Delta m_{23}^2$  is positive or negative) and the octant of  $\sin^2(\theta_{23})$ . The Bayesian approach utilised within this analysis gives an intuitive method of model comparison by determining which hypothesis is most favourable. Taking the ratio of Equation 3.3 for the two hypotheses of normal hierarchy,  $NH$ , and inverted hierarchy,  $IH$ , gives

$$\frac{P(\vec{\theta}_{NH}|D)}{P(\vec{\theta}_{IH}|D)} = \frac{P(D|\vec{\theta}_{NH})}{P(D|\vec{\theta}_{IH})} \times \frac{P(\vec{\theta}_{NH})}{P(\vec{\theta}_{IH})}. \quad (3.9)$$

The middle term defines the Bayes factor which is a data-driven interpretation of how strong the data prefers one hierarchy to the other. For this analysis, equal priors on both mass hierarchy hypotheses are chosen ( $P(\vec{\theta}_{NH}) = P(\vec{\theta}_{IH}) = 0.5$ ). In practice, the MCMC chain proposes a value of  $|\Delta m_{23}^2|$  and then applies a 50% probability that the value is sign flipped. Consequently, the Bayes factor can be calculated from

1149 the ratio of the probability density in either hypothesis. This equates to counting the  
1150 number of steps taken in the normal and inverted hierarchies and taking the ratio. The  
1151 same approach can be taken to compare the upper octant (UO) compared to the lower  
1152 octant (LO) hypothesis of  $\sin^2(\theta_{23})$ .

1153 Whilst the value of the Bayes factor should always be shown, the Jeffreys scale [129]  
1154 (highlighted in Table 3.1) gives an indication of the strength of preference for one model  
1155 compared to the other. Other interpretations of the strength of preference of a model  
1156 exist, e.g. the Kass and Raferty Scale [130].

$\log_{10}(B_{AB})$	$B_{AB}$	Strength of Preference
< 0.0	< 1	No preference for hypothesis A (Supports hypothesis B)
0.0 – 0.5	1.0 – 3.16	Preference for hypothesis A is weak
0.5 – 1.0	3.16 – 10.0	Preference for hypothesis A is substantial
1.0 – 1.5	10.0 – 31.6	Preference for hypothesis A is strong
1.5 – 2.0	31.6 – 100.0	Preference for hypothesis A is very strong
> 2.0	> 100.0	Decisive preference for hypothesis A

**Table 3.1:** Jeffreys scale for strength of preference for two models  $A$  and  $B$  as a function of the calculated Bayes factor ( $B_{AB} = B(A/B)$ ) between the two models [129]. The original scale is given in terms of  $\log_{10}(B(A/B))$  but converted to linear scale for easy comparison throughout this thesis.

### 1157 3.3.4 Comparison of MCMC Output to Expectation

1158 Whilst not important for the extraction of oscillation parameters, understanding how  
1159 the data constrains the model parameters is important to the understanding of this  
1160 analysis. A simple method of doing this is to perform a comparison in the fitting  
1161 parameters (For instance, the reconstructed neutrino energy and lepton direction for  
1162 T2K far detector beam samples) of the spectra generated by the MCMC chain to ‘data’.  
1163 This ‘data’ could be true data or some variation of Monte Carlo prediction. This allows  
1164 easy comparison of the MCMC probability distribution to the data. To perform this,  $N$

1165 steps from the post burn-in MCMC chain are randomly selected (Where for all plots  
1166 of this style in this thesis,  $N = 3000$ ). From these, the Monte Carlo prediction at each  
1167 step is generated by reweighting the model parameters to the values specified at that  
1168 step. Due to the probability density being directly correlated with the density of steps  
1169 in a certain region, parameter values close to the best fit value are most likely to be  
1170 selected.

1171 In practice, for each bin of the fitting parameters has a probability distribution  
1172 of event rates, with one entry per sampled MCMC step. This distribution is binned  
1173 where the bin with the highest probability is selected as the mean and an error on  
1174 the width of this probability distribution is calculated using the approach highlighted  
1175 in subsection 3.3.2. Consequently, the best fit distribution in the fit parameter is not  
1176 necessarily that which would be attained by reweighting the Monte Carlo prediction  
1177 to the most probable parameter values.

1178 A similar study can be performed to illustrate the freedom of the model parameter  
1179 space prior to the fit. This can be done by throwing parameter values from the prior  
1180 uncertainty of each parameter. This becomes troublesome for parameters with no  
1181 prior uncertainty as the range is technically infinite. Where applicable solutions to  
1182 remove these have been addressed.

<sub>1183</sub> **Chapter 4**

<sub>1184</sub> **Oscillation Probability Calculation**

<sub>1185</sub> The calculation of the oscillation probability is crucial to the reliability of the sensitivity  
<sub>1186</sub> measurements of the analysis presented within this thesis. Firstly, it is important to  
<sub>1187</sub> understand how and where the sensitivity to the oscillation parameters come from  
<sub>1188</sub> for both atmospheric and beam samples. An overview of how these sets of samples  
<sub>1189</sub> observe changes in  $\delta_{CP}$ ,  $\Delta m_{23}^2$  and  $\sin^2(\theta_{23})$  as well as how the atmospheric samples  
<sub>1190</sub> have an increased sensitivity to mass hierarchy determination is given in section 4.1.  
<sub>1191</sub> It also explains the additional complexities involved when including atmospheric  
<sub>1192</sub> neutrinos as compared to a beam-only analysis.

<sub>1193</sub> Without additional techniques, atmospheric sub-GeV upward-going neutrinos can  
<sub>1194</sub> artificially inflate the sensitivity to  $\delta_{CP}$  due to the quickly varying oscillation probabil-  
<sub>1195</sub> ity in this region. Therefore, a “sub-sampling” approach has been developed to reduce  
<sub>1196</sub> these biases ensuring accurate and reliable sensitivity measurements. This technique  
<sub>1197</sub> ensures that small-scale unresolvable features of the oscillation probability have been  
<sub>1198</sub> averaged over whilst the large-scale resolvable features in the oscillation probability  
<sub>1199</sub> have been kept. The documentation of this technique is found in section 4.2 alongside  
<sub>1200</sub> the validation of the choices which have been made. The CUDAProb3 implementation  
<sub>1201</sub> choice made within the fitting framework, as detailed in section 4.3, ensures that the  
<sub>1202</sub> analysis can be done in a timely manner.

<sub>1203</sub> Whilst the beam neutrinos are assumed to propagate through a constant density  
<sub>1204</sub> slab of material, the density variations through the Earth result in more complex  
<sub>1205</sub> oscillation patterns Furthermore, the uncertainty in the electron density can modify

the oscillation probability for the denser core-layers of the Earth. section 4.4 details the model of the Earth used within this analysis. This includes the official SK-only methodology as well as a relatively straight forward improvement which can be made to more closely approximate the PREM model. Another quirk of atmospheric neutrinos oscillation studies is that the height of production in the atmosphere is not known on an event-by-event analysis. An analytical averaging technique that approximates the uncertainty on the oscillation probability has been followed, with the author of this thesis being responsible for the implementation and validation. This technique is illustrated in section 4.5 alongside the variation in oscillation probability which would be expected effect in the down-going and horizontal-going neutrinos.

## 4.1 Overview

The analysis presented within this thesis focuses on the determination of oscillation parameters from atmospheric and beam neutrinos. Whilst subject to the same oscillation probability, the way in which the two sets of samples have sensitivity to the different oscillation parameters differs quite significantly.

Atmospheric neutrinos have a varying baseline, or “path length”, such that the distance each neutrino travels before interacting is dependent upon the zenith angle. Therefore the oscillation probability can be represented as a two-dimensional “oscillogram” as shown in Figure 4.1. For this calculation, four layers of fixed density were used to model the Earth with values taken from an approximation of the PREM model. These can be seen in the distinct discontinuities in the oscillogram as a function of the zenith angle.

Another complexity of atmospheric neutrino oscillation probability calculation is the uncertainty in the height at which a neutrino was produced, termed the “produ-

tion height". Primary cosmic rays, whch contribute most of the neutrino flux, can interact anywhere between the Earth's surface and  $\sim 50\text{km}$  above that. The baseline,  $L$ , for a neutrino generated with zenith angle,  $\theta$ , and production height,  $h$ , can be calculated as

$$L = \sqrt{(R_E + h)^2 - R_E^2 (1 - \cos^2(\theta))} - R_E \cos(\theta), \quad (4.1)$$

where  $R_E = 6,371\text{km}$  is the Earth's radius.

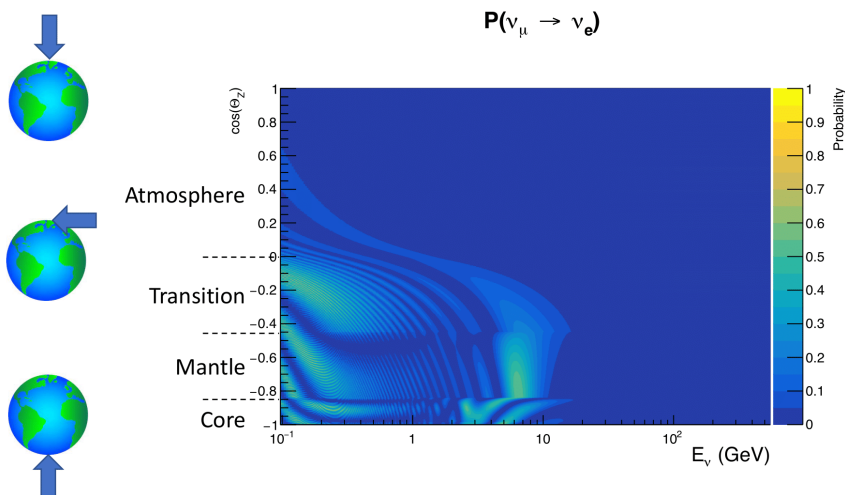


**Figure 4.1:** An "Oscillogram" that depicts the  $P(\nu_\mu \rightarrow \nu_e)$  oscillation probability as a function of neutrino energy and cosine of the zenith angle. The zenith angle is defined such that  $\cos(\theta_Z) = 1.0$  represents neutrinos that travel from directly above the detector. The four-layer constant density PREM model approximation is used and Asimov A oscillation parameters are assumed.

Atmospheric neutrinos do have some sensitivity to  $\delta_{CP}$  through a normalisation term. Figure 4.2 illustrates the difference in oscillation probability between CP-conserving and CP-violating  $\delta_{CP}$  values. The result is a complicated oscillation pattern in the appearance probability for sub-GeV upgoing neutrinos. The detector does not have sufficient resolution to resolve these individual patterns so the sensi-

tivity to  $\delta_{CP}$  for atmospheric neutrinos comes via the overall normalisation of the sub-GeV upgoing events. The presence of matter means that the effect  $\delta_{CP}$  has on the oscillation probability is not equal between neutrinos and antineutrinos which would be expected when propagating through a vacuum. This is further extenuated by the fact that SK can not distinguish neutrinos and antineutrinos well and that the cross-section neutrino interaction is larger than that for antineutrinos. Finally, sample selections (discussed in [DB: Link to selection chapter](#)) targeting different neutrino interaction modes (charge current quasi-elastic and single pion production) result in an imbalance in the percentage of neutrinos to anti-neutrinos in these samples due to pion capture. Negatively charged pions from antineutrino interactions are more likely to be captured by a nucleus compared to a positively charged pion emitted from a neutrino interaction. This all culminates in atmospheric neutrinos having a very complex sensitivity to  $\delta_{CP}$ .

Atmospheric neutrinos are subject to matter effects as they travel through the dense matter in the Earth. The vacuum and matter oscillation probabilities for  $P(\nu_e \rightarrow \nu_e)$  and  $P(\bar{\nu}_e \rightarrow \bar{\nu}_e)$  are presented in Figure 4.3. The oscillation probability for both neutrinos and antineutrinos are affected in the presence of matter but the resonance (Effects around  $E_\nu \sim 5\text{GeV}$ ) only occurs for neutrinos in normal mass hierarchy and antineutrinos for inverse mass ordering. The exact position and amplitude of the resonance depend on  $\sin^2(\theta_{23})$  meaning that the atmospheric neutrinos have sensitivity to the octant of  $\theta_{23}$ .

As the T2K beam flux is centered at the first oscillation maximum, the sensitivity to  $\delta_{CP}$  is predominantly observed as a change in the event-rate of e-like samples in  $\nu/\bar{\nu}$  modes. Figure 4.4 illustrates the  $P(\nu_\mu \rightarrow \nu_e)$  oscillation probability for a range of  $\delta_{CP}$  values. A circular modulation of the oscillation peak (in both magnitude and position) is observed when varying throughout the allowable values of  $\delta_{CP}$ . The CP-

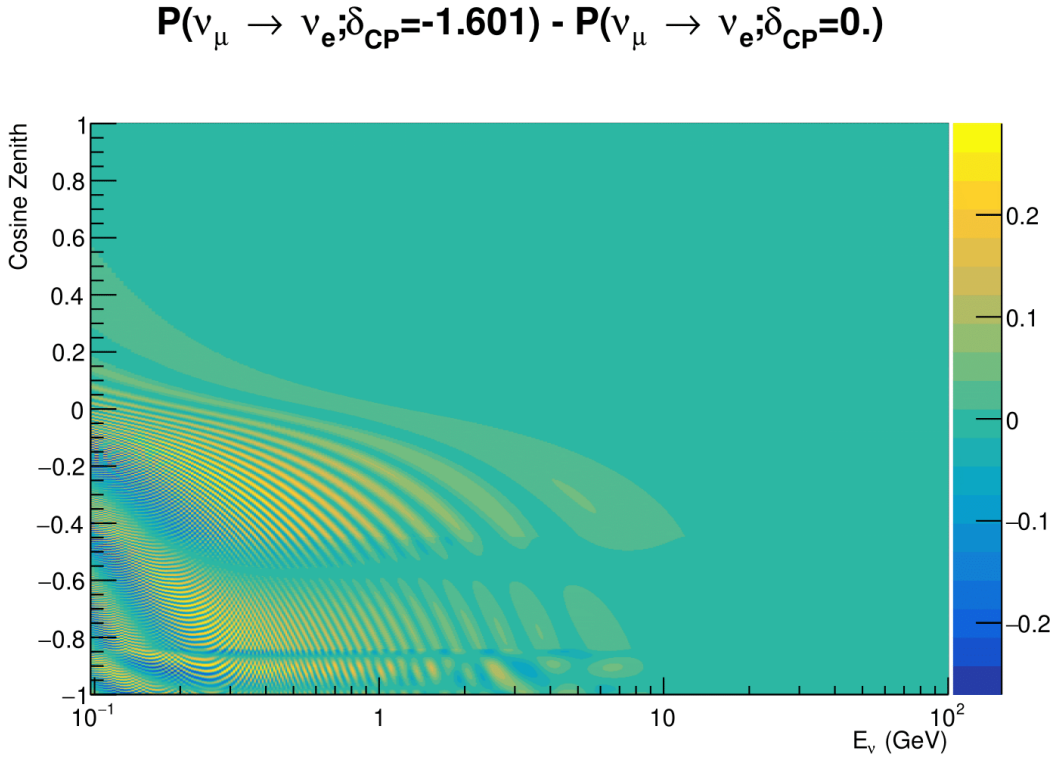


**Figure 4.2:** The effect of  $\delta_{CP}$  for atmospheric neutrinos given in terms of the neutrino energy and zenith angle. The oscillogram compares the  $P(\nu_\mu \rightarrow \nu_e)$  oscillation probability for a CP conserving ( $\delta_{CP} = 0.0$ ) and CP violating ( $\delta_{CP} = -1.601$ ) value of  $\delta_{CP}$ . The other oscillation parameters assume the “Asimov A” oscillation parameter set given in Table 4.1.

1266 conserving values of  $\delta_{CP} = 0, \pi$  have a lower(higher) oscillation maximum than the  
 1267 CP-violating values of  $\delta_{CP} = -\pi/2 (\delta_{CP} = \pi/2)$  leading to a  $\sin(\delta_{CP})$  type sensitivity.  
 1268 A sub-dominant shift in the energy of the oscillation peak is also present to aid in  
 1269 separating the two CP-conserving values of  $\delta_{CP}$ .

1270 T2K’s sensitivity to the atmospheric oscillation parameters is more of a shape-  
 1271 based variation of the muon-like samples, as illustrated in Figure 4.4. The value of  
 1272  $\Delta m_{32}^2$  laterally shifts the position of the oscillation dip (around  $E_\nu \sim 0.6$ GeV) in the  
 1273  $P(\nu_\mu \rightarrow \nu_\mu)$  oscillation probability. A variation of  $\sin^2(\theta_{23})$  is predominantly observed  
 1274 as a vertical shift of the oscillation dip with second-order horizontal shifts being due  
 1275 to matter effects. The beam neutrinos have limited sensitivity to matter effects due

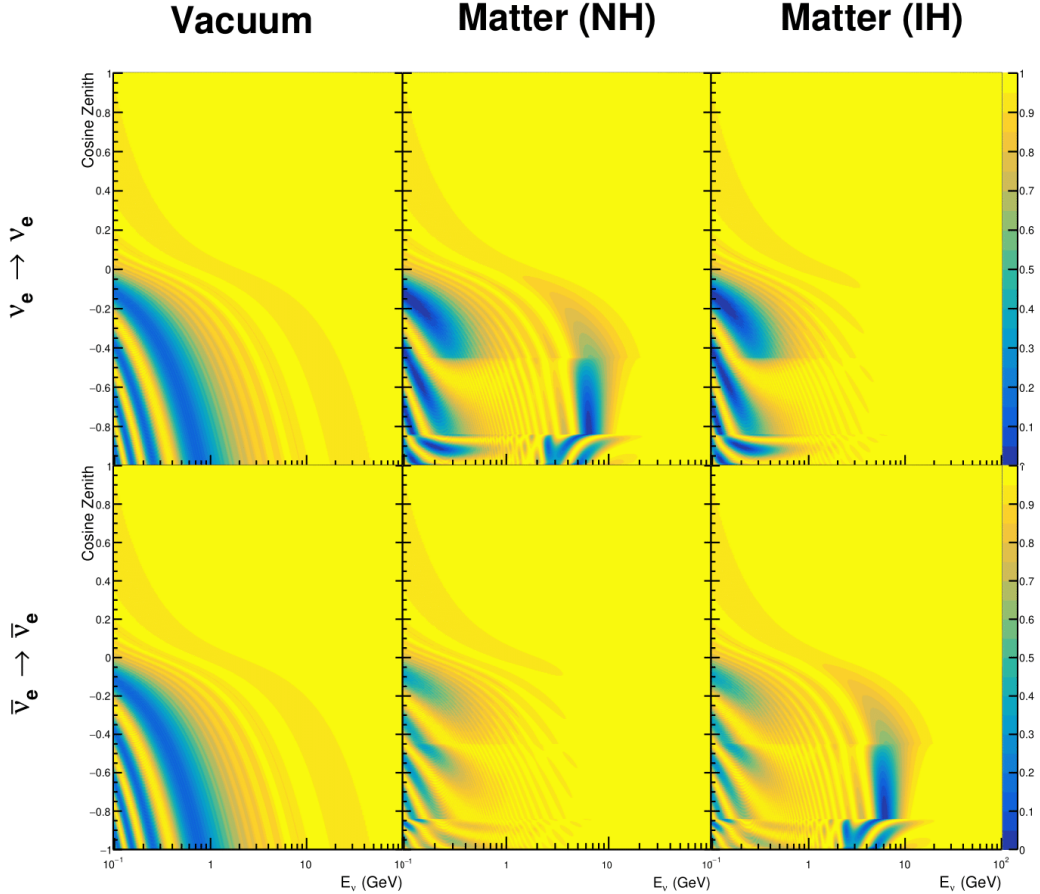


**Figure 4.3:** An illustration of the matter-induced effects on the oscillation probability, given as a function of neutrino energy and zenith angle. The top row of panels gives the  $P(\nu_e \rightarrow \nu_e)$  oscillation probability and the bottom row illustrates the  $P(\bar{\nu}_e \rightarrow \bar{\nu}_e)$  oscillation probability. The left column highlights the oscillation probability in a vacuum, whereas the middle and right column represents the oscillation probabilities when the four layer fixed density PREM model is assumed. All oscillation probabilities assume the “Asimov A” set given in Table 4.1, but importantly, the right column sets an inverted mass hierarchy. The “matter resonance” effects at  $E_\nu \sim 5\text{GeV}$  can be seen in the  $P(\nu_e \rightarrow \nu_e)$  for normal mass hierarchy and  $P(\bar{\nu}_e \rightarrow \bar{\nu}_e)$  for inverted hierarchy.

to the shorter baseline as well as the Earth’s mantle is relatively low-density material (as compared to the Earth’s core). For some values of  $\delta_{CP}$ , the degeneracy in the number of e-like events allows the mass hierarchy to be resolved. This leads to a  $\delta_{CP}$ -dependent mass hierarchy sensitivity. **DB: Bi-probability plot?**

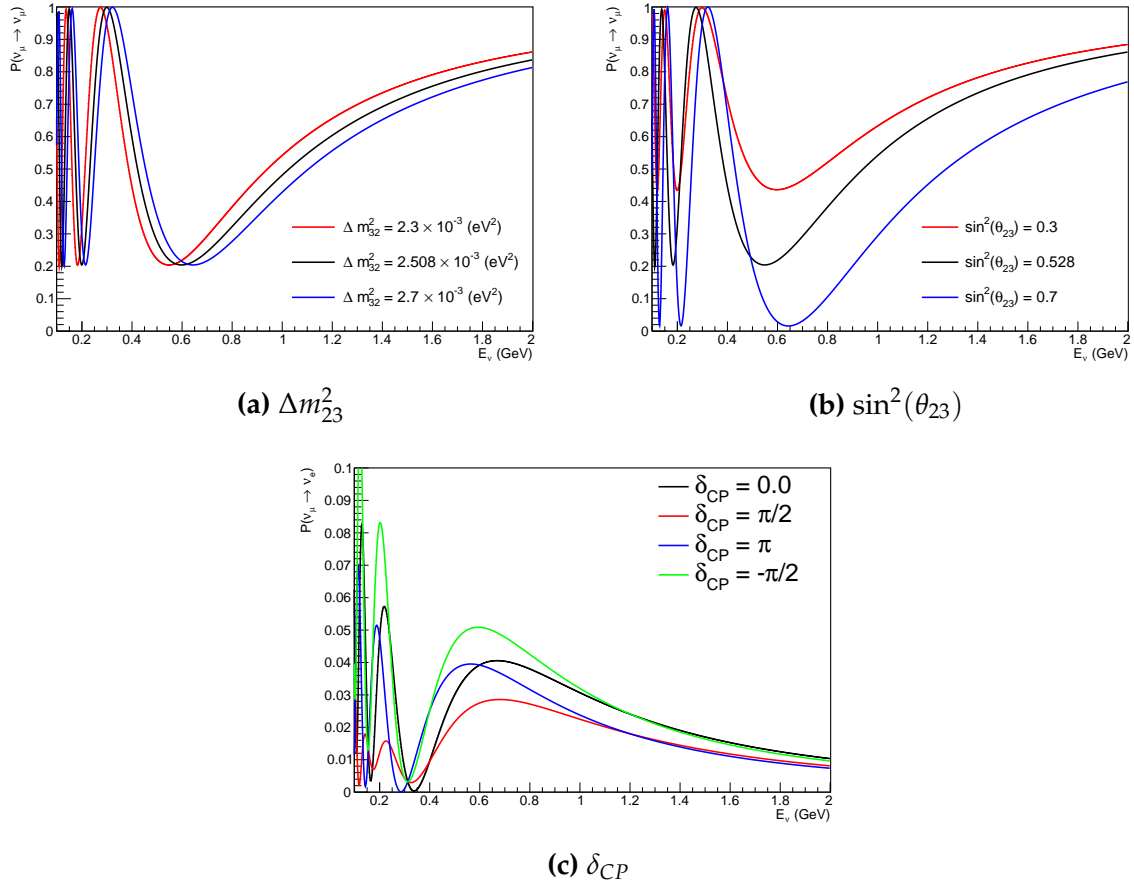


**Figure 4.4:** The oscillation probability for beam neutrino events, given as a function of neutrino energy. All oscillation parameters assume the “Asimov A” set given in Table 4.1 unless otherwise stated. Each panel represents a change in one of the oscillation parameters whilst keeping the remaining parameters fixed.

Whilst all oscillation channels should be included for completeness, the computational resources required to run a fit are limited and any reasonable approximations which reduce the number of oscillation probability calculations which need to be made should be applied. The  $\nu_e \rightarrow \nu_{e,\mu,\tau}$  (and antineutrino equivalent) oscillations can be ignored for beam neutrinos as the  $\nu_e/\bar{\nu}_e$  fluxes being approximately two orders of magnitude smaller than the corresponding  $\nu_\mu/\bar{\nu}_\mu$  flux. Furthermore, as the peak neutrino energy of the beam is well below the threshold for  $\tau$  production ( $E_\nu \sim 3\text{GeV}$  [131]) only a small proportion of the neutrinos produced in the beam have the required energy. For the few neutrinos that have sufficient energy, the oscillation probability is very small due to the short baseline. Whilst these approximations can be made for the

1290 beam neutrinos, the atmospheric flux of  $\nu_e$  is of the same order of magnitude as the  $\nu_\mu$   
1291 flux and the energy distribution of atmospheric neutrinos extends well above the tau  
1292 production threshold.

1293 Throughout this thesis, several spectra predictions, Asimov fits, and contour com-  
1294 parisons are presented which require oscillation parameters to be assumed. Table 4.1  
1295 defines two sets of oscillation parameters, with “Asimov A” set being close to the  
1296 preferred values from a previous T2K-only fit [DB: Need Citation](#) and “Asimov B”  
1297 being CP-conserving and further from maximal  $\theta_{23}$  mixing.

Parameter	Asimov A	Asimov B
$\Delta m_{12}^2$	$7.53 \times 10^{-5} \text{ eV}^2$	
$\Delta m_{32}^2$	$2.509 \times 10^{-3} \text{ eV}^2$	
$\sin^2(\theta_{12})$	0.304	
$\sin^2(\theta_{13})$	0.0219	
$\sin^2(\theta_{23})$	0.528	0.45
$\delta_{CP}$	-1.601	0.0

**Table 4.1:** Reference values of the neutrino oscillation parameters for two different oscillation parameter sets.

## 1298 4.2 Treatment of Fast Oscillations

1299 As shown in Figure 4.5, atmospheric neutrino oscillations have a significantly more  
1300 complex structure for upgoing neutrinos with energy below 1GeV. This is because the  
1301  $L/E$  dependence of the oscillation probability in this region induces rapid variations  
1302 for small changes in  $L$  or  $E$ . As discussed in section 4.1, this is also the region in which  
1303 atmospheric neutrinos have sensitivity to  $\delta_{CP}$ . In practice, the direction between  
1304 the detector and a neutrino’s production vertex is inferred from the direction of any  
1305 secondary particles created in the detector target. For low energy neutrinos, this

1306 inference can be rather poor and introduces a distinct difference to beam neutrinos  
1307 where the direction to production vertex is very well known.

1308 As a consequence of the poor detector resolution, an average oscillation probability  
1309 is observed in this region. This creates a computational problem as a significantly  
1310 large amount of MC statistics would be required to accurately predicted the number  
1311 of events in each bin if MC averaging was the only technique used. This section  
1312 describes the ‘sub-sampling’ approach developed for this analysis and compares it to  
1313 the methodology used within the SK-only analysis.

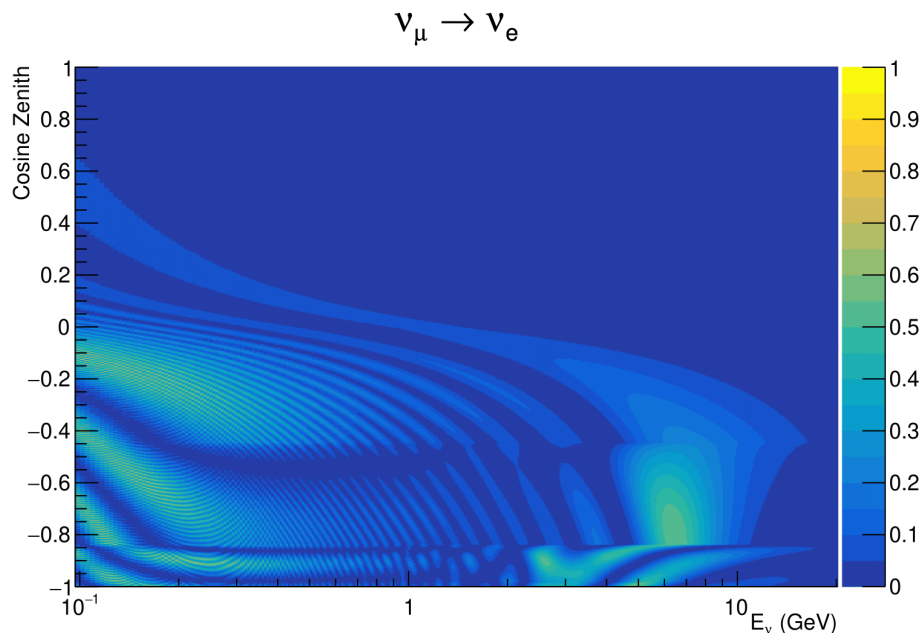


**Figure 4.5:** The oscillation probability  $P(\nu_\mu \rightarrow \nu_e)$ , given as a function of neutrino energy and zenith angle, which highlights an example of the “fast” oscillations in the sub-GeV upgoing region.

1314 The official SK-only analysis uses the osc3++ oscillation parameter fitter [132]. To  
1315 perform the fast oscillation averaging, it uses a ‘nearest-neighbour’ technique. For a  
1316 given neutrino MC event, the nearest neighbours in reconstructed lepton momentum  
1317 and zenith angle are found and a distribution of neutrino energies is built. This

<sub>1318</sub> distribution is then used to compute an average oscillation probability for the given  
<sub>1319</sub> neutrino MC event.

<sub>1320</sub> For the  $i^{th}$  event, the oscillation weight is calculated as

$$W_i = \frac{1}{5}P(E_i, \bar{L}_i) + \frac{1}{5} \sum_{\beta=-1,-0.5,0.5,1} P(E_i + \beta\sigma_i, L_\beta), \quad (4.2)$$

<sub>1321</sub> where  $P(E, L)$  is the oscillation probability calculation for neutrino energy  $E$  and  
<sub>1322</sub> path length  $L$ ,  $\sigma_i$  is the RMS of the energy distribution for the given event, and the  
<sub>1323</sub> two path lengths,  $\bar{L}_i$  and  $L_\beta$  are discussed below. In practice, twenty of the nearest  
<sub>1324</sub> neighbours are used to generate the neutrino energy distribution. All of the oscillation  
<sub>1325</sub> probability calculations are performed with a fixed zenith angle (and therefore have  
<sub>1326</sub> same matter density profile).

<sub>1327</sub> The uncertainty in the production height is controlled by using an “average” pro-  
<sub>1328</sub> duction height.  $\bar{L}_i$  represents the average path length computed using twenty produc-  
<sub>1329</sub> tion heights taken from the Honda flux model’s prediction DB: Need citation for a  
<sub>1330</sub> fixed zenith angle, where the production heights are sampled in steps of 5% of their  
<sub>1331</sub> cumulative distribution function.  $L_\beta$  values are similarly calculated but instead use  
<sub>1332</sub> different combinations of four production heights (sampled in the same way),

$$\begin{aligned} L_{-1.0} &= \frac{1}{4}L(45, 50, 55, 60), \\ L_{-0.5} &= \frac{1}{4}L(35, 40, 65, 70), \\ L_{+0.5} &= \frac{1}{4}L(25, 30, 75, 68), \\ L_{+1.0} &= \frac{1}{4}L(15, 20, 85, 89). \end{aligned} \quad (4.3)$$

1333     This averaging works well because of the correlation between true neutrino zenith  
1334   angle and the inferred direction from secondary particles in the detector. For low  
1335   energy neutrinos, where the resolution of the true neutrino direction is poor,  $\sigma_i$  will be  
1336   large resulting in significant averaging effects. Contrary to this, the inferred direction  
1337   of high energy neutrinos will be much closer to the true value, meaning that  $\sigma_i$  will be  
1338   smaller.

1339     In practice, this technique is performed before the fit in order to deal with the  
1340   computational cost. Oscillation probabilities are pre-calculated on a 4D grid. This  
1341   is possible as the Osc3++ framework uses binned oscillation parameters rather than  
1342   continuous so the oscillation parameters used in the fit are known prior to run-time. The  
1343   framework used in the analysis presented within this thesis uses continuous oscillation  
1344   parameters. Due to the MCMC technique invoked within the fitter (see chapter 3),  
1345   there is no way to know which oscillation parameter values will be selected in each  
1346   step at run-time. Therefore, the oscillation parameter calculation would have to  
1347   be performed at run-time which is very expensive for event-by-event reweighting.  
1348   Having to compute five oscillation probabilities per event would require far too much  
1349   computational resources to be viable so the SK technique can not be used within this  
1350   analysis. However, the concept of the averaging technique can be taken from it.

1351     This analysis uses a binned oscillogram in which oscillation probabilities for a given  
1352   event are selected based on that event's attributes. To perform a similar averaging as  
1353   the SK analysis, a sub-sampling approach has been devised. The technique can be  
1354   explained by considering a "fine" and "coarse" oscillogram. The fine oscillograms  
1355   are used to define the array of cosine zeniths and energies for the neutrino oscillation  
1356   engine. The coarse oscillograms cover the same phasespace as the fine oscillograms  
1357   but have fewer bins in that range. Then, for a given coarse oscillogram bin, the value

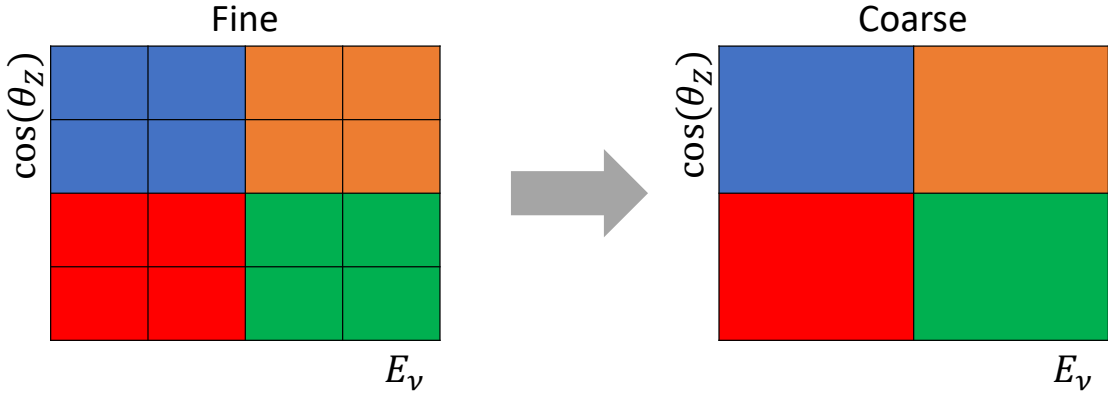


**Figure 4.6:** Illustration of the averaging procedure for  $N = 2$ . The oscillation probabilities calculated on the finer left binning are averaged to obtain the oscillation probabilities in the coarser right binning. These averaged oscillation probabilities with the coarser binning are then applied to each event during the fit.

1358 of that bin will be taken as the average of all the oscillation probabilities of all the fine  
 1359 oscillogram bins which fall into that coarse oscillogram bin.

1360 The binning which is used to calculate the oscillation probabilities, known as the  
 1361 ‘fine’ binning, has  $N \times N$  subdivisions per coarse bin. The value assigned to a coarse  
 1362 bin is the linear average (flat prior in  $E_\nu$  and  $\cos(\theta_Z)$ ) of all the oscillation probabilities  
 1363 calculated at the center of each fine bin contained within that coarse bin. Figure 4.6  
 1364 illustrates the  $N = 2$  example where the assigned value to a coarse bin is the linear  
 1365 average of the four fine bins which fall in that coarse bin. Whilst the coarse bin edges  
 1366 are not linear in either axis, the sub-division of the fine bins is linear over the range  
 1367 of a coarse bin. The alignment of the fine and coarse binning edges are checked at  
 1368 run-time.

1369 The coarse binning is defined with  $67 \times 52$  bins in true neutrino energy  $\times$  cosine  
 1370 zenith. In general, the binning is logarithmically spaced in neutrino energy but has  
 1371 some hand-picked bin edges. Firstly, the bin density around the matter resonance is  
 1372 smoothly increased around the matter resonance region. This is to avoid smearing  
 1373 this region which can be well sampled by the Monte Carlo. Secondly, bin edges  
 1374 are selected to hit 0.4, 0.6, 1, 10, 30, 50, 100GeV. This is to ensure that the Coloumb

correction systematic and the atmospheric flux systematics definitions in neutrino energy can be hit. The cosine zenith binning is approximately linearly spaced across the allowable range but the values of layer transitions are hit precisely;  $-0.8376$  (core-mantle) and  $-0.4464$  (mantle/transition zone). Bins are spread further apart for downgoing events as this is a region unaffected by the fast oscillation wavelengths and reduces the total number of calculations required to perform the reweight (Not the number required to perform the oscillation calculation).

The choice of  $N$  is justified based on two studies. Firstly, the variation of event rates of each sample is studied as a function of the number of subdivisions. For a given set of oscillation parameters thrown from the PDG prior constraints, the oscillation probabilities are calculated using a given value of  $N$ . Each sample is reweighted and the event rate is stored. The value of  $N$  is scanned from 1, which corresponds to no averaging, to 24, which corresponds to the largest computationally viable subdivision binning. The event rate of each sample at large  $N$  is expected to converge to a stationary value due to the fine binning fully sampling the small scale structure. Figure 4.7 illustrates this behaviour for the SubGeV\_elike\_0dcy sample for 30 different throws of the oscillation parameters.

Denoting the event rate for one sample for a given throw  $t$  at each  $N$  by  $\lambda_t^{(N)}$ , the average over all considered  $N$  values ( $\bar{\lambda}_t = \frac{1}{24} \sum_{N=1}^{24} \lambda_t^{(N)}$ ) is computed. The variance in the event rate at each  $N$  is then calculated from

$$\text{Var}[\lambda^{(N)}] = \frac{1}{N_{\text{throws}}} \sum_{t=1}^{N_{\text{throws}}} (\lambda_t^{(N)} - \bar{\lambda}_t)^2 - \left[ \frac{1}{N_{\text{throws}}} \sum_{t=1}^{N_{\text{throws}}} (\lambda_t^{(N)} - \bar{\lambda}_t) \right]^2. \quad (4.4)$$

The aim of the study is to find the lowest value of  $N$  such that this variance is below 0.001. This is the typical threshold used by T2K fitters to validate systematic

### SubGeV-elike-0dcy

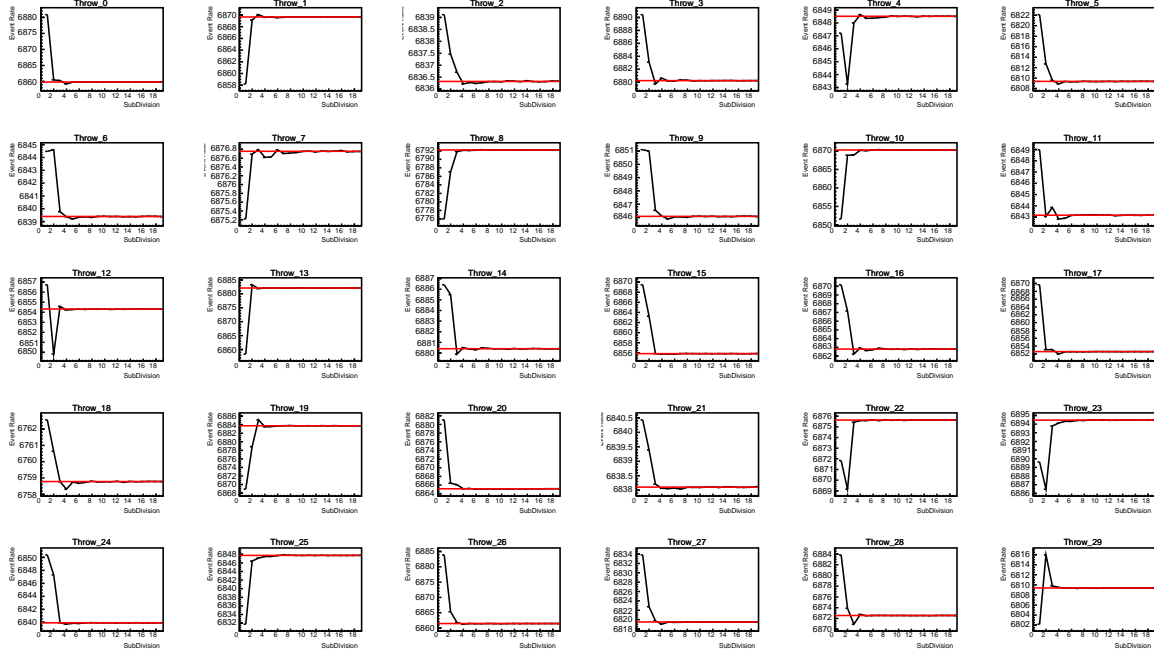


**Figure 4.7:** Event rate of the SubGeV\_elike\_0dcy sample as a function of the number of subdivisions per coarse bin. Each sub-plot represents the event rate of the sample at a different oscillation parameter set (thrown from the PDG priors). The red-line in each sub plot represents the mean of the event rate over the different values of subdivisions for that particular oscillation parameter throw.

implementation so is just as applicable to the oscillation probability calculation. The results of this study for each atmospheric sample used within this thesis are illustrated in Figure 4.8 for 2000 throws of the oscillation parameters. As can be seen, the variance is below the threshold at  $N = 10$ , and is driven primarily by the SubGeV\_mulike\_1dcy and SubGeV\_elike\_0dcy selections.

The second study to determine the value of  $N$  is as follows. The likelihood for each sample is computed against an Asimov data set created with oscillation parameters from “Asimov A” in Table 4.1. Following Equation 4.4, the variance of the log-likelihood over all considered  $N$  is computed. The results are shown in Figure 4.9. This tests the impact of the averaging on each sample’s binning by reconstructed

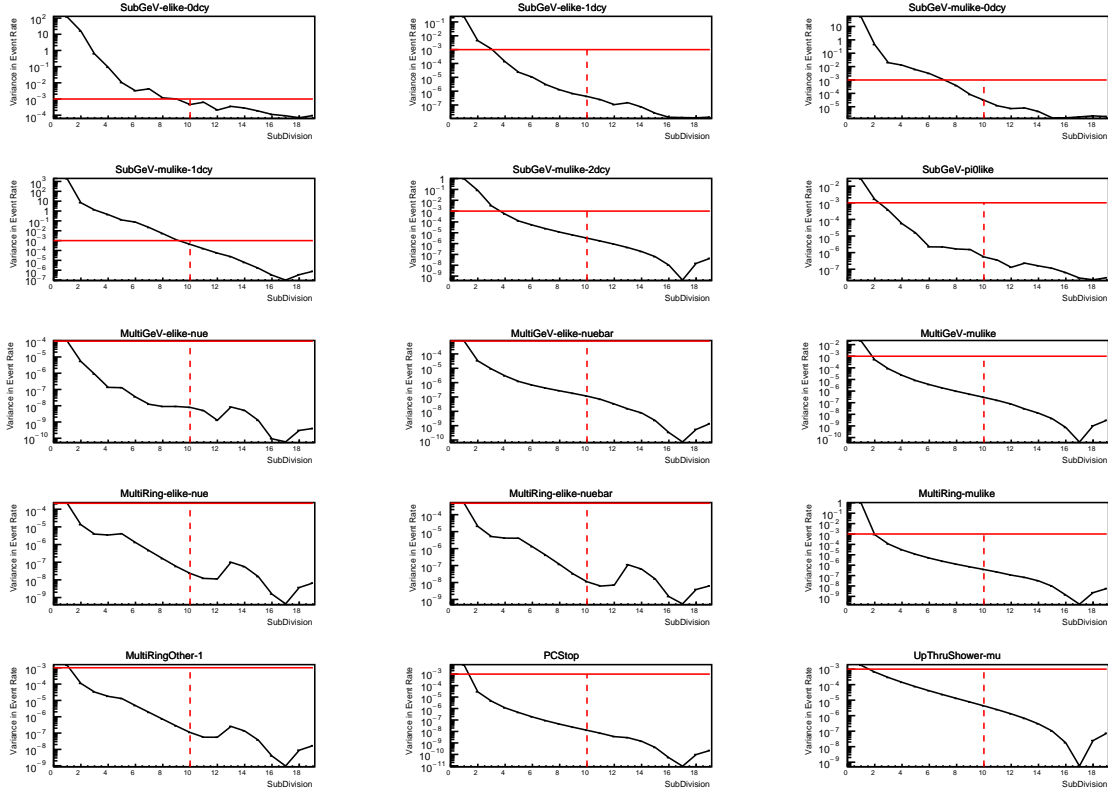


**Figure 4.8:** Variance of event rate for each atmospheric sample as a function of the number of sub-divisions per coarse bin. The solid red line indicates the 0.1% threshold and the dashed red line is a graphical indication of the variance at a sub-division  $N = 10$ .

1407 momentum and/or zenith angle and also provides a scale for the calculation errors  
 1408 compared to their statistical uncertainties.

1409 A choice of  $N$  sub-divisions per coarse bin has a variance in both event rate and  
 1410 log-likelihood residuals less than the required threshold of 0.001. The event rate test is  
 1411 the more stringent test. For the variance of log-likelihood residuals the largest value is  
 1412 of order  $10^{-7}$ , corresponding to an error on the log-likelihood of about  $3 \times 10^{-4}$ , small  
 1413 enough to be negligible for the oscillation analysis.

1414 In practice Figure 4.10 illustrates the effect of the smearing using  $N = 10$ . The fast  
 1415 oscillations in the sub-GeV upgoing region have been replaced with a normalisation  
 1416 effect whilst the large matter resonance structure remains.

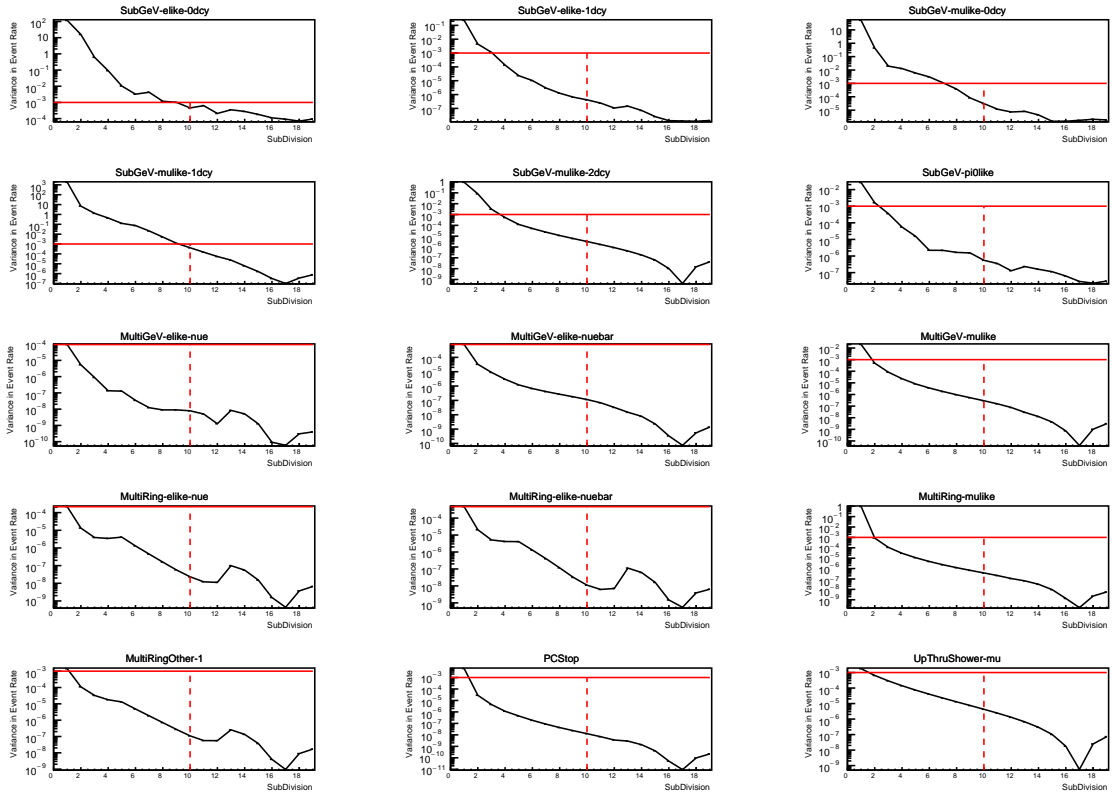


**Figure 4.9:** Variance of sample likelihood, when compared to ‘Asimov data’ set at Asimov A, for each atmospheric sample as a function of the number of sub-divisions per coarse bin. The solid red line indicates the 0.1% threshold and the dashed red line is a graphical indication of the variance at a sub-division  $N = 10$ .

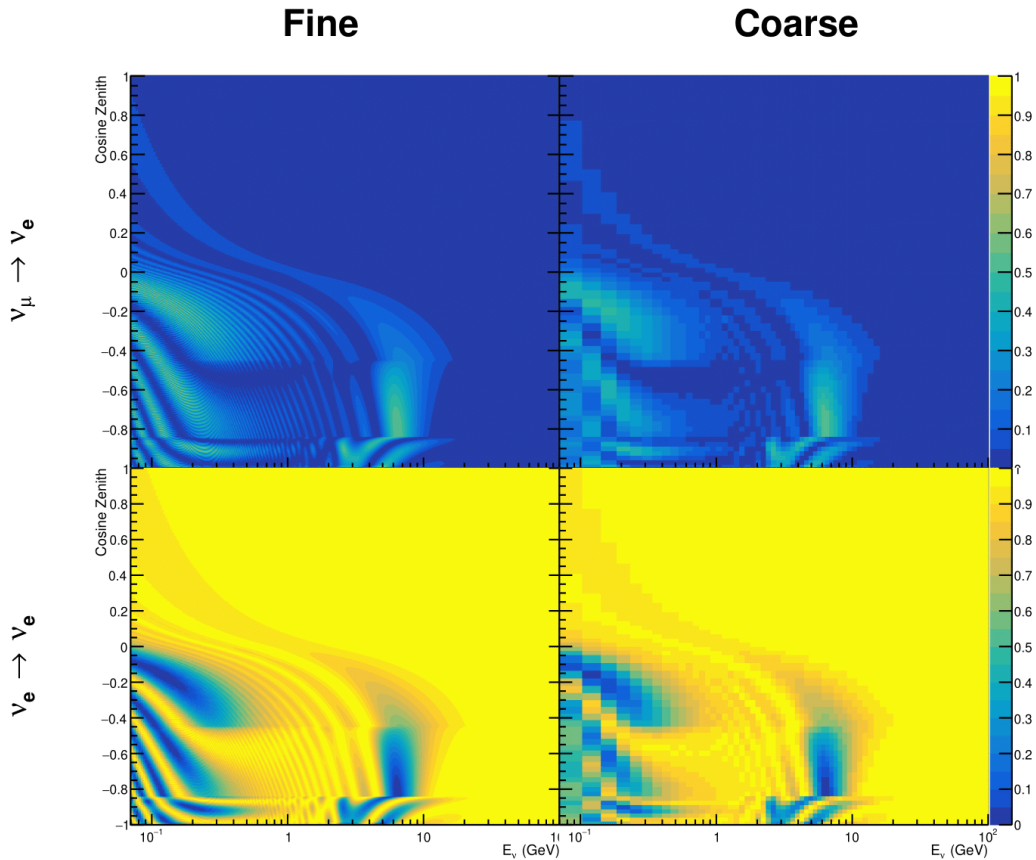


**Figure 4.10:** The oscillation probability,  $P(\nu_\mu \rightarrow \nu_e)$  (top row) and  $P(\nu_e \rightarrow \nu_e)$  (bottom row), given as a function of neutrino energy and zenith angle. The left column gives the “fine” binning used to calculate the oscillation probabilities and the right column illustrates the “coarse” binning used to reweight the MC events. The fine binning choice is given with  $N = 10$ , which was determined to be below threshold from Figure 4.8 and Figure 4.9.

## <sup>1417</sup> 4.3 Calculation Engine

<sup>1418</sup> As previously discussed in section 4.2, the calculation of oscillation probabilities is per-  
<sup>1419</sup> formed at run-time due to utilising continuous oscillation parameters. Consequently,  
<sup>1420</sup> the time per calculation is crucial for fit performance. The fitting framework used for  
<sup>1421</sup> this analysis was developed with ProbGPU [133]. This is a GPU-only implementation  
<sup>1422</sup> of the prob3 engine [134]. It is primarily designed for neutrino propagation in a beam  
<sup>1423</sup> experiment (single layer of constant density) with the atmospheric propagation code  
<sup>1424</sup> not being used prior to the analysis in this thesis.

<sup>1425</sup> Another engine, CUDAProb3 [135], has been implemented within the fitting frame-  
<sup>1426</sup> work used within this analysis. It has been specifically optimised for atmospheric  
<sup>1427</sup> neutrino oscillation calculation so unfortunately does not contain the code to replace  
<sup>1428</sup> the beam oscillation calculation. The engine is utilises object orientated techniques as  
<sup>1429</sup> compared to the functional implementation of ProbGPU. This allows the energy and  
<sup>1430</sup> cosine zenith arrays to be kept on GPU memory, rather than having to load these  
<sup>1431</sup> arrays onto GPU memory for each calculation. General memory interfacing is one  
<sup>1432</sup> of the slowest tasks which GPUs can do, so being able to eliminate this significantly  
<sup>1433</sup> reduces the time required for calculation. This can be seen in Figure 4.11, where  
<sup>1434</sup> the GPU implementaton of CUDAProb3 is approximately three times faster than the  
<sup>1435</sup> ProbGPU engine.

<sup>1436</sup> Another significant advantage of CUDAProb3 is that it contains a CPU multithreaded  
<sup>1437</sup> implementation which is not possible with the ProbGPU or prob3 engines. This elimi-  
<sup>1438</sup> nates the requirement for GPU resources when submitting jobs to batch systems. As  
<sup>1439</sup> illustrated in Figure 4.11, the calculation speed depends on the number of available  
<sup>1440</sup> threads. Using 8 threads (which is typical of the batch systems being used) is ap-  
<sup>1441</sup> proximately twice as slow as the ProbGPU engine implementation, but would allow

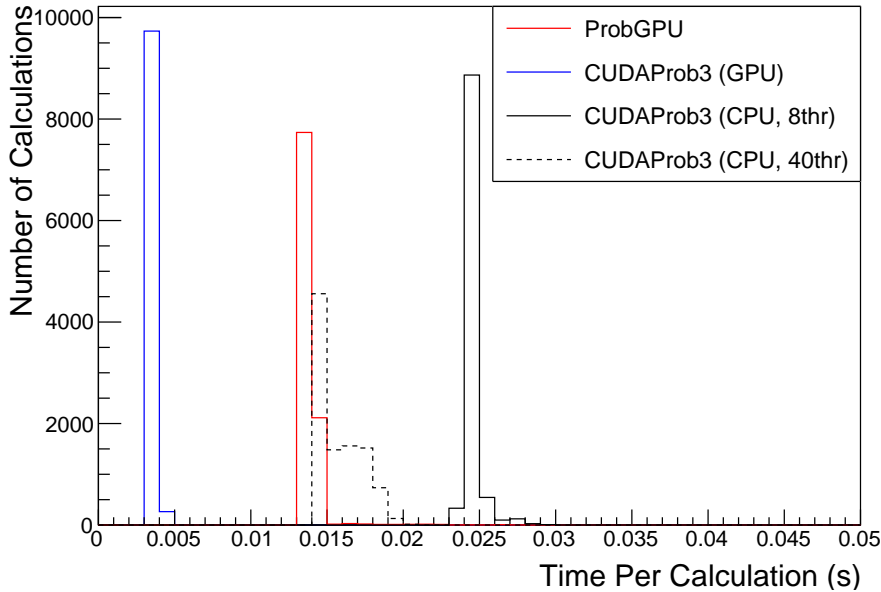


**Figure 4.11:** The calculation time taken to both calculate the oscillation probabilities and fill the “coarse” oscillograms, following the technique given in section 4.2, for the CUDAProb3 and ProbGPU (Red) calculation engines. CUDAProb3 has both a GPU (Blue) and CPU (Black) implementation, where the CPU implementation is multithreaded. Therefore, 8-threads (solid) and 40-threads (dashed) configurations have been used. Prob3, which is a CPU single-thread implementation has a mean step time of 1.142s.

<sup>1442</sup> the fitting framework to be run on many more resources. This fact is utilised for any  
<sup>1443</sup> SK-only fits but GPU resources are required for any fits which include beam samples  
<sup>1444</sup> due to the ProbGPU requirement.

## <sup>1445</sup> 4.4 Matter Density Profile

<sup>1446</sup> For an experiment observing atmospheric neutrinos propagating through the Earth,  
<sup>1447</sup> such as the studies presented in this thesis, a model of the Earth’s density and layering  
<sup>1448</sup> is required. The model used within this analysis is the Preliminary Reference Earth  
<sup>1449</sup> Model (PREM) [136]. This model provides piecewise cubic polynomials as a function  
<sup>1450</sup> of radius which results in the density profile illustrated in Figure 4.12. As will be  
<sup>1451</sup> discussed in section 4.5, the propagator used within the calculation engine requires

<sup>1452</sup> constant density layers. To follow the official SK-only analysis [132], the average  
<sup>1453</sup> density of each layer has been taken from the PREM model. Table 4.2 documents the  
<sup>1454</sup> density and radii of the layers used within this approximation.

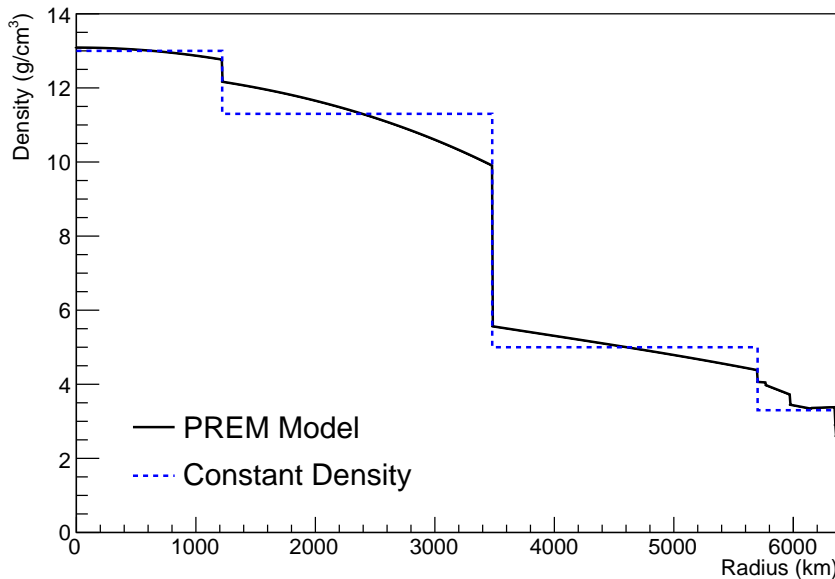


**Figure 4.12:** The density of the Earth given as a function of the radius, as given by the PREM model (Black) and the constant density four-layer approximation (Blue), as used in the official SK-only analysis.

Layer	Outer Radius [km]	Density [g/cm <sup>3</sup> ]	Chemical composition (Z/A)
Inner Core	1220	13	$0.468 \pm 0.029$
Outer Core	3480	11.3	$0.468 \pm 0.029$
Lower Mantle	5701	5.0	0.496
Transition Zone	6371	3.3	0.496

**Table 4.2:** Description of the four layers of the Earth invoked within the average constant density approximation of the PREM model [136].

<sup>1455</sup> The density measurements provided in the PREM model are provided in terms  
<sup>1456</sup> of mass density, whereas neutrino oscillations are sensitive to the electron number  
<sup>1457</sup> density. This value can be computed as the product of the chemical composition, or  
<sup>1458</sup> the Z/A value, and mass density of each layer. Currently, the only way to calculate  
<sup>1459</sup> this value for layers close to the Earth's core is through neutrino oscillations. The

<sup>1460</sup> chemical composition of the upper layers of the Earth's Mantle and Transition zone is  
<sup>1461</sup> well known due to it being predominantly pyrolite which has a chemical composition  
<sup>1462</sup> value of 0.496 [137]. The components of the Earth's core region is less well known.  
<sup>1463</sup> Consequently the chemical composition dial for the core layers is set to a value of 0.468  
<sup>1464</sup> [138]. This value is assigned a Gaussian error with standard deviation equivalent to  
<sup>1465</sup> the difference of chemical composition in core and mantle layers. Figure 4.13 illustrates  
<sup>1466</sup> the effect of moving from the  $Z/A = 0.5$  method which is used in the official SK-only  
<sup>1467</sup> analysis [132] to more precise values recorded by other neutrino experiments.

<sup>1468</sup> The beam oscillation probability in this thesis uses a baseline of 295km, density  
<sup>1469</sup>  $2.6\text{g/cm}^3$  [139], and chemical composition 0.5 as is done by the official T2K-only  
<sup>1470</sup> analysis.

<sup>1471</sup> Whilst the propagator requires a fixed density layer model of the Earth, the density  
<sup>1472</sup> only has to be fixed for a specific neutrino energy  $\times \cos(\theta_Z)$  bin in a given layer (I.e.  
<sup>1473</sup> set of values at which to calculate the oscillation probability). As the density is a  
<sup>1474</sup> function of radius, which is a function of the direction in which a neutrino propagates,  
<sup>1475</sup> a better approximation of the PREM model can be made if a  $\cos(\theta_Z)$ -specific density is  
<sup>1476</sup> calculated.

<sup>1477</sup> To achieve this, the average density,  $\langle \rho \rangle_i$ , in the  $i^{th}$  layer, is calculated as the density,  
<sup>1478</sup>  $\rho$ , integrated over the track a given  $\cos(\theta_Z)$ ,

$$\langle \rho \rangle_i = \frac{1}{t_{i+1} - t_i} \int_{t_i}^{t_{i+1}} \rho(t) dt \quad (4.5)$$

<sup>1479</sup> where  $t_i$  are the intersection points between each layer and  $t$  is the path length of  
<sup>1480</sup> the trajectory across the layer which is dependent upon  $\cos(\theta_Z)$ .

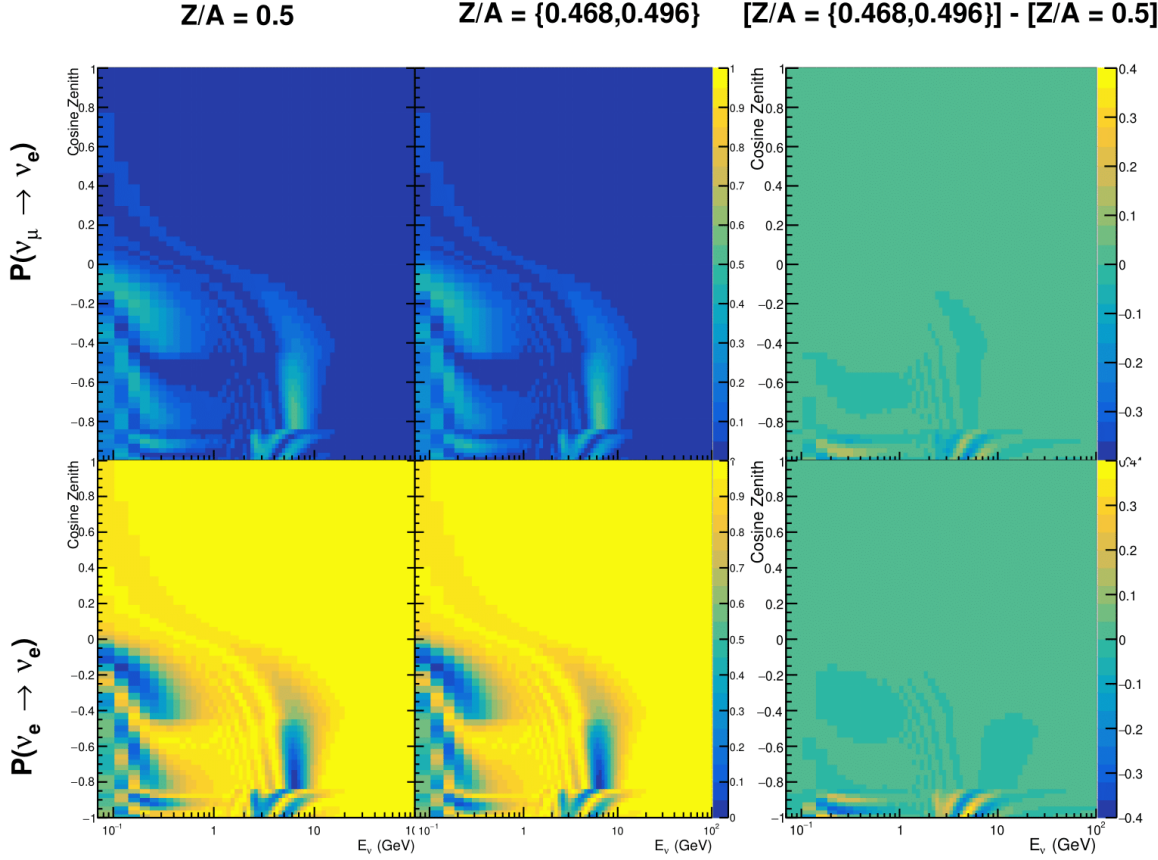


**Figure 4.13:** The oscillation probability,  $P(\nu_\mu \rightarrow \nu_e)$  (top row) and  $P(\nu_e \rightarrow \nu_\mu)$  (bottom row), given as a function of neutrino energy and zenith angle. The left column gives probabilities where the constant  $Z/A = 0.5$  approximation which is used in the official SK-only analysis. The middle column gives the probabilities where the more accurate  $Z/A = [0.468, 0.498]$  values as given in Table 4.2. The right column illustrates the difference in oscillation probability between the two different techniques.

The oscillation probability calculation speed is approximately linear in the number of layers invoked within the Earth model. Therefore a four layer model is still utilized with the only difference to the above example being that the four layer model used for each value of  $\cos(\theta_Z)$  is different. Following the method outlined in [140], a four layer piecewise quadratic polynomial is fit to the PREM model for the four layers defined in Table 4.2. This fit was not performed by the author of the thesis and is documented in [141]. The co-efficients of the quadratic fit to each layer is given in Table 4.3 with

<sup>1488</sup> the final distribution illustrated in Figure 4.14. The quadratic approximation is clearly  
<sup>1489</sup> much closer to the PREM model as compared to the constant density approximation.

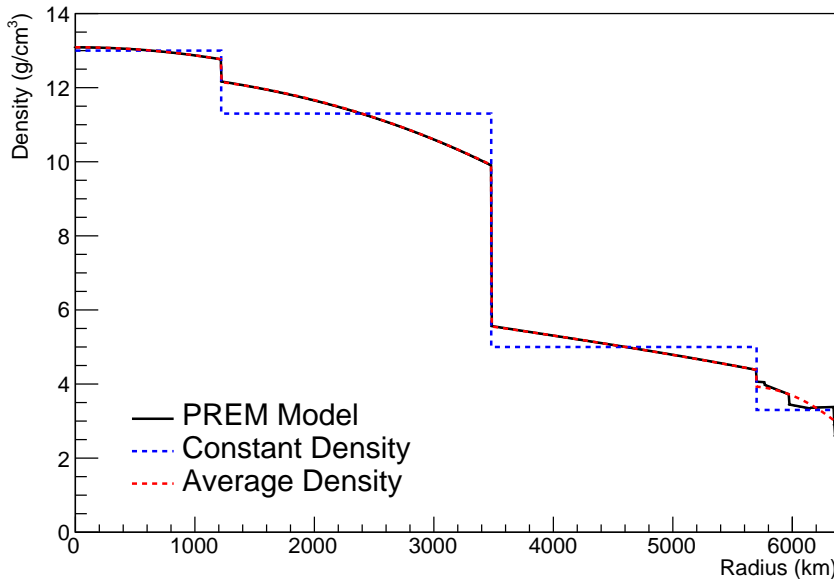


**Figure 4.14:** The density of the Earth given as a function of the radius, as given by the PREM model (Black), the constant density four-layer approximation (Blue), as used in the official SK-only analysis, and the quadratic approximation of the PREM model (Red).

Layer	Outer Radius [km]	Density [g/cm <sup>3</sup> ]
Inner Core	1220	$13.09 - 8.84x^2$
Outer Core	3480	$12.31 + 1.09x - 10.02x^2$
Lower Mantle	5701	$6.78 - 1.56x - 1.25x^2$
Transition Zone	6371	$-50.42 + 123.33x - 69.95x^2$

**Table 4.3:** The quadratic polynomial fits to the PREM model for four assumed layers of the PREM model. The fit to calculate the coefficients is given in [141], where  $x = R/R_{Earth}$ .

<sup>1490</sup> The effect of using the average density per  $\cos(\theta_Z)$  model is highlighted in Fig-  
<sup>1491</sup> ure 4.15. The slight discontinuity in the oscillation probability around  $\cos(\theta_Z) \sim -0.45$   
<sup>1492</sup> in the fixed density model, which is due to the transition to mantle layer boundary, has  
<sup>1493</sup> been reduced. This is expected as the difference in the density across this boundary is  
<sup>1494</sup> significantly smaller in the average density model as compared to the constant density

model. Whilst the difference in density across the other layer transitions is reduced, there is still a significant difference. This means the discontinuities in the oscillation probabilities remain, but are significantly reduced. However, as the average density approximation matches the PREM model well in this region, these discontinuities are due to the Earth model rather than an artifact of the oscillation calculation.

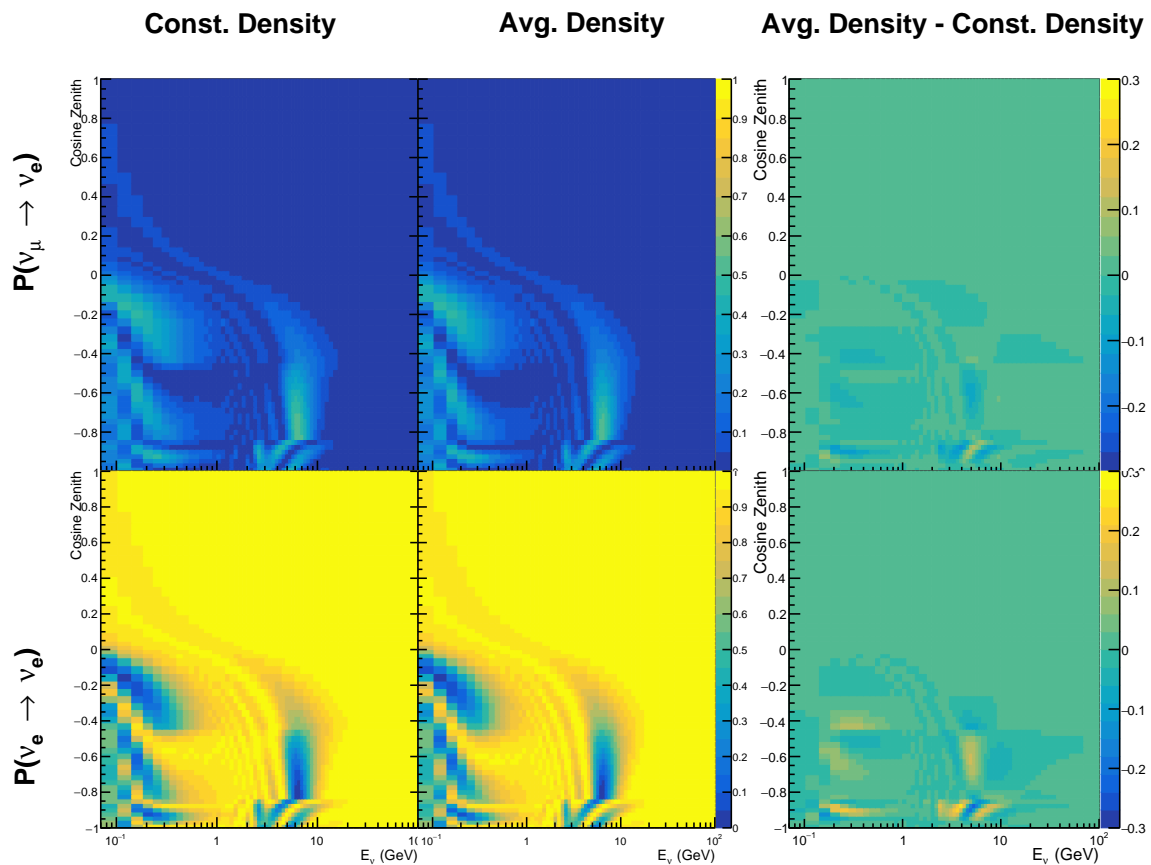


**Figure 4.15:** The oscillation probability,  $P(\nu_\mu \rightarrow \nu_e)$  (top row) and  $P(\nu_e \rightarrow \nu_e)$  (bottom row), given as a function of neutrino energy and zenith angle. The left column gives probabilities where the four-layer constant density approximation is used. The middle column gives the probabilities where the density is integrated over the trajectory, using the quadratic PREM approximation, for each  $\cos(\theta_Z)$  is used. The right column illustrates the difference in oscillation probability between the two different techniques.

## 1500 4.5 Production Height Averaging

1501 As discussed in section 4.1, the height at which the cosmic ray flux interacts in the  
1502 atmosphere is not known on an event-by-event basis. The production height can  
1503 vary from the Earth's surface to 50km above that. The SK-only analysis methodol-  
1504 ogy (described in section 4.2) for including the uncertainty on the production height  
1505 is to include variations from the Honda model when pre-calculating the oscillation  
1506 probabilities prior to the fit. This technique is not possible for this analysis which  
1507 uses continuous oscillation parameters that can not be known prior to the fit. Conse-  
1508 quently, an analytical averaging technique was developed in [141]. The author of this  
1509 thesis was not responsible for the derivation of the technique but has performed the  
1510 implementation and validation of the technique for this analysis alone.

1511 The oscillation probability used within this analysis is based on [142]. The neutrino  
1512 wavefunction in the vacuum Hamiltonian evolves in each layer of constant matter  
1513 density via

$$i \frac{d\psi_j(t)}{dt} = \frac{m_j^2}{2E_\nu} \psi_j(t) - \sum_k \sqrt{2} G_F N_e U_{ej} U_{ke}^\dagger \psi_k(t), \quad (4.6)$$

1514 where  $m_j^2$  is the square of the  $j^{th}$  vacuum eigenstate mass,  $E_\nu$  is the neutrino energy,  
1515  $G_F$  is Fermi's constant,  $N_e$  is the electron number density and  $U$  is the PMNS matrix.  
1516  $N_e \rightarrow -N_e$  and  $\delta_{CP} \rightarrow -\delta_{CP}$  for antineutrino propagation.

1517 Using the 20 production heights per MC neutrino event, provided as 5% percentiles  
1518 from the Honda flux model, a production height distribution  $p_j(h|E_\nu, \cos \theta_Z)$  is built  
1519 for each neutrino flavour  $j = \nu_e, \bar{\nu}_e, \nu_\mu, \bar{\nu}_\mu$ . In practice, a histogram is filled with 20  
1520 evenly spaced bins in production height  $h$  between 0 and 50km. The neutrino energy

and cosine zenith binning is the same as that provided in section 4.2. The average production height,  $\bar{h} = \int dh \frac{1}{4} \sum_j p_j(h|E_\nu, \cos(\theta_Z))$ , is calculated. The production height binning of this histogram is then translated into  $\delta t(h) = t(z, \bar{h}) - t(z, h)$ , where  $t(z, h)$  is the distance travelled along the trajectory.

For the  $i^{th}$  traversed layer, the transition amplitude,  $D_i(t_{i+1}, t_i)$ , is computed. The time ordered product of these is then used as the overall transition amplitude via

$$A(t_{n+1}, t_0) = D_n(t_{n+1}, t_n) \dots D_1(t_2, t_1) D_0(t_1, t_0), \quad (4.7)$$

where,

$$\begin{aligned} D_n(t_{n+1}, t_n) &= \exp[-iH_n(t_{n+1} - t_n)] \\ &= \sum_{k=1}^3 C_k \exp[ia_k \delta t] \end{aligned} \quad (4.8)$$

is expressed as a diagonalised time-dependent solution to the schrodinger equation. The  $0^{th}$  layer is the propagation through the atmosphere and is the only term which depends on the production height. Using the substitution  $t_0 = t(\bar{h}) - \delta t(h)$ , it can be shown that

$$D_0(t_1, t_0) = D_0(t_1, \bar{h}) D_0(\delta t). \quad (4.9)$$

Thus Equation 4.7 becomes

$$\begin{aligned}
A(t_{n+1}, t_0) &= D_n(t_{n+1}, t_n) \dots D_1(t_2, t_1) D_0(t_1, \bar{h}) D(\delta t) \\
&= A(t_{n+1}, \bar{h}) \sum_{k=1}^3 C_k \exp[i a_k \delta t], \\
&= \sum_{k=1}^3 B_k \exp[i a_k \delta t].
\end{aligned} \tag{4.10}$$

<sub>1533</sub> The oscillation probability, averaged over production height is calculated as

$$\begin{aligned}
\bar{P}(\nu_j \rightarrow \nu_i) &= \int d(\delta t) p_j(\delta t | E_\nu, \cos \theta_Z) P(\nu_j \rightarrow \nu_i) \\
&= \int d(\delta t) p_j(\delta t | E_\nu, \cos \theta_Z) A(t_{n+1}, t_0) A^*(t_{n+1}, t_0) \\
&= \sum_{km} (B_k)_{ij} (B_m)_{ij}^* \int d(\delta t) p_j(\delta t | E_\nu, \cos \theta_Z) \exp[i(a_k - a_m)\delta t]
\end{aligned} \tag{4.11}$$

<sub>1534</sub> In practice, implementation in CUDAProb3 [135] is relatively straight forward as  
<sub>1535</sub> the majority of these terms are already calculated in the standard oscillation calculation.  
<sub>1536</sub> Figure 4.16 illustrates the results of the production height averaging. As expected,  
<sub>1537</sub> the main effect is observed in the low-energy downward-going and horizontal-going  
<sub>1538</sub> events. Upward-going events have to travel the radius of the Earth,  $R_E = 6371\text{km}$ ,  
<sub>1539</sub> where the production height uncertainty is a small fraction of the total path length.

<sub>1540</sub>

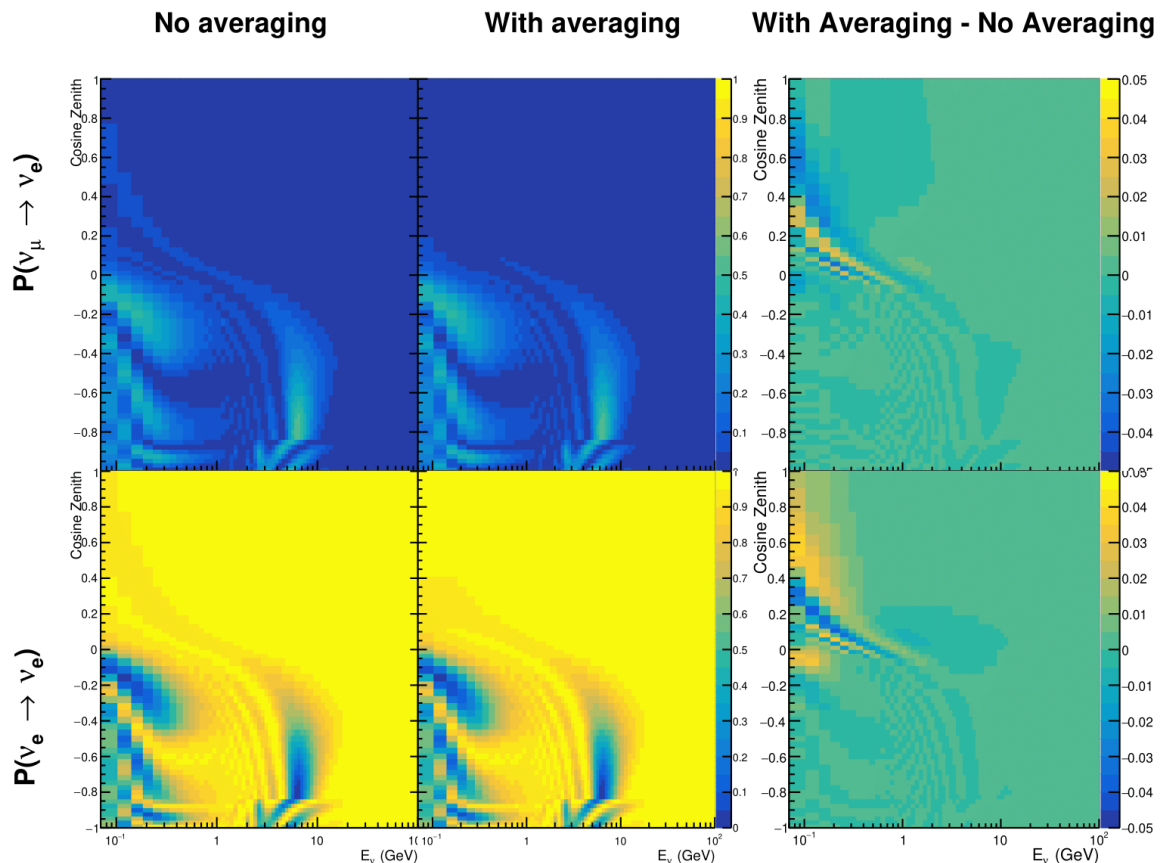


**Figure 4.16:** The oscillation probability,  $P(\nu_\mu \rightarrow \nu_e)$  (top row) and  $P(\nu_e \rightarrow \nu_\mu)$  (bottom row), given as a function of neutrino energy and zenith angle. The left column gives probabilities where a fixed production height of 25km is used. The middle column gives the probabilities where the production height is analytically averaged. The right column illustrates the difference in oscillation probability between the two different techniques.

<sub>1541</sub> **Bibliography**

- <sub>1542</sub> [1] J. Chadwick, Verhandl. Dtsc. Phys. Ges. **16**, 383 (1914).
- <sub>1543</sub> [2] C. D. Ellis and W. A. Wooster, Proc. R. Soc. Lond. A Math. Phys. Sci. **117**, 109  
<sub>1544</sub> (1927).
- <sub>1545</sub> [3] W. Pauli, Phys. Today **31N9**, 27 (1978).
- <sub>1546</sub> [4] E. Fermi, Z. Phys. **88**, 161 (1934).
- <sub>1547</sub> [5] F. Reines and C. L. Cowan, Phys. Rev. **92**, 830 (1953).
- <sub>1548</sub> [6] C. L. Cowan, F. Reines, F. B. Harrison, H. W. Kruse, and A. D. McGuire, Science  
<sub>1549</sub> **124**, 103 (1956), <http://science.sciencemag.org/content/124/3212/103.full.pdf>.
- <sub>1550</sub> [7] G. Danby *et al.*, Phys. Rev. Lett. **9**, 36 (1962).
- <sub>1551</sub> [8] K. Kodama *et al.*, Physics Letters B **504**, 218 (2001).
- <sub>1552</sub> [9] LSND, A. Aguilar-Arevalo *et al.*, Phys. Rev. **D64**, 112007 (2001), hep-ex/0104049.
- <sub>1553</sub> [10] MiniBooNE Collaboration, A. A. Aguilar-Arevalo *et al.*, Phys. Rev. Lett. **110**,  
<sub>1554</sub> 161801 (2013).
- <sub>1555</sub> [11] and P. A. R. Ade *et al.*, Astronomy and Astrophysics **594**, A13 (2016).
- <sub>1556</sub> [12] B. Pontecorvo, Sov. Phys. JETP **26**, 984 (1968), [Zh. Eksp. Teor. Fiz. 53, 1717 (1967)].
- <sub>1557</sub> [13] B. Pontecorvo, Sov. Phys. JETP **7**, 172 (1958), [Zh. Eksp. Teor. Fiz. 34, 247 (1957)].
- <sub>1558</sub> [14] M. Kobayashi and T. Maskawa, Progress of Theoretical Physics **49**, 652 (1973).
- <sub>1559</sub> [15] N. Cabibbo, Phys. Rev. Lett. **10**, 531 (1963).
- <sub>1560</sub> [16] A. Y. Smirnov, (2003).
- <sub>1561</sub> [17] S. Mikheyev and A. Smirnov, Soviet Journal of Nuclear Physics **42**, 913 (1985).
- <sub>1562</sub> [18] L. Wolfenstein, Phys. Rev. D **17**, 2369 (1978).
- <sub>1563</sub> [19] The Super-Kamiokande Collaboration, Y. Ashie *et al.*, Phys. Rev. Lett. **93**, 101801  
<sub>1564</sub> (2004).
- <sub>1565</sub> [20] SNO Collaboration, Q. R. Ahmad *et al.*, Phys. Rev. Lett. **89**, 011301 (2002).

- 1566 [21] 2015 Nobel prize in Physics as listed by Nobelprize.org, [https://www.](https://www.nobelprize.org/nobel_prizes/physics/laureates/2015/)  
1567 nobelprize.org/nobel\_prizes/physics/laureates/2015/, Accessed: 22-06-  
1568 2022.
- 1569 [22] J. A. Formaggio and G. P. Zeller, Rev. Mod. Phys. **84**, 1307 (2012), 1305.7513.
- 1570 [23] A. Bellerive, Int. J. Mod. Phys. A **19**, 1167 (2004).
- 1571 [24] R. Davis, D. S. Harmer, and K. C. Hoffman, Phys. Rev. Lett. **20**, 1205 (1968).
- 1572 [25] N. Vinyoles *et al.*, Astrophys. J. **835**, 202 (2017).
- 1573 [26] V. Gribov and B. Pontecorvo, Phys. Lett. B **28**, 493 (1969).
- 1574 [27] K. S. Hirata *et al.*, Phys. Rev. Lett. **63**, 16 (1989).
- 1575 [28] W. Hampel *et al.*, Phys. Lett. B **447**, 127 (1999).
- 1576 [29] SAGE Collaboration, J. N. Abdurashitov *et al.*, Phys. Rev. C **60**, 055801 (1999).
- 1577 [30] Q. R. Ahmad *et al.*, Phys. Rev. Lett. **89** (2002).
- 1578 [31] Borexino Collaboration, Nature **562**, 505 (2018).
- 1579 [32] B. Aharmim *et al.*, Astrophys. J. **653**, 1545 (2006).
- 1580 [33] M. Agostini *et al.*, (2020).
- 1581 [34] S. Andringa *et al.*, Adv. High Energy Phys. **2016**, 1 (2016).
- 1582 [35] J. F. Beacom *et al.*, Chin. phys. C **41**, 023002 (2017).
- 1583 [36] F. An *et al.*, J. Phys. G Nucl. Part. Phys. **43**, 030401 (2016).
- 1584 [37] J. Aalbers *et al.*, (2020), 2006.03114.
- 1585 [38] T. K. Gaisser and M. Honda, (2002).
- 1586 [39] G. D. Barr, T. K. Gaisser, P. Lipari, S. Robbins, and T. Stanev, Physical Review D  
1587 **70** (2004).
- 1588 [40] M. Honda, T. Kajita, K. Kasahara, S. Midorikawa, and T. Sanuki, Physical Review  
1589 D **75** (2007).
- 1590 [41] M. Honda, T. Kajita, K. Kasahara, and S. Midorikawa, Phys. Rev. D **70**, 043008  
1591 (2004).

- 1592 [42] A. Fasso, A. Ferrari, P. R. Sala, and J. Ranft, (2001).
- 1593 [43] Y. Ashie *et al.*, Physical Review D **71** (2005).
- 1594 [44] F. Reines *et al.*, Phys. Rev. Lett. **15**, 429 (1965).
- 1595 [45] D. Casper *et al.*, Phys. Rev. Lett. **66**, 2561 (1991).
- 1596 [46] K. S. Hirata *et al.*, Phys. Lett. B **280**, 146 (1992).
- 1597 [47] Z. Li *et al.*, Physical Review D **98** (2018).
- 1598 [48] Kamiokande Collaboration *et al.*, (2017).
- 1599 [49] T2K Collaboration, Nature **580**, 339 (2020).
- 1600 [50] M. A. Acero *et al.*, Phys. Rev. Lett. **123**, 151803 (2019).
- 1601 [51] M. G. Aartsen *et al.*, Phys. Rev. Lett. **120** (2018).
- 1602 [52] P. Adamson *et al.*, Phys. Rev. Lett. **112** (2014).
- 1603 [53] M. S. Athar *et al.*, Progress in Particle and Nuclear Physics **124**, 103947 (2022).
- 1604 [54] G. Danby *et al.*, Phys. Rev. Lett. **9**, 36 (1962).
- 1605 [55] K. Abe *et al.*, Physical Review D **87** (2013).
- 1606 [56] MINOS Collaboration, D. G. Michael *et al.*, Phys. Rev. Lett. **97**, 191801 (2006).
- 1607 [57] G. Danby *et al.*, Phys. Rev. Lett. **9**, 36 (1962).
- 1608 [58] NOvA Collaboration, M. A. Acero *et al.*, Phys. Rev. Lett. **123**, 151803 (2019).
- 1609 [59] B. Abi, R. Acciarri, M. A. Acero, and G. e. a. Adamov, Eur. Phys. J. C Part. Fields **80** (2020).
- 1610 [60] Hyper-Kamiokande Proto-Collaboration *et al.*, Prog. Theor. Exp. Phys. **2015**, 53C02 (2015).
- 1611 [61] C. Blanco, D. Hooper, and P. Machado, Physical Review D **101** (2020).
- 1612 [62] MicroBooNE Collaboration *et al.*, Search for an Excess of Electron Neutrino Interactions in MicroBooNE Using Multiple Final State Topologies, 2021.
- 1613 [63] KARMEN Collaboration, B. Armbruster *et al.*, Phys. Rev. D **65**, 112001 (2002).
- 1614 [64] S.-B. Kim, T. Lasserre, and Y. Wang, Adv. High Energy Phys. **2013**, 1 (2013).

- [65] M. Sajjad Athar *et al.*, Prog. Part. Nucl. Phys. **124**, 103947 (2022), 2111.07586.
- [66] K. Abe *et al.*, Nucl. Instrum. Methods Phys. Res. A **1027**, 166248 (2022).
- [67] F. P. An *et al.*, Phys. Rev. Lett. **108**, 171803 (2012).
- [68] RENO Collaboration, J. K. Ahn *et al.*, Phys. Rev. Lett. **108**, 191802 (2012).
- [69] Double Chooz Collaboration, Y. Abe *et al.*, Phys. Rev. Lett. **108**, 131801 (2012).
- [70] J. Collaboration *et al.*, TAO Conceptual Design Report: A Precision Measurement of the Reactor Antineutrino Spectrum with Sub-percent Energy Resolution, 2020, 2005.08745.
- [71] for the RENO Collaboration, New results from RENO and the 5 MeV excess, AIP Publishing LLC, 2015.
- [72] Y. Abe *et al.*, Journal of High Energy Physics **2014** (2014).
- [73] Daya Bay Collaboration, D. Adey *et al.*, Phys. Rev. Lett. **123**, 111801 (2019).
- [74] M. P. Decowski, Nucl. Phys. B. **908**, 52 (2016).
- [75] The KamLAND Collaboration, A. Gando *et al.*, Phys. Rev. D **83**, 052002 (2011).
- [76] Y. Fukuda *et al.*, Phys. Rev. Lett. **81**, 1562 (1998).
- [77] K. Abe *et al.*, Nuclear Instruments and Methods in Physics Research Section A: Accelerators, Spectrometers, Detectors and Associated Equipment **737**, 253 (2014).
- [78] S. Fukuda *et al.*, Nucl. Instrum. Methods Phys. Res. A **501**, 418 (2003).
- [79] Y. Itow *et al.*, (2001).
- [80] M. Jiang *et al.*, Prog. Theor. Exp. Phys. **2019** (2019).
- [81] S. Fukuda *et al.*, Nuclear Instruments and Methods in Physics Research Section A: Accelerators, Spectrometers, Detectors and Associated Equipment **501**, 418 (2003), <http://www.sciencedirect.com/science/article/pii/S016890020300425X>.
- [82] Y. Nakano *et al.*, Nucl. Instrum. Methods Phys. Res. A **977**, 164297 (2020).
- [83] Hamamatsu, Hamamatsu Photonics Photomultiplier Tubes Handbook.
- [84] K. Abe *et al.*, Nucl. Instrum. Methods Phys. Res. A **1027**, 166248 (2022).

- [85] J. F. Beacom and M. R. Vagins, Phys. Rev. Lett. **93**, 171101 (2004).
- [86] L. Marti *et al.*, Nucl. Instrum. Methods Phys. Res. A **959**, 163549 (2020).
- [87] L. Marti *et al.*, (2019).
- [88] G. Carminati, Phys. Procedia **61**, 666 (2015).
- [89] T. Tanimori *et al.*, IEEE Transactions on Nuclear Science **36**, 497 (1989).
- [90] Super-Kamiokande Collaboration, J. Hosaka *et al.*, Phys. Rev. D **73**, 112001 (2006).
- [91] H. Nishino *et al.*, Nucl. Instrum. Methods Phys. Res. A **610**, 710 (2009).
- [92] S. Yamada *et al.*, IEEE Transactions on Nuclear Science **57**, 428 (2010).
- [93] S. Yamada, Y. Hayato, Y. Obayashi, and M. Shiozawa, New online system without hardware trigger for the Super-Kamiokande experiment, in *2007 IEEE Nuclear Science Symposium Conference Record*, IEEE, 2007.
- [94] P. A. Čerenkov, Phys. Rev. **52**, 378 (1937).
- [95] I. Frank and I. Tamm, Coherent visible radiation of fast electrons passing through matter, in *Selected Papers*, pp. 29–35, Springer Berlin Heidelberg, Berlin, Heidelberg, 1991.
- [96] The T2K Collaboration, KEK Proposal (2001), <http://neutrino.kek.jp/jhfnu/loi/loi.v2.030528.pdf>.
- [97] Y. Itow *et al.*, (2001), hep-ex/0106019.
- [98] The K2K Collaboration and S. H. Ahn, (2001), hep-ex/0103001.
- [99] The T2K Collaboration, KEK Proposal (2006), [http://j-parc.jp/researcher/Hadron/en/pac\\_0606/pdf/p11-Nishikawa.pdf](http://j-parc.jp/researcher/Hadron/en/pac_0606/pdf/p11-Nishikawa.pdf).
- [100] T2K Collaboration, K. Abe *et al.*, Phys. Rev. Lett. **112**, 061802 (2014), <https://link.aps.org/doi/10.1103/PhysRevLett.112.061802>.
- [101] NINJA Collaboration, T. Fukuda *et al.*, Proposal for precise measurement of neutrino-water cross-section in NINJA physics run, Proposal for J-PARC and KEK, 2017.
- [102] T. Ovsiannikova *et al.*, Physics of Particles and Nuclei **48**, 1014 (2017),

- 1673        <https://doi.org/10.1134/S1063779617060478>.
- 1674 [103] M. Antonova *et al.*, Journal of Instrumentation **12**, C07028 (2017),  
1675        <http://stacks.iop.org/1748-0221/12/i=07/a=C07028>.
- 1676 [104] The T2K Collaboration, K. Abe *et al.*, Phys. Rev. D **102**, 012007 (2020).
- 1677 [105] K. Abe *et al.*, Progress of Theoretical and Experimental Physics **2021** (2021).
- 1678 [106] The T2K Collaboration, K. Abe *et al.*, Nuclear Instruments  
1679        and Methods in Physics Research Section A: Accelerators, Spec-  
1680        trometers, Detectors and Associated Equipment **659**, 106 (2011),  
1681        <http://www.sciencedirect.com/science/article/pii/S0168900211011910>.
- 1682 [107] K. Matsuoka *et al.*, Nuclear Instruments and Methods in Physics Research Section  
1683        A: Accelerators, Spectrometers, Detectors and Associated Equipment **624**, 591  
1684        (2010), <http://www.sciencedirect.com/science/article/pii/S016890021002098X>.
- 1685 [108] K. Abe *et al.*, Phys. Rev. D. **103** (2021).
- 1686 [109] T. Vladisavljevic, *Predicting the T2K neutrino flux and measuring oscillation parame-*  
1687        *ters* Springer theses, 1 ed. (Springer Nature, Cham, Switzerland, 2020).
- 1688 [110] D. Beavis, A. Carroll, and I. Chiang, (1995).
- 1689 [111] P.-A. Amaudruz *et al.*, Nuclear Instruments and Methods in Physics Research  
1690        Section A: Accelerators, Spectrometers, Detectors and Associated Equipment  
1691        **696**, 1 (2012).
- 1692 [112] N. Abgrall *et al.*, Nuclear Instruments and Methods in Physics Research Section  
1693        A: Accelerators, Spectrometers, Detectors and Associated Equipment **637**, 25  
1694        (2011).
- 1695 [113] S. Assylbekov *et al.*, Nuclear Instruments and Methods in Physics Research  
1696        Section A: Accelerators, Spectrometers, Detectors and Associated Equipment  
1697        **686**, 48 (2012).
- 1698 [114] D. Allan *et al.*, Journal of Instrumentation **8**, P10019 (2013).
- 1699 [115] F. Vannucci, Advances in High Energy Physics **2014**, 1 (2014).
- 1700 [116] UA1 magnet sets off for a second new life, 2022.
- 1701 [117] S. Aoki *et al.*, Nuclear Instruments and Methods in Physics Research Section

- 1702        A: Accelerators, Spectrometers, Detectors and Associated Equipment **698**, 135  
1703        (2013).
- 1704        [118] M. Yokoyama *et al.*, Nuclear Instruments and Methods in Physics Research  
1705        Section A: Accelerators, Spectrometers, Detectors and Associated Equipment  
1706        **622**, 567 (2010).
- 1707        [119] K. Suzuki *et al.*, Progress of Theoretical and Experimental Physics **2015**, 53C01  
1708        (2015).
- 1709        [120] S. Brooks, A. Gelman, G. L. Jones, and X.-L. Meng, *Handbook of Markov Chain  
1710        Monte Carlo* (CRC Press, 2011).
- 1711        [121] W. R. Gilks, S. Richardson, and D. J. Spiegelhalter, *Markov Chain Monte Carlo in  
1712        Practice* (Chapman & Hall/CRC Interdisciplinary Statistics, 1995).
- 1713        [122] C. Wret, *Minimising systematic uncertainties in the T2K experiment using near-  
1714        detector and external data*, PhD thesis, Imperial College London, 2018.
- 1715        [123] K. E. Duffy, *Measurement of the Neutrino Oscillation Parameters  $\sin^2 \theta_{23}$ ,  $\Delta m_{32}^2$ ,  
1716         $\sin^2 \theta_{13}$ , and  $\delta_{CP}$  in Neutrino and Antineutrino Oscillation at T2K*, PhD thesis, Oriel  
1717        College, University of Oxford, 2016.
- 1718        [124] T. Bayes, Rev., Phil. Trans. Roy. Soc. Lond. **53**, 370 (1764).
- 1719        [125] N. Metropolis, A. W. Rosenbluth, M. N. Rosenbluth, A. H. Teller, and E. Teller,  
1720        Journal of Chemical Physics **21** (1970).
- 1721        [126] W. K. Hastings, Biometrika **57** (1970).
- 1722        [127] J. Dunkley, M. Bucher, P. G. Ferreira, K. Moodley, and C. Skordis, Mon. Not. R.  
1723        Astron. Soc. **356**, 925 (2005).
- 1724        [128] Particle Data Group *et al.*, Prog. Theor. Exp. Phys. **2020** (2020).
- 1725        [129] H. Jeffreys, *The Theory of Probability* Oxford Classic Texts in the Physical Sciences  
1726        (, 1939).
- 1727        [130] R. E. Kass and A. E. Raftery, J. Am. Stat. Assoc. **90**, 773 (1995).
- 1728        [131] P. Machado, H. Schulz, and J. Turner, Physical Review D **102** (2020).
- 1729        [132] R. Wendell, *Three Flavor Oscillation Analysis of Atmospheric Neutrinos in Super-  
1730        Kamiokande*, PhD thesis, University of North Carolina, 2008.

- <sub>1731</sub> [133] R. G. Calland, A. C. Kaboth, and D. Payne, **9**, P04016 (2014).
- <sub>1732</sub> [134] R. Wendell, <http://www.phy.duke.edu/raw22/public/Prob3++/>.
- <sub>1733</sub> [135] F. Kallenborn, C. Hundt, S. Böser, and B. Schmidt, Computer Physics Communications **234**, 235 (2019).
- <sub>1734</sub>
- <sub>1735</sub> [136] A. M. Dziewonski and D. L. Anderson, Phys. Earth Planet. Inter. **25**, 297 (1981).
- <sub>1736</sub> [137] S. Bourret, J. A. B. Coelho, and V. V. E. and, Journal of Physics: Conference Series **888**, 012114 (2017).
- <sub>1737</sub>
- <sub>1738</sub> [138] C. Rott, A. Taketa, and D. Bose, Scientific Reports **5** (2015).
- <sub>1739</sub> [139] K. Hagiwara, N. Okamura, and K. ichi Senda, Journal of High Energy Physics **2011** (2011).
- <sub>1740</sub>
- <sub>1741</sub> [140] D. Typinski, Earth Gravity, <http://www.typnet.net/Essays/EarthGravGraphics/EarthGrav.pdf>, Accessed: 24-06-2022.
- <sub>1742</sub>
- <sub>1743</sub> [141] D. B. et al., T2K Technical Note **425** (2022).
- <sub>1744</sub> [142] V. D. Barger, K. Whisnant, S. Pakvasa, and R. J. N. Phillips, Phys. Rev. D **22**, 2718 (1980).
- <sub>1745</sub>

# <sup>1746</sup> List of Figures

<sup>1747</sup> 1.1	The cross-section of neutrinos from various natural and man-made sources as a function of neutrino energy. Taken from [22] . . . . .	9
<sup>1748</sup>		
<sup>1749</sup> 1.2	The solar neutrino flux as a function of neutrino energy for various fusion reactions and decay chains as predicted by the Standard Solar Model. Taken from [23]. . . . .	10
<sup>1750</sup>		
<sup>1751</sup> 1.3	Left panel: The atmospheric neutrino flux for different neutrino flavours as a function of neutrino energy as predicted by the 2007 Honda model (“This work”) [40], the 2004 Honda model (“HKKM04”) [41], the Bartol model [39] and the FLUKA model [42]. Right panel: The ratio of the muon to electron neutrino flux as predicted by all the quoted models. Both figures taken from [40]. . . . .	12
<sup>1752</sup>		
<sup>1753</sup>		
<sup>1754</sup>		
<sup>1755</sup>		
<sup>1756</sup>		
<sup>1757</sup>		
<sup>1758</sup> 1.4	A diagram illustrating the definition of zenith angle as used in the Super Kamiokande experiment [43]. . . . .	13
<sup>1759</sup>		
<sup>1760</sup> 1.5	Predictions of the summed neutrino and antineutrino flux for electron and muon neutrinos from the Bartol [39], Honda [40] and FLUKA [42] models as a function of zenith angle with respect to the detector. Left panel: $0.3 < E_\nu < 0.5$ . Middle panel: $0.9 < E_\nu < 1.5$ . Right panel: $3.0 < E_\nu < 5.0$ . Figures taken from [43]. . . . .	14
<sup>1761</sup>		
<sup>1762</sup>		
<sup>1763</sup>		
<sup>1764</sup>		
<sup>1765</sup> 1.6	Constraints on the atmospheric oscillation parameters, $\sin^2(\theta_{23})$ and $\Delta m_{23}^2$ , from atmospheric and long baseline experiments: SK [48], T2K [49], NO $\nu$ A [50], IceCube [51] and MINOS [52]. Figure taken from [53].	15
<sup>1766</sup>		
<sup>1767</sup>		
<sup>1768</sup> 1.7	Reactor electron antineutrino fluxes for $^{235}\text{U}$ (Black), $^{238}\text{U}$ (Green), $^{239}\text{Pu}$ (Purple), and $^{241}\text{Pu}$ (Orange) isotopes. The inverse $\beta$ -decay cross-section (Blue) and corresponding measurable neutrino spectrum (Red) are also given. Top panel: Schematic of Inverse $\beta$ -decay interaction including the eventual capture of the emitted neutron. This capture emits a $\gamma$ -ray which provides a second signal of the event. Taken from [65]. . . . .	18
<sup>1769</sup>		
<sup>1770</sup>		
<sup>1771</sup>		
<sup>1772</sup>		
<sup>1773</sup>		
<sup>1774</sup> 2.1	A schematic diagram of the Super-Kamiokande Detector. Taken from [79].	22

1775	2.2	The location of “standard PMTs” (red) inside the SK detector. Taken from [77]. . . . .	26
1776			
1777	2.3	Schematic view of the data flow through the data acquisition and online system. Taken from [92]. . . . .	29
1778			
1779	2.4	The cross-section view of the Tokai to Kamioka experiment illustrating the beam generation facility at J-PARC, the near detector situated at a baseline of 280m and the Super Kamiokande far detector situated 295km from the beam target. . . . .	32
1780			
1781			
1782			
1783	2.5	The near detector suite for the T2K experiment showing the ND280 and INGRID detectors. The distance between the detectors and the beam target is 280m. . . . .	33
1784			
1785			
1786	2.6	Top panel: Bird’s eye view of the most relevant part of primary and secondary beamline used within the T2K experiment. The primary beamline is the main-ring proton synchrotron, kicker magnet, and graphite target. The secondary beamline consists of the three focusing horns, decay volume, and beam dump. Figure taken from [106]. Bottom panel: The side-view of the secondary beamline including the focusing horns, beam dump and neutrino detectors. Figure taken from [107]. . . . .	35
1787			
1788			
1789			
1790			
1791			
1792			
1793	2.7	The Monte Carlo prediction of the energy spectrum for each flavour of neutrino ( $\nu_e$ , $\bar{\nu}_e$ , $\nu_\mu$ and $\bar{\nu}_\mu$ ) in the neutrino dominated beam FHC mode (Left) and antineutrino dominated beam RHC mode (Right) expected at SK. Taken from [108]. . . . .	36
1794			
1795			
1796			
1797	2.8	Top panel: T2K muon neutrino disappearance probability as a function of neutrino energy. Middle panel: T2K electron neutrino appearance probability as a function of neutrino energy. Bottom panel: The neutrino flux distribution for three different off-axis angles (Arbitrary units) as a function of neutrino energy. . . . .	38
1798			
1799			
1800			
1801			
1802	2.9	The components of the ND280 detector. The neutrino beam travels from left to right. Taken from [106]. . . . .	39
1803			
1804	2.10	Comparison of data to Monte Carlo prediction of integrated deposited energy as a function of track length for particles that stopped in FGD1. Taken from [111]. . . . .	41
1805			
1806			

1807	2.11 Schematic design of a Time Projection Chamber detector. Taken from [112].	42
1808	2.12 The distribution of energy loss as a function of reconstructed momentum for charged particles passing through the TPC, comparing data to Monte Carlo prediction. Taken from [112].	42
1810		
1811	2.13 A schematic of the P0D side-view. Taken from [113].	44
1812	2.14 Left panel: The Interactive Neutrino GRID on-axis Detector. 14 modules are arranged in a cross-shape configuration, with the center modules being directly aligned with the on-axis beam. Right panel: The layout of a single module of the INGRID detector. Both figures are recreated from [106].	46
1814		
1816		
1817	3.1 Example of using Monte Carlo techniques to find the area under the blue line. The gradient and intercept of the line are 0.4 and 1.0 respectively. The area found to be under the curve using one thousand samples is 29.9 units.	51
1819		
1820		
1821	3.2 The area under a line of gradient 0.4 and intercept 1.0 for the range $0 \leq x \leq 10$ as calculated using Monte Carlo techniques as a function of the number of samples used in each repetition. The analytical solution to the area is 30 units as given by the red line.	52
1823		
1824		
1825	3.3 Three MCMC chains, each with a stationary distribution equal to a Gaussian centered at 0 and width 1 (As indicated by the black dotted lines). All of the chains use a Gaussian proposal function but have different widths (or 'step size $\sigma$ '). The top panel has $\sigma = 0.1$ , middle panel has $\sigma = 0.5$ and the bottom panel has $\sigma = 5.0$ .	57
1827		
1829		
1830	3.4 The log-likelihood from the fit detailed in <a href="#">DB: Link to AsimovA Sensitivity Section</a> as a function of the number of steps accumulated in each fit. Many independent MCMC chains were run in parallel and overlaid on this plot. The red line indicates the $1 \times 10^5$ step burn-in period after which the log-likelihood becomes stable.	58
1832		
1833		
1834		

1835      3.5	Left: The two dimensional probability distribution for two correlated parameters $x$ and $y$ . The red distribution shows the two dimensional probability distribution when $0 \leq x \leq 5$ . Right: The marginalised probability distribution for the $y$ parameter found when requiring the $x$ to be bound between $-5 \leq x \leq 5$ and $0 \leq x \leq 5$ for the black and red distribution, respectively. . . . .	61
1841      4.1	An “Oscillogram” that depicts the $P(\nu_\mu \rightarrow \nu_e)$ oscillation probability as a function of neutrino energy and cosine of the zenith angle. The zenith angle is defined such that $\cos(\theta_Z) = 1.0$ represents neutrinos that travel from directly above the detector. The four-layer constant density PREM model approximation is used and Asimov A oscillation parameters are assumed. . . . .	67
1847      4.2	The effect of $\delta_{CP}$ for atmospheric neutrinos given in terms of the neutrino energy and zenith angle. The oscillogram compares the $P(\nu_\mu \rightarrow \nu_e)$ oscillation probability for a CP conserving ( $\delta_{CP} = 0.0$ ) and CP violating ( $\delta_{CP} = -1.601$ ) value of $\delta_{CP}$ . The other oscillation parameters assume the “Asimov A” oscillation parameter set given in Table 4.1. . . . .	69
1852      4.3	An illustration of the matter-induced effects on the oscillation probability, given as a function of neutrino energy and zenith angle. The top row of panels gives the $P(\nu_e \rightarrow \nu_e)$ oscillation probability and the bottom row illustrates the $P(\bar{\nu}_e \rightarrow \bar{\nu}_e)$ oscillation probability. The left column highlights the oscillation probability in a vacuum, whereas the middle and right column represents the oscillation probabilities when the four layer fixed density PREM model is assumed. All oscillation probabilities assume the “Asimov A” set given in Table 4.1, but importantly, the right column sets an inverted mass hierarchy. The “matter resonance” effects at $E_\nu \sim 5\text{GeV}$ can be seen in the $P(\nu_e \rightarrow \nu_e)$ for normal mass hierarchy and $P(\bar{\nu}_e \rightarrow \bar{\nu}_e)$ for inverted hierarchy. . . . .	70
1863      4.4	The oscillation probability for beam neutrino events, given as a function of neutrino energy. All oscillation parameters assume the “Asimov A” set given in Table 4.1 unless otherwise stated. Each panel represents a change in one of the oscillation parameters whilst keeping the remaining parameters fixed. . . . .	71

1868	4.5	The oscillation probability $P(\nu_\mu \rightarrow \nu_e)$ , given as a function of neutrino energy and zenith angle, which highlights an example of the “fast” oscillations in the sub-GeV upgoing region. . . . .	73
1871	4.6	Illustration of the averaging procedure for $N = 2$ . The oscillation probabilities calculated on the finer left binning are averaged to obtain the oscillation probabilities in the coarser right binning. These averaged oscillation probabilities with the coarser binning are then applied to each event during the fit. . . . .	76
1876	4.7	Event rate of the SubGeV_elike_0dcy sample as a function of the number of sub-divisions per coarse bin. Each sub-plot represents the event rate of the sample at a different oscillation parameter set (thrown from the PDG priors). The red-line in each sub plot represents the mean of the event rate over the different values of sub divisions for that particular oscillation parameter throw. . . . .	78
1882	4.8	Variance of event rate for each atmospheric sample as a function of the number of sub-divisions per coarse bin. The solid red line indicates the 0.1% threshold and the dashed red line is a graphical indication of the variance at a sub-division $N = 10$ . . . . .	79
1886	4.9	Variance of sample likelihood, when compared to ‘Asimov data’ set at Asimov A, for each atmospheric sample as a function of the number of sub-divisions per coarse bin. The solid red line indicates the 0.1% threshold and the dashed red line is a graphical indication of the variance at a sub-division $N = 10$ . . . . .	80
1891	4.10	The oscillation probability, $P(\nu_\mu \rightarrow \nu_e)$ (top row) and $P(\nu_e \rightarrow \nu_e)$ (bottom row), given as a function of neutrino energy and zenith angle. The left column gives the “fine” binning used to calculate the oscillation probabilities and the right column illustrates the “coarse” binning used to reweight the MC events. The fine binning choice is given with $N = 10$ , which was determined to be below threshold from Figure 4.8 and Figure 4.9. . . . .	81

1898	4.11 The calculation time taken to both calculate the oscillation probabilities 1899 and fill the “coarse” oscillograms, following the technique given in 1900 section 4.2, for the CUDAProb3 and ProbGPU (Red) calculation engines. 1901 CUDAProb3 has both a GPU (Blue) and CPU (Black) implementation, 1902 where the CPU implementation is multithreaded. Therefore, 8-threads 1903 (solid) and 40-threads (dashed) configurations have been used. Prob3, 1904 which is a CPU single-thread implementation has a mean step time of 1905 1.142s. . . . .	83
1906	4.12 The density of the Earth given as a function of the radius, as given by the 1907 PREM model (Black) and the constant density four-layer approximation 1908 (Blue), as used in the official SK-only analysis. . . . .	84
1909	4.13 The oscillation probability, $P(\nu_\mu \rightarrow \nu_e)$ (top row) and $P(\nu_e \rightarrow \nu_e)$ (bot- 1910 tom row), given as a function of neutrino energy and zenith angle. 1911 The left column gives probabilities where the constant $Z/A = 0.5$ 1912 approximation which is used in the official SK-only analysis. The mid- 1913 dle column gives the probabilities where the more accurate $Z/A =$ 1914 $[0.468, 0.498]$ values as given in Table 4.2. The right column illustrates 1915 the difference in oscillation probability between the two different tech- 1916 niques. . . . .	86
1917	4.14 The density of the Earth given as a function of the radius, as given by 1918 the PREM model (Black), the constant density four-layer approxima- 1919 tion (Blue), as used in the official SK-only analysis, and the quadratic 1920 approximation of the PREM model (Red). . . . .	87
1921	4.15 The oscillation probability, $P(\nu_\mu \rightarrow \nu_e)$ (top row) and $P(\nu_e \rightarrow \nu_e)$ (bot- 1922 tom row), given as a function of neutrino energy and zenith angle. The 1923 left column gives probabilities where the four-layer constant density ap- 1924 proximation is used. The middle column gives the probabilities where 1925 the density is integrated over the trajectory, using the quadratic PREM 1926 approximation, for each $\cos(\theta_Z)$ is used. The right column illustrates the 1927 difference in oscillation probability between the two different techniques.	88

- 1928      4.16 The oscillation probability,  $P(\nu_\mu \rightarrow \nu_e)$  (top row) and  $P(\nu_e \rightarrow \nu_e)$  (bot-  
1929      tom row), given as a function of neutrino energy and zenith angle. The  
1930      left column gives probabilities where a fixed production height of 25km  
1931      is used. The middle column gives the probabilities where the produc-  
1932      tion height is analytically averaged. The right column illustrates the  
1933      difference in oscillation probability between the two different techniques. 92

# **List of Tables**

1935	2.1	The various SK periods and respective live-time. The SK-VI live-time is calculated until 1 <sup>st</sup> April 2022. SK-VII started during the writing of this thesis. . . . .	21
1936			
1937			
1938	2.2	The trigger thresholds and extended time windows saved around an event which were utilised throughout the SK-IV period. The exact thresholds can change and the values listed here represent the thresholds at the start and end of the SK-IV period. . . . .	30
1939			
1940			
1941			
1942	2.3	The threshold momentum and energy for a particle to generate Cherenkov light in ultrapure water, as calculated in Equation 2.2 in ultrapure water which has refractive index $n = 1.33$ . . . . .	31
1943			
1944			
1945	3.1	Jeffreys scale for strength of preference for two models $A$ and $B$ as a function of the calculated Bayes factor ( $B_{AB} = B(A/B)$ ) between the two models [129]. The original scale is given in terms of $\log_{10}(B(A/B))$ but converted to linear scale for easy comparison throughout this thesis.	63
1946			
1947			
1948			
1949	4.1	Reference values of the neutrino oscillation parameters for two different oscillation parameter sets. . . . .	72
1950			
1951	4.2	Description of the four layers of the Earth invoked within the average constant density approximation of the PREM model [136]. . . . .	84
1952			
1953	4.3	The quadratic polynomial fits to the PREM model for four assumed layers of the PREM model. The fit to calculate the coefficients is given in [141], where $x = R/R_{Earth}$ . . . . .	87
1954			
1955			